

SC5459.FR

Copy No. 4

SC5459.FR

AD-A224 285

AFOSR-TR- 90 0745

**PROCESSABILITY AND HIGH TEMPERATURE
BEHAVIOR OF EMERGING AEROSPACE ALLOYS**

FINAL REPORT

May 1, 1986 through February 28, 1990

CONTRACT NO. F49620-86-C-0058

Prepared for

**Air Force Office of Scientific Research
Directorate of Electronic and Material Sciences
Building 410
Bolling AFB, DC 20332-6448**

**Part I: C. Gandhi
A.K. Ghosh
Part II: C.G. Rhodes
Principal Investigators**

**DTIC
ELECTE
JUL 20 1990
S E D**

JUNE 1990

Approved for public release; distribution unlimited



**Rockwell International
Science Center**

The Contractor, Rockwell International Corporation Science Center, hereby certifies that, to the best of its knowledge and belief, the technical data delivered herewith under Contract No. F49620-86-C-0058 is complete, accurate, and complies with all requirements of the contract.

June 25, 1990

Date



Name and Title of Certifying Official

C.G. Rhodes, Program Manager

REPORT DOCUMENTATION PAGE

FORM APPROVED
OMB No. 0704-0188

1a. REPORT SECURITY CLASSIFICATION UNCLASSIFIED		1b. RESTRICTIVE MARKINGS	
2a. SECURITY CLASSIFICATION AUTHORITY		3. DISTRIBUTION/AVAILABILITY OF REPORT Approved for public release	
2b. CLASSIFICATION/DOWNGRADING SCHEDULE			
4. PERFORMING ORGANIZATION REPORT NUMBER(S) SC5459.FR		5. MONITORING ORGANIZATION REPORT NUMBER(S) AFOSR-TR- 91 0745	
6a. NAME OF PERFORMING ORGANIZATION ROCKWELL INTERNATIONAL Science Center	6b. OFFICE SYMBOL (If Applicable)	7a. NAME OF MONITORING ORGANIZATION <i>Same as 8a</i>	
6c. ADDRESS (City, State and ZIP Code) 1049 Camino Dos Rios Thousand Oaks , CA 91360		7b. ADDRESS (City, State and ZIP Code) <i>Same as 8c</i>	
8a. NAME OF FUNDING/SPONSORING ORGANIZATION Air Force Office of Scientific Research	8b. OFFICE SYMBOL (If Applicable) <i>NE</i>	8c. PROCUREMENT INSTRUMENT IDENTIFICATION NUMBER CONTRACT NO. F49620-86-C-0058	
8c. ADDRESS (City, State and ZIP Code) Building 410 Bolling AFB, DC 20332		10. SOURCE OF FUNDING NOS.	
		PROGRAM ELEMENT NO. <i>61102F</i>	PROJECT NO. <i>2306/A*</i>
		TASK NO. <i>A1</i>	WORK UNIT ACCESSION NO.
11. TITLE (Include Security Classification) PROCESSABILITY AND HIGH TEMPERATURE BEHAVIOR OF EMERGING AEROSPACE ALLOYS (U)			
12. PERSONAL AUTHOR(S) Gandhi, C., Ghosh, A.K., and Rhodes, C.G.			
13a. TYPE OF REPORT FINAL	13b. TIME COVERED FROM 05/01/86 TO 02/28/90	14. DATE OF REPORT (Year, Month, Day) 1990, JUNE	15. PAGE COUNT
16. SUPPLEMENTARY NOTATION			
17. COSATI CODES		18. SUBJECT TERMS (Continue on reverse if necessary and identify by block number)	
FIELD	GROUP	SUB-GROUP	
19. ABSTRACT (Continue on reverse if necessary and identify by block number) In Part I, Task 1, a model for subgrain superplasticity has been developed. Aluminum alloys that contain low angle boundaries exhibit different superplastic behavior than alloys consisting of high angle boundaries. On a relative basis, the low angle boundaries increase the flow stress but impart a greater resistance to cavitation; the strain-rate sensitivity of this material is generally smaller and the change in the strain-rate sensitivity with strainrate shows a minimum instead of a maximum as observed in the large angle boundary materials. As a result, the subgrain material can be deformed to a large tensile strains at fast strain rates. A kinetic model for subgrain superplasticity that invokes a balance between the <i>(Continued on Back)</i>			
20. DISTRIBUTION/AVAILABILITY OF ABSTRACT <i>unlimited</i>		21. ABSTRACT SECURITY CLASSIFICATION <i>Unclassified</i>	
22a. NAME OF RESPONSIBLE INDIVIDUAL <i>Klosterin</i>		22b. TELEPHONE NUMBER (INCLUDE AREA CODE) <i>202 7674933</i>	22c. OFFICE SYMBOL <i>NE</i>

(Continued from front)

arrival and emission rates of dislocations at low angle boundaries is presented. It explains several features of subgrain superplasticity. It also explains why ultrafine dispersoids of intermetallics appear to stabilize the subgrain structure in aluminum. Early work on the correlation between flow stress and subgrain size in dynamic recrystallization of metals may also be consistent with the model. JES

Part I, Task 2 was designed to develop an understanding of the interrelationship among the various deformation processing approaches, the resulting microstructures and their subsequent elevated temperature flow characteristics. Two dispersion containing Al alloys, in their as extruded state, were subjected to a variety of processing procedures, such as warm isothermal rolling, isothermal compression, three-axis forging and thermomechanical treatment (TMT) involving overaging and static recrystallation steps. The flow behavior of these materials, including flow stress, stress hardening, and strain rate sensitivities and progressively changing microstructure, were then studied as functions of temperature strain rate. It found that both deformation mode and the absolute level of effective strain influence subsequent flow characteristics of these materials. Three-axis forging and TMT processes showed unique advantages in improving processability, even though the extruded or rolled microstructures were just as fine or finer. While isothermal compression to extremely large strains appeared to possess similar potential as three-axis forging process, the latter is more practical to use.

Part II of this program has examined the effects of C, Fe, and O, on creep behavior of Ti-24Al-11Nb.

Surface cracking of the type observed in samples creep tested to failure was not present in samples tested only into the steady-state regime. Surface cracking is a function of strain and time at temperature. It is not a 'creep mechanism' as has been suggested elsewhere, but rather occurs when the material has strained well into steady-state or, more likely, into tertiary creep.

The most significant of the alloying effects on steady-state creep was due to silicon at the higher test temperatures, where increasing Si reduced the creep rate. Similarly, increasing carbon also lowered creep rate, although not to the degree observed for Si. Iron was effective only at the lowest temperatures, where reducing Fe decreased creep rates. At the higher temperatures, Fe had essentially no effect on creep.

All the data indicate a single creep mechanism in the temperature range of 675-750°C. Dislocation climb appears to be the most likely rate controlling mechanism. Below 675°C, the data suggest a change in the (unidentified) rate controlling mechanism.



TABLE OF CONTENTS

	<u>Page</u>
3.3.4.1 Material Selection	63
3.3.4.2 Heat Treatments	64
3.3.4.3 Tensile Properties	64
3.3.4.4 Creep Properties	66
3.3.5 Discussion of Results	80
3.3.6 Summary and Conclusions	82
4.0 REFERENCES	83
5.0 APPENDIX	86

LIST OF FIGURES

<u>Figure</u>	<u>Page</u>
1 Schematics of the contrast between the flow properties of (a) materials with large angle and (b) materials with low angle boundaries. The principal difference is in the curvature of the $m(\dot{\epsilon})$ curves. In the sub-grain materials the best elongations are obtained at high strain rates where m is greater.	11
2 Transmission electron micrographs of intermetallic dispersoids of (a) Cr-rich compounds in 7475, and (b) $ZrAl_3$ in D19. The $ZrAl_3$ dispersoids are about ten times smaller than the Cr rich dispersoids.	12
3 Normalization of $\sigma(\dot{\epsilon})$ data for 7475 for different grain sizes using Eq. (3). The experimental curves appear to merge into a master curve when the strain rate is normalized with respect to the grain size.	14
4 $\sigma(\dot{\epsilon})$ data for several aluminum alloys where the $\dot{\epsilon}$ has been normalized for differences in grain size and temperature.	14
5 Experimental data for a material with large angle boundaries (7475) and low angle boundaries (D19) showing the difference in the curvature of the $m(\dot{\epsilon})$ curves.	15
6 Distribution of grain boundary misorientations in the subgrain (D19) and other materials.	16



LIST OF FIGURES

<u>Figure</u>		<u>Page</u>
7	Evidence of lower cavitation in D19 as compared to 7475 or 8091.	16
8	Description of the model proposed to explain subgrain superplasticity. The steady state deformation obtains when the emission rate of dislocations from the boundaries is equal to the arrival rate of dislocations. The intermetallic dispersoids influence the mobility and therefore the arrival rate of dislocations.	17
9	The change in the critical distance for dislocation emission from a boundary of misorientation $\Delta\theta$, at different levels of applied stress. Note this distance varies from about 10 to 25 atom spacings.	19
10	The variation of subgrain size with stress at (a) 340°C, (b) 520°C, and (c) 650°C	21
11	The predicted shape of $\sigma(\dot{\epsilon})$ curves for different misorientations at (a) 340°C and (b) 520°C.	23
12	TEM micrograph of 7064 AlSiC rolled 92% at 250°C.	36
13	TEM micrograph of 7064 AlSiC rolled 88% at 350°C.	36
14	{112} CBED pattern from grain indicated by arrow in Fig. 13	36
15	SEM microstructures of 7064 AlSiC: (a) as extruded; (b) 350°C warm rolled; (c) fine grain TMT; and (d) three-axis forged conditions. (Rolling direction is vertical.)	38
16	Grain size (subgrain size) of 7064 Al/SiC for various processing methods.	39
17	Subgrain size distribution of 7064 Al/SiC: (a) 250°C rolled; (b) 350°C rolled; and (c) fine grain TMT.	39
18	Grain size of 7064 Al/SiC after tensile test at elevated temperatures.	40
19	SEM microstructures of 350°C rolled 7064 Al/SiC after tested at 350°C and 0.0001 1/s: (a) gauge area, and (b) grip area. (Tensile axis is vertical.)	42
20	Typical grain structures of 7064 Al/SiC after compression test at 350°C and 0.0001 1/s: (a) plane parallel to compression (vertical) axis, and (b) plane normal to compression axis.	42



LIST OF FIGURES

<u>Figure</u>		<u>Page</u>
21	Variation of average grain size of 7064 Al/SiC tested in compression at various temperatures and strain rates of (a) 0.0001 1/s and (b) 0.01 1/s as a function of strain.....	43
22	7064 Al matrix subgrain misorientation distribution: (a) 250°C rolled; (b) 350°C rolled; (c) fine grain TMT; (d) as-extruded and (e) three-axis forged condition.....	44
23	Relative frequency of average grain misorientation of 7064 AlSiC.	45
24	Optical microstructure of 350°C rolled 7064 Al/SiC, (a) as-extruded, (b) rolled 25% at 350°C, (c) rolled 52% at 350°C, and (d) rolled 88% at 350°C	45
25	Optical microstructure of 250°C rolled 7064 Al/SiC, (a) as-extruded (b) rolled 25% at 250°C, (c) rolled 53% at 250°C, and (d) rolled 92% at 250°C	46
26	Area fraction of SiC clusters as a function of effective strain.	47
27	Area fraction occupied by SiC in nonclustered areas as a function of effective strain.	47
28	Aspect ratio of SiC particulate clusters as a function of effective strain.	47
29	Fracture strain vs grain size of 7064 Al/SiC (a) near the fracture surface (top), and (b) in the grip area (bottom).	53
30	Cavitation below the fracture surface of the 350°C rolled 7064 Al/SiC tested at 350°C and 0.01 1/s.	54
31	Cavitation initiated at the tip of SiC cluster.	54
32	Cavity formation along grain boundaries.	54
33	Cavitation as a function of strain, determined by metallographic method.	54
34	Optical microstructure of (a) 380°C rolled and (b) three-axis forged Al-8-Fe-4Ce	55
35	SEM microstructure of 380°C rolled sheet tested at 480°C and 0.005 1/s.	55



LIST OF FIGURES

<u>Figure</u>		<u>Page</u>
36	Variation of microstructural size of Al-8Fe-4Ce as a function of strain.....	56
37	Optical microstructure of rolled Al-8Fe-4Ce tested at (a) 0.005 1/s and (b) 0.1 1/s. Notice the nonuniform microstructure as a result of high strain in (b).	56
38	(a) Flow stress vs strain rate of as-extruded Al-8Fe-4Ce. Open data points: compression data; solid data points: tensile data. (b) Strain rate sensivity vs strain rate of as-extruded Al-8Fe-4Ce.	57
39	Arrhenius plots showing the variation of strain rate with the reciprocal temperature of the as-extruded Al-8Fe-4Ce.	58
40	Typical microstructure of Ti-24Al-11Nb alloys creep tested in this program.	64
41	Illustrating method for determining primary creep strain from experimental creep curve.	67
42	Primary creep strain for Ti-24Al-11Nb alloys as a function of applied stress for three temperatures.	68
43	Initial creep rate for Ti-24Al-11Nb alloys as a function of steady-state creep rate.	68
44	Transient creep strain as a function of applied stress.	69
45	Steady-state creep rate at 600°C as a function of carbon content for three stress levels.	69
46	Steady-state creep rate at 675°C as a function of carbon content for three stress levels.	70
47	Steady-state creep rate at 750°C as a function of carbon content for two stress levels.	70
48	Steady-state creep rate at 600°C as a function of iron content for three stress levels.	71
49	Steady-state creep rate at 675°C as a function of iron content for three stress levels.	71



LIST OF FIGURES

<u>Figure</u>		<u>Page</u>
50	Steady-state creep rate at 750°C as a function of iron content for two stress levels.	71
51	Steady-state creep rate at 600°C as a function of silicon content for three stress levels.	71
52	Steady-state creep rate at 675°C as a function of silicon content for three stress levels.	72
53	Steady-state creep rate at 750°C as a function of silicon content for two stress levels.	72
54	Steady-state creep rate as a function of reciprocal temperature for baseline alloy at three stress levels.	72
55	Steady-state creep rate as a function of reciprocal temperature for low carbon containing alloy at three stress levels.	72
56	Steady-state creep rate as a function of reciprocal temperature for intermediate carbon containing alloy at three stress levels.	73
57	Steady-state creep rate as a function of reciprocal temperature for low iron containing alloy at three stress levels.	73
58	Steady-state creep rate as a function of reciprocal temperature for intermediate iron containing alloy at three stress levels.	73
59	Steady-state creep rate as a function of reciprocal temperature for intermediate silicon containing alloy at three stress levels.	73
60	Steady-state creep rate as a function of reciprocal temperature for high silicon containing alloy at three stress levels.	74
61	Apparent activation energy vs applied stress for baseline (Alloy 1), low iron (Alloy 4), intermediate iron (Alloy 5), and high silicon (Alloy 7) alloys.	76
62	$\ln \dot{\epsilon}$ vs $\ln \sigma$ for 600°C test of variable carbon alloys.	77
63	$\ln \dot{\epsilon}$ vs $\ln \sigma$ for 675°C test of variable carbon alloys.	77
64	$\ln \dot{\epsilon}$ vs $\ln \sigma$ for 750°C test of variable carbon alloys.	77
65	$\ln \dot{\epsilon}$ vs $\ln \sigma$ for 600°C test of variable iron alloys.	78



LIST OF FIGURES

<u>Figure</u>		<u>Page</u>
66	$\ln \dot{\epsilon}$ vs $\ln \sigma$ for 675°C test of variable iron alloys.	78
67	$\ln \dot{\epsilon}$ vs $\ln \sigma$ for 750°C test of variable iron alloys.	78
68	$\ln \dot{\epsilon}$ vs $\ln \sigma$ for 600°C test of variable silicon alloys.	79
69	$\ln \dot{\epsilon}$ vs $\ln \sigma$ for 675°C test of variable silicon alloys.	79
70	$\ln \dot{\epsilon}$ vs $\ln \sigma$ for 750°C test of variable silicon alloys.	79



LIST OF TABLES

<u>Table</u>		<u>Page</u>
1	Composition of Aluminum Alloys	12
2	Compositions of Ti Aluminide Alloys (at. pct.).....	32
3	Room Temperature Tensile Properties of Titanium Aluminide Alloys	33
4	600°C Tensile Properties of Titanium Aluminide Alloys	40
5	675°C Tensile Properties of Titanium Aluminide Alloys	41
6	750°C Tensile Properties of Titanium Aluminide Alloys	48
7	Summary of Tensile Test Results of TMT 7064 Al/SiC	50
8	Summary of Tensile Results of Three-Axis Forged 7064 Al-SiC	50
9	Strain Rate Sensitivity of As-Extruded 7064 Al/SiC	51
10	Summary of Tensile Test Results of Al-8Fe-4Ce	58
11	Compositions of Ti Aluminide Alloys, at% (wt%).....	63
12	Room Temperature Tensile Properties of Titanium Aluminide Alloys	65
13	600°C Tensile Properties of Titanium Aluminide Alloys	65
14	675°C Tensile Properties of Titanium Aluminide Alloys	66
15	750°C Tensile Properties of Titanium Aluminide Alloys	66
16	Apparent Activation Energy for Steady State Creep in Titanium Aluminide Alloys at 103 MPa (15 ksi)	74
17	Apparent Activation Energy for Steady State Creep in Titanium Aluminide Alloys at 172 MPa (25 ksi)	75
18	Apparent Activation Energy for Steady State Creep in Titanium Aluminide Alloys at 276 MPa (40 ksi)	75
19	Stress Exponent for Power Law Creep in Titanium Alumindes	79



LIST OF TABLES

<u>Table</u>		<u>Page</u>
A1	Steady State Creep Rates for Titanium Aluminides Tested at 600°C and 117 MPa (17 ksi)	86
A2	Steady State Creep Rates for Titanium Aluminides Tested at 600°C and 172 MPa (17 ksi)	86
A3	Steady State Creep Rates for Titanium Aluminides Tested at 600°C and 276 MPa (17 ksi)	87
A4	Steady State Creep Rates for Titanium Aluminides Tested at 675°C and 103 MPa (17 ksi)	87
A5	Steady State Creep Rates for Titanium Aluminides Tested at 675°C and 172 MPa (17 ksi)	88
A6	Steady State Creep Rates for Titanium Aluminides Tested at 675°C and 241 MPa (17ksi)	88
A7	Steady State Creep Rates for Titanium Aluminides Tested at 750°C and 90 MPa (17 ksi)	89
A8	Steady State Creep Rates for Titanium Aluminides Tested at 750°C and 138 MPa (17 ksi)	89
A9	Steady State Creep Rates for Titanium Aluminides Tested at 750°C and 207 MPa (17 ksi)	90



FOREWORD

This document is the final report on Contract No. F49620-86-C-0058 sponsored by the Air Force Office of Scientific Research entitled "Processability and High Temperature Behavior of Emerging Aerospace Alloys." The results of research conducted subsequent to issuance of the Second Annual Report, corresponding to the period from May 1988 through Feb. 1990, are reported herein.

Readers are referred to the First Annual Report and the Second Annual Report - References 1 and 2 in this document - for details of results generated prior to May 1988.

The program was monitored by Dr. Allen Rosenstein of AFOSR and was conducted at the Rockwell International Science Center by Dr. Amit Ghosh, Dr. Chimata Gandhi and Mr. Cecil Rhodes. Dr. Ghosh was Program Manager from May 1986 through August 1988, at which time Mr. Rhodes became Program Manager. Dr. Gandhi and Mr. Rhodes were Principal Investigators for Parts I and II of the Program, respectively.

In this document, Part I, Task I has been written by Dr. Gandhi who was assisted by Prof. Richi Raj of Cornell University and Part I, Task II has been written by Dr. Ghosh with the assistance of Mr. Y. Zhu of the University of Michigan. Part II results have been written by Mr. Rhodes.



1.0 ABSTRACT

This final report describes results of a three-year research program to study the relationship among processing, microstructure, and properties of advanced aerospace alloys. This is a two-part program. Part I is a study of microstructural control and processibility of Al alloys. Part II is a study of creep in alpha-2 type titanium aluminides. This report highlights results developed during the final year of the program. Earlier results have been reported in the first and second annual reports.

Part I of this program has examined a unified approach for understanding and assessing microstructural changes in Al alloys under the influence of different modes of thermomechanical and deformation processing.

In Part I, Task 1, a model for subgrain superplasticity has been developed. Aluminum alloys that contain low angle boundaries exhibit different superplastic behavior than alloys consisting of high angle boundaries. On a relative basis, the low angle boundaries increase the flow stress but impart a greater resistance to cavitation; the strain-rate sensitivity of this material is generally smaller and the change in the strain-rate sensitivity with strain rate shows a minimum instead of a maximum as observed in the large angle boundary materials. As a result, the subgrain material can be deformed to large tensile strains at fast strain rates. A kinetic model for subgrain superplasticity that invokes a balance between the arrival and emission rates of dislocations at low angle boundaries is presented. It explains several features of subgrain superplasticity. It also explains why ultrafine dispersoids of intermetallics appear to stabilize the subgrain structure in aluminum. Early work on the correlation between flow stress and the subgrain size in dynamic recrystallization of metals may also be consistent with the model.

Part I, Task 2 was designed to develop an understanding of the interrelationship among the various deformation processing approaches, the resulting microstructures and their subsequent elevated temperature flow characteristics. Two dispersion containing Al alloys, in their as-extruded state, were subjected to a variety of processing procedures, such as warm isothermal rolling, isothermal compression, three-axis forging and thermomechanical treatment (TMT) involving overaging and static recrystallization steps. The flow behavior of these materials, including flow stress, strain hardening, and strain rate sensitivities and progressively changing microstructure, were then studied as functions of tem-



perature and strain rate. It was found that both deformation mode and the absolute level of effective strain influence subsequent flow characteristics of these materials. Three-axis forging and TMT processes showed unique advantages in improving processability, even though the extruded or rolled microstructures were just as fine or finer. While isothermal compression to extremely large strains appeared to possess similar potential as the three-axis forging process, the latter is more practical to use.

Part II of this program has examined the effects of C, Fe, and O, on creep behavior of Ti-24Al-11Nb. All creep tests, which were conducted at 600, 675 and 750°C in air, exhibited well defined primary and secondary regimes.

Surface cracking of the type observed in samples creep tested to failure was not present in samples tested only into the steady-state regime. Surface cracking is a function of strain and time at temperature. It is not a 'creep mechanism' as has been suggested elsewhere, but rather occurs when the material has strained well into steady-state or, more likely, into tertiary creep.

There is a positive correspondence of the initial creep rate in the primary regime with steady-state creep rate indicating that primary creep is influenced by those factors that influence steady-state creep. Significant levels of strain can accumulate during transient creep.

The most significant of the alloying effects on steady-state creep was due to silicon at the higher test temperatures, where increasing Si reduced the creep rate. Similarly, increasing carbon also lowered creep rate, although not to the degree observed for Si. Iron was effective only at the lowest temperatures, where reducing Fe decreased creep rates. At the higher temperatures, Fe had essentially no effect on creep.

All the data indicate a single creep mechanism in the temperature range of 675-750°C. Dislocation climb appears to be the most likely rate controlling mechanism. Below 675°C, the data suggest a change in the (unidentified) rate controlling mechanism.



2.0 INTRODUCTION

Processing, properties and microstructure form a close interrelationship determining the structural performance of metallic materials. Microstructure and alloy composition not only determine properties that are important for structural performance, but properties that control the processability of structural alloys. In turn, the processing methods used to fabricate components, e.g., forging or forming operations, and the microstructure resulting from them dictate structural performance. This two-part research program was designed to investigate two aspects of airframe material processing. In Part I, microstructural control and processability in Al alloys has been investigated, and the effect of microstructural conditions on widening the processing windows within which material could be successfully processed has been determined. In Part II, the creep behavior of high-temperature titanium aluminide alloys has been examined, and the importance of alloy additives on the mechanisms of creep determined.

Modern metallic materials for aerospace applications are becoming increasingly complex in character. With rapidly solidified high-strength and high-temperature materials on one hand and the emergence of low-density Al-Li alloy on the other, the development of new Al alloys is preceding the development of cost-effective processing technologies such as superplastic forming, isothermal forging and other hot-working operations. The significant impact of processing on microstructure and properties cannot be overestimated, particularly in the development of these new Al alloys where microstructural instability could lead to degradation in properties. It is being realized that empirical approaches to shaping of these alloys must be replaced by an overall approach to improving processability, which is based on the understanding of the micromechanics and is extrapolatable from one type of shape change to another. This subject is examined in Part I with the objective of developing a science base for providing a unified approach which is applicable to different processing modes. This involves appropriate microstructural control using processes of dynamic recovery and static recrystallizations, and strain-induced grain boundary migration.

Specific experimental approaches have focused on two advanced Al base materials: particulate SiC-reinforced Al sheets and high-temperature Al alloy, Al-8Fe-4Ce. Microstructural changes during deformation processing along a variety of strain paths were determined. Such changes involve quantitative characterization of grain (or subgrain) size



and misorientations as a function of processing history. In addition, the distribution of particulate reinforcements was monitored as a function of strain.

A method of three-axis forging has been devised, in which a block of metal is compressed under plane strain conditions to a high level of strain, and then rotated between successive passes to impart a very large level of strain without an overall change in the shape or size of the block. By adjusting the deformation temperature to allow dynamic recovery (not recrystallization), an extremely fine-grain microstructure could be produced. The effect of this deformation mode, which involves shear along three orthogonal directions on the microstructural features, is reported.

Part II of the program addresses creep behavior in high-temperature intermetallics designed for aerospace applications. The performance requirements of skins and subsurface structural components which will be exposed to exceptionally high temperatures in hypersonic and transatmospheric vehicles are of considerable current concern. The development of high thrust-to-weight ratio turbine engines for these advanced aircraft has also provided impetus for significant activity aimed at developing lightweight, elevated temperature materials. An alloy system emerging as a prime candidate for turbine engine applications is one based on the intermetallic compound Ti_3Al .

First-tier properties, such as tensile strength and ductility, have been well documented on alloys designated as potential structural materials. As particular alloy compositions evolve for high-temperature applications, second-tier properties, such as creep resistance, need to be evaluated.

This program was designed to examine elevated temperature creep behavior of Ti_3Al base alloys. There is an established literature base on the effects of minor alloying additions on the creep behavior of conventional Ti alloys. That base was used to compose alloy chemistries for study in this program. The effects of minor additions on both steady-state creep rate and primary creep strain are reported.

Experimental results generated earlier in the program are not re-reported in this Final Report. Details can be found in the First Annual Report¹ and Second Annual Report.²



3.0 RESULTS

3.1 Summary of Results

3.1.1 Part I, Task 1: Model for Subgrain Superplastic Flow in Al Alloys

Phenomenological experiments on a variety of aluminum alloys have shown that a special type of superplastic flow occurs when the boundaries are predominantly low angle. The strain rate sensitivity, m , of the subgrain material is generally lower than that of conventional superplastic aluminum alloys, but is still high enough to produce large strains without strain localization. More interesting is the change in m with strain-rate: in the subgrain material it goes through a minimum at intermediate strain rates while the conventional materials show a maximum. As a result, high values of m , which yield the best elongations, obtain at high strain rates in the subgrain material.

The model developed to explain this behavior invokes a kinetic equilibrium between the arrival rate and the emission rate of dislocations at low angle boundaries. The emission rate depends on the angle of the subboundary and the elastic constants while the arrival rate depends on the mobility of the dislocation which is controlled by the size and spacing of coherent intermetallic dispersoids in the lattice. The subgrain structure is stable only within a certain range of strain rate. If the strain rate is too slow then the arrival rate of dislocations exceeds the emission rate and the subboundaries gradually grow into large angle boundaries. If the strain rate is too high, then the emission rate is faster and the low angle boundaries melt into the crystal grains. Within the stable range, the m value changes and the model predicts a broad minimum in m , which agrees with experiment. The magnitude of m in the minimum is estimated to be 0.4 to 0.5 which is consistent with experiment.

3.1.2 Part I, Task 2: Effect of Processing on High Temperature Flow in Al Alloys

Three-axis forged and fine grain TMT processes produced the greatest microstructural refinement and larger grain misorientation distributions, in comparison to isothermally rolled materials. Extruded alloy showed an extremely fine microstructure but grain misorientations were generally low. These processing steps caused negligible coarsening of the Al-8Fe-4Ce alloy.



Processability improvements were greatest for the three-axis deformation showing largest ductilities and lowest flow stresses, believed to arise from extensive shear occurring on intersecting shear planes. Processability improvement was tied not only to structural fineness, but to the higher misorientation levels. Thus deformation path and the magnitude of overall strain influenced subsequent flow characteristics more strongly than grain size or subgrain size would indicate.

Fracture strain was found to strongly increase with decreasing grain size at higher test temperatures (480°C) for 7064 Al/SiC, but the behavior became more complicated at lower temperatures (350°C or below). Overall ductility, however, increased and flow stress decreased with decreasing grain size even at the lower temperatures. This grain size dependence at temperatures well below that where diffusional creep is important suggests an important role of high angle grain boundaries on intermediate temperature creep.

3.1.3 Part II. Creep of High Temperature Intermetallics

The effects of minor alloying additions on creep resistance of Ti-24Al-11Nb have been studied. The additives were carbon, iron, and silicon. All alloys were beta annealed prior to creep testing, to develop a transformed beta microstructure.

Creep tests were conducted at 600, 675 and 750°C in air. All tests exhibited well defined primary and secondary regimes. Surface cracking of the type observed in creep samples tested to failure in Phase I, and reported by others, was not detected in samples tested only the into steady-state regime. Surface cracking is a function of strain and time at temperature. Surface cracking is not a 'creep mechanism' as has been suggested, but rather occurs when the material has strained well into steady-state or, more likely, into tertiary creep.

There are definite effects of alloying additions on secondary creep rate. The most significant effect was due to silicon at the higher temperatures, where increasing Si reduced the creep rate at all stress levels. The effect of carbon was found to be small, but definite: increasing C reduces secondary creep rates. Iron was effective only at the lowest temperature, where reducing Fe to 0.009 at% (0.01 wt%) decreased creep rates. At the higher temperatures, Fe had essentially no effect on creep.

All the data indicate a single creep mechanism in the temperature regime of 675 - 750°C. The stress exponent values of 3-4, in conjunction with ΔH_c values of 200 - 300



kJ/m, suggest dislocation climb as the most likely rate controlling mechanism. Below 675°C, stress exponent values fall to 1-2, with $\Delta H_c \sim 100$ kJ/m, indicating a change in the (unidentified) rate controlling mechanism.

3.2 Part I. Microstructural Control and Processability in Al Alloys

This section describes the results from Part I, relating microstructural development with deformation processing, and the development of optimum processing schemes for advanced Al alloys. The emphasis in this final report is on results generated since the second Annual Report.²

3.2.1 Background

With the development of rapidly solidified, powder metallurgy Al alloys for high-strength and high-temperature applications, the capabilities of these materials have been pushed significantly forward through recent studies.³⁻⁶ A technology which has not kept pace with these developments is the appropriate low-cost method for fabricating components from these alloys. Consequently, the advantages offered by these materials are being questioned, as the already expensive structural materials require even more expensive fabrication methods. The development of cost-effective processing technologies, such as superplastic forming, isothermal forging, and other types of hot-working operations, is therefore urgently needed to enhance the application of these new-generation alloys. These call for an improved understanding of processability and microstructural models for predicting optimal process conditions and process limits.

Among the recent work on processing of advanced alloys, e.g., Al/SiC and elevated temperature Al alloys, the work of Gegel et al is noteworthy.⁷⁻⁹ By using a streamlined (cosine-shaped) die (as originally developed by Richmond^{10,11} for minimizing center bursting problem in extrusion), Gegel et al have shown that Al alloys containing SiC whiskers could be safely extruded with little whisker damage. This is very useful for producing extrusions from complex materials through reduction of hydrostatic tension in the workpiece which can reduce damage. Gegel et al have also found different microstructural conditions produced within different processing regimes similar to deformation processing maps. While different regimes of behavior are predictable from their dynamic material model based on compression tests, the microstructural development resulting from such



processing and correlation is empirical in nature. Correlations are expected between compression tests as well as streamline die extrusion because both processes are axisymmetric. However, in two important industrial processes, rolling and sheet-metal forming (or superplastic sheet-metal forming), where the stress states are plane strain and biaxial tension, respectively, the microstructural correlations do not agree with axisymmetric processes.¹¹ Since the extent of shear deformation components varies widely between these processes, it is reasonable to expect entirely different processing windows ($\dot{\epsilon}$, T , etc.) for these processes from those for extrusion of similar materials, and these will be explored in this work.

In connection with the development of different microstructures during extrusion, Gegel et al have been able to develop ultra-fine microstructures (subgrain structures) in the advanced Al alloys by a process of dynamic recrystallization by extruding these materials at a high strain rate and a high homologous temperature.¹² Although prior particle boundaries begin to disappear when extrusion is carried out under these conditions, a closer examination reveals faint outlines of continuous oxide film along these boundaries. Streamline die provides uniform shear which is ideal for minimizing whisker damage, but not suitable for dispersion of oxide stringers. To achieve some degree of oxide dispersion, streamline die requires a greater extrusion ratio than a shear face die, since the latter introduces intense inhomogeneous shear. For superplastic forming of the extruded material, fine subgrain structures produced via extrusion could undergo dynamic recrystallization; however, the oxide stringers can adversely influence superplasticity by causing excessive cavitation. Since superplastic sheet forming processes develop more severe tensile conditions at the oxide stringers (causing cavitation) than does isothermal forging or extrusion, overall reductions of roughly 30:1 (extrusion plus thermomechanical processing) involving shear deformation are necessary to sufficiently disperse oxides in the billet.

Improved processability in the new, complex Al alloys could be achieved by: (1) development of a very fine microstructure (subgrain and/or grain structure), and (2) developing new grain boundaries with simultaneous removal of prior particle boundaries (for P/M) or prior ingot structure boundaries (for I/M). The latter takes advantage of precipitation effects available in Al alloy systems, while the former depends, among other things, on the volume fraction and size of dispersoids usually present in Al alloys. The alloys of interest for the present study are: (1) an Al/SiC composite; (2) a second-generation, high-strength P/M Al alloy made by the rapid solidification method, and (3) a high-



temperature P/M Al alloy produced via the rapid solidification method. The Al/SiC composites do offer an excellent combination of strength and elastic modulus; however, fracture toughness and fabricability are important considerations. The high-strength P/M alloy will be used in strength-critical areas where Al-Li alloys cannot be used, and high-temperature Al alloys (Al-Fe-Ce, Al-Fe-Mo, etc.) will be used in areas where temperature requirements are higher, but Ti is underutilized. Because of the pivotal role these alloys are likely to play in aircraft structures in the near future, cost-effective fabrication and processing technologies, such as superplastic forming and hot-forming techniques, must be found. It is also important that such processing does not deteriorate the service properties of the alloys.

A common method of microstructural refinement is static recrystallization of a deformed (rolled) alloy. This uses recrystallization of an alloy which has undergone significant amounts of cold work. Recently, it was found that when ultra-fine dispersoid particles are present (such as Al_3Zr and perhaps $FeAl_3$ and $FeAl_6$), the Zener pinning force exerted on the grain boundaries could be large enough to prevent grain boundary migration and full recrystallization of the alloy. The deformed structure, which primarily consists of subgrains, does exhibit some growth at higher temperatures, but does not form high angle boundaries. When aided by concurrent deformation, these boundaries can become mobile and sweep through other areas to increase misorientation between grain boundaries (continuous dynamic recrystallization). Evidence exists that fine equiaxed subgrain structures could form when the proper combination of extrusion and rolling deformation is used. The efficiency of this substructure formation could be significantly influenced by simultaneous precipitation effects present in Al alloys (since these precipitates can additionally pin the dislocations introduced), and therefore the process temperature may be critical.

3.2.2 Objectives

In the second year of this program, the objective for Part I is to develop a unified approach for deformation and thermomechanical processing of complex Al alloys. Specifically, selected alloys are to be subjected to three-axis plane strain forging and other deformation modes. Characterization of microstructural and crystallographic texture changes, as well as their impact on elevated temperature flow characteristics, are to be documented.



3.2.3 Results, Task 1: Model for Subgrain Superplastic Flow in Al Alloys

3.2.3.1 Introduction

Tensile strains in superplastic flow can be limited either by a low value of the strain-rate sensitivity, m , that is defined as:

$$m = \frac{\partial \ln \sigma}{\partial \ln \dot{\epsilon}} \quad (1)$$

where σ and $\dot{\epsilon}$ are the shear stress and strain rate, or by the nucleation and growth of intergranular cavities.¹³ In the absence of cavitation, fracture occurs by flow localization; and the tensile strain, in a constant strain rate experiment, can be described by:¹⁴

$$\epsilon_f = m \ln \frac{1}{1 - \left(\frac{A_0 - \delta A}{A_0}\right)^{1/m}} \quad (2)$$

where ϵ_f is the strain to failure by localization and $\delta A/A_0$ is the size of the initial defect, expressed as a fraction of the initial cross-section. Equation (2) predicts a rapid increase in tensile elongation with m for example, if $\delta A/A_0 = 0.005$ then m (% elongation) gives the following results: 0.2 (98%), 0.4 (580%), 0.6 (1670%), and 0.8 (5700%). These calculations show that substantial elongations are possible even if m is as low as 0.4. Nabarro-Herring¹⁵ and Coble¹⁶ diffusional creep are credited with the high value of strain rate sensitivity¹⁷⁻¹⁹ in conventional superplastic materials.

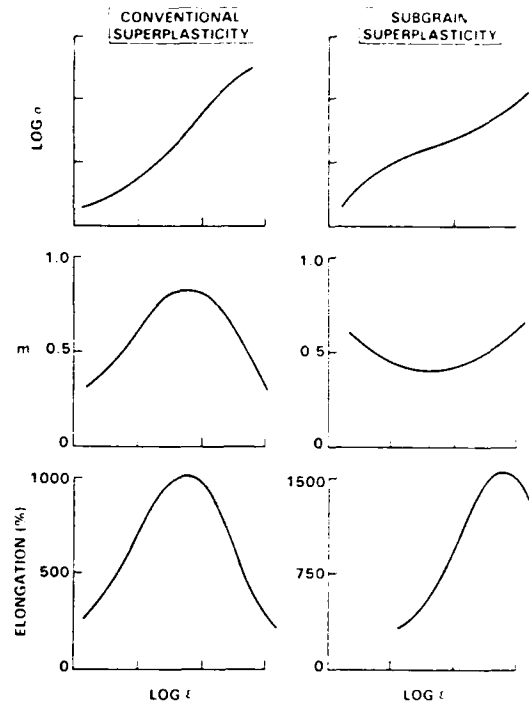
If m is large, the ductility of superplastic materials is often limited by the nucleation and growth of internal cavities. Most commonly the cavities form at grain boundaries. Deformation within hydrostatic pressure can prevent cavity growth,^{13,20,21} restoring the ductility expected from the high m values.

The flow properties of conventional superplastic aluminum alloys are shown by the schematics in Fig. 1a. The stress-strain rate behavior is such that the slope, m , has its maximum value at intermediate strain-rates. The tensile elongations are correlated to m , although in region of maximum 'm' the ductility is usually limited by cavitation.



Fig. 1

Schematics of the contrast between the flow properties of (a) materials with large angle and (b) materials with low angle boundaries. The principal difference is in the curvature of the $m(\dot{\epsilon})$ curves. In the sub-grain materials the best elongations are obtained at high strain rates where m is greater.



The rheology of low angle boundary materials is illustrated in Fig. 1b. Here, m has a minimum at intermediate strain rates. These alloys are also more resistant to cavitation with the result that greater elongations are obtained even though the magnitude of the m -value is smaller than in large angle materials.

In the following sections, we begin by giving details of superplastic flow in conventional and subgrain aluminum alloys. That is followed by the presentation of a model for subgrain superplasticity. Finally possible applications of the model to microstructure design are described.

3.2.3.2 Superplastic Flow and Cavitation in Aluminum Alloys

3.2.3.2.1 Materials

The compositions of the aluminum alloys included in this study are given in Table 1. 7475 and 8091 Al are ingot alloys and the remaining ones are powder processed alloys. The 8091 alloy contains 2.4 wt% lithium to increase the elastic stiffness and reduce density. The processing of the alloys was optimized to produce the smallest grain size because of the sensitivity of diffusional creep to the grain size. The details of processing are given in Refs. 22-27.



Table 1
Composition of Aluminum Alloys

Alloy	Zr	Cr	Co wt %	Li	Zn	Mg	Cu	Al	Processing Ref. #
7475	-	0.2	-	-	6.0	2.5	1.5	bal.	22,23
PM64	0.2	0.12	0.2	-	7.2	2.4	2.0	bal.	24
D19	0.3	0.3	-	-	7.1	2.5	1.9	bal.	25,26
8091	0.15	-	-	2.4	-	0.8	2.0	bal.	27
CU78	Al-8Fe-4Ce								present work

The alloys in Table 1 contain a variety of intermetallic dispersoids which play a role in grain refinement and subgrain development. The chromium intermetallics are 0.1 to 1.0 μm in diameter - a micrograph is given in Fig. 2a - and have a wide range of composition.

In contrast, the ZrAl_3 intermetallics are line compounds and are finely dispersed in D19 and other alloys having a particle size of ~ 20-50 nm as seen in Fig. 2b.

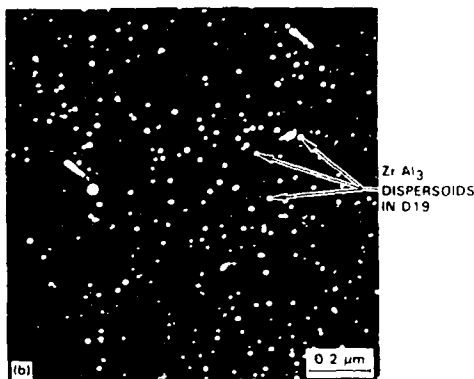
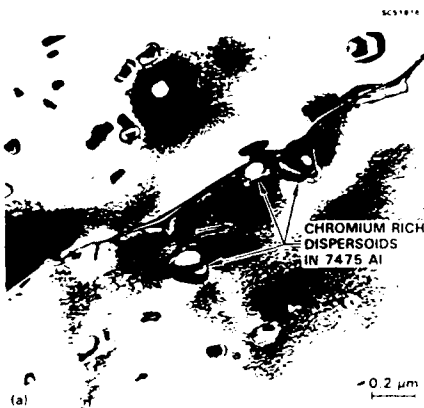


Fig. 2

Transmission electron micrographs of intermetallic dispersoids of (a) Cr-rich compounds in 7475, and (b) ZrAl_3 in D19. The ZrAl_3 dispersoids are about ten times smaller than the Cr-rich dispersoids.



The difference between these two classes of intermetallics can be understood from the phase diagrams. The high melting point and narrow solid solubility in $ZrAl_3$ are responsible for the fine dispersion. The small scale of this dispersion apparently is required to stabilize the subgrain structure. Among these alloys, only D19, which contains the highest zirconium; and CU78, which contains a large volume fraction of intermetallics, show subgrain superplasticity.

3.2.3.2 Rheology

Since the alloys had different grain sizes and were tested at different temperatures, the data were normalized according to the equation for diffusional creep so that the important differences in the rheology of the alloys could be understood. The equations for N-H and Coble creep were written in the following form:

$$\frac{\dot{\epsilon}}{\frac{D_l}{d^2} + \frac{\pi \delta D_b}{d^3}} = \frac{42\Omega}{kT} \cdot \sigma \quad (3)$$

where D_l is the lattice diffusion coefficient, δD_b is boundary width times the boundary diffusion coefficient, and d is the grain size. The left side of Eq. (3) is nondimensional; on the right side Ω is the atomic volume. The diffusion data used by Frost and Ashby,^{28,29} were also used here, which are as follows: $D_l = (1.7 \times 10^{-4}) \exp(-142 \text{ kJ mole}^{-1}/RT) \text{ m}^2 \text{ s}^{-1}$ and $\delta D_b = (5.0 \times 10^{-14}) \exp(-84 \text{ kJ mole}^{-1}/RT) \text{ m}^3 \text{ s}^{-1}$.

The effectiveness of the grain size normalization is illustrated in Fig. 3 where flow stress data for 7475 aluminum at 516°C for $d = 12.3 \text{ } \mu\text{m}$ to $69.4 \text{ } \mu\text{m}$ is plotted with and without normalization. Reasonably good agreement that spans three to four orders of magnitude in strain rate and two to three orders of magnitude in stress is obtained.

When the normalization is extended to all alloys for all temperatures and grain sizes quoted in Table 1, the result shown in Fig. 4 is obtained. It shows two groups of behavior exemplified by conventional alloys on the right and the subgrain alloys on the left. The alloy CU78, which contains nearly 10 vol% of intermetallics, also fits the subgrain behavior even though it does not contain zirconium.



Fig. 3

Normalization of $\sigma(\dot{\epsilon})$ data for 7475 for different grain sizes using Eq. (3). The experimental curves appear to merge into a master curve when the strain rate is normalized with respect to the grain size.

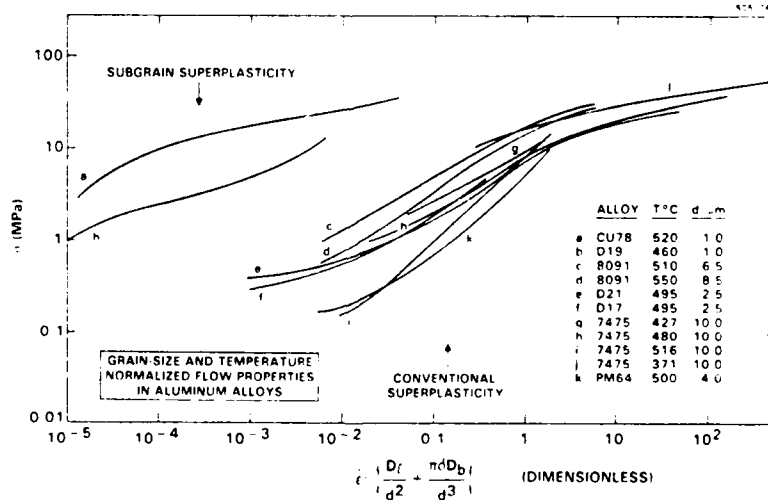
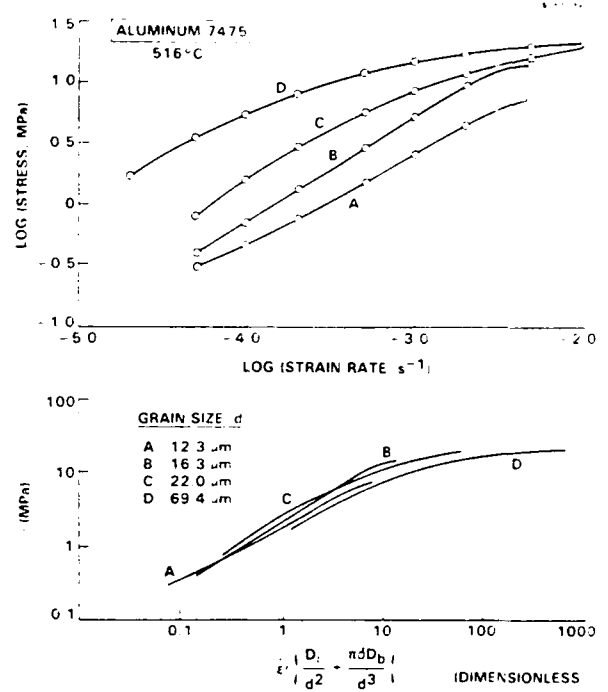


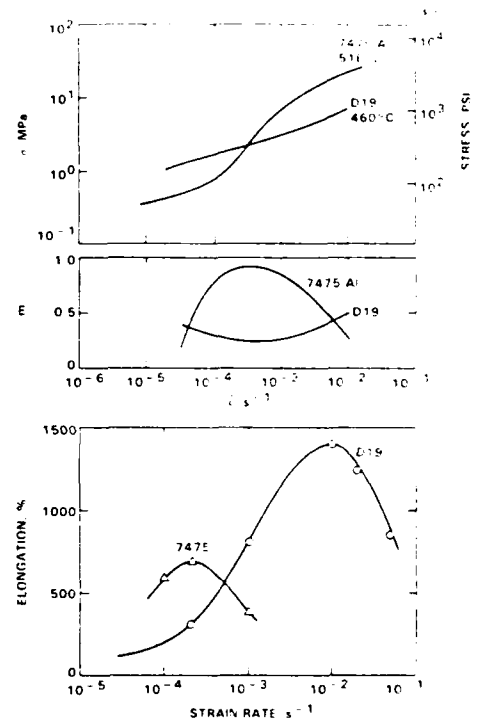
Fig. 4 $\sigma(\dot{\epsilon})$ data for several aluminum alloys were the $\dot{\epsilon}$ has been normalized for differences in grain size and temperature.



The two types of rheology differ as follows: (a) the magnitude of the relative flow stress is one to two orders of magnitude greater for the subgrain materials; and (b) the curves for m -values show a minimum with strain rate in subgrain superplasticity and a maximum in conventional superplasticity. Experimental data for 7475 and D19 alloys are summarized in Fig. 5, which shows the change in the curvature of the $m(\dot{\epsilon})$ curves. Note also that the elongations in D19 were greater, in spite of the lower magnitude of the m -value, because of the greater cavitation resistance of low angle boundaries.

Fig. 5

Experimental data for a material with large angle boundaries (7475) and low angle boundaries (D19) showing the difference in the curvature of the $m(\dot{\epsilon})$ curves.



3.2.3.2.3 Grain Boundary Structure

The significant difference between the two types of materials lies in the structure of grain boundaries. In one case, the majority of the boundaries were low angle while in the other class they were large angle. Typical angle distributions for the two cases are shown in Fig. 6. Interestingly, when the D19 material is processed to increase the grain boundary misorientations, its flow behavior changes from subgrain to conventional superplasticity; this can be appreciated in Fig. 4 where D21 and D17 materials show large angle behavior. These alloys had the similar composition as D19 but were processed to contain large angle boundaries.³⁰

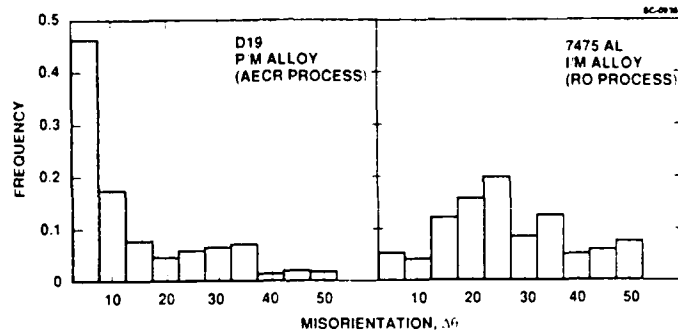


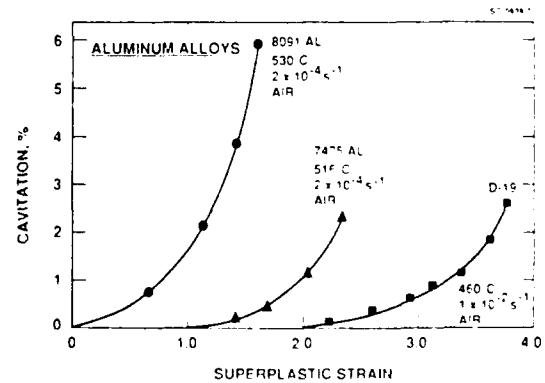
Fig. 6 Distribution of grain boundary misorientations in the subgrain (D19) and other materials.

3.2.3.2.4 Cavitation

The change in volume with strain in a simple uniaxial tensile test is one measure of cavitation in superplastic materials. The results from such experiments for three alloys are shown in Fig. 7. They illustrate the remarkable cavitation resistance of the D19 material; it cavitates less even though the temperature is lower and the strain rate is higher.

Fig. 7

Evidence of lower cavitation in D19 as compared to 7475 or 8091.



This behavior can be explained in terms of a cavity nucleation model where the activation barrier for nucleation is interface energy dependent.²⁶ In this scenario the lower energy of the low angle boundary would substantially lower the probability of cavity nucleation.



3.2.3.3 A Model for Subgrain Superplasticity

The experimental results described in the previous section show that the unusual rheology of the D19 alloy is most likely related to the low angle structure of grain boundaries. Such boundaries can be described by dislocation arrays.³¹ The model presented here invokes a kinetic equilibrium between the dislocations arriving and leaving the subgrain boundaries. The concept is illustrated in Fig. 8. In the model the mobility of the dislocation is controlled by the size and spacing of the intermetallic dispersoids, while the emission rate of the dislocation depends upon the interaction energy between a dislocation and the sub-grain boundary.

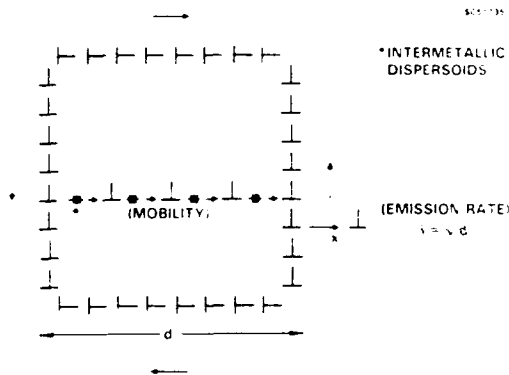


Fig. 8

Description of the model proposed to explain subgrain superplasticity. The steady state deformation obtains when the emission rate of dislocations from the boundaries is equal to the arrival rate of dislocations. The intermetallic dispersoids influence the mobility and therefore the arrival rate of dislocations.

First, we calculate the emission rate of dislocations, I , from dislocation walls under the influence of an applied shear stress, σ . The interaction energy, ΔE , as a function of the distance from the dislocation wall, x , consists of two parts: ΔU , the interaction energy in the absence of applied stress, and ΔW , the work done by external stress as the dislocation moves and produces external strain. ΔE , ΔU and ΔW can be normalized by a quantity, ΔE_0 , such that:*

$$\Delta E_0 = \frac{Gb^2}{2\pi(1-\nu)} \quad (4)$$

*Symbols are defined in Section 3.2.3.6.



where G is the shear modulus, γ is the Poisson's ratio, and b is the Burger's vector. The normalized quantities are written as $\overline{\Delta E}$, $\overline{\Delta U}$ and $\overline{\Delta W}$ and are defined as:

$$\overline{\Delta E}, \overline{\Delta U} \text{ and } \overline{\Delta W} = \frac{\Delta E}{E_0}, \frac{\Delta U}{E_0} \text{ and } \frac{\Delta W}{E_0}. \quad (5)$$

The quantity ΔU has been explicitly derived in Ref. 12 and $\Delta W = \sigma b x$, where σb is the force on the dislocation. Since moving the dislocation out of the wall increases the energy of the system, whereas the applied stress reduces the free energy by doing work on the system, we have that $\Delta E = \Delta U - \Delta W$. Substituting for ΔU from Ref. 12 we obtain that

$$\overline{\Delta E} = \overline{\Delta U} - \overline{\sigma} \overline{x} \quad (6)$$

where

$$\overline{\Delta U} = \ln(\sinh \pi \overline{x} \Delta \theta) - \pi \overline{x} \Delta \theta \coth(\pi \overline{x} \Delta \theta) + \ln \frac{e}{\pi \Delta \theta} \quad (7)$$

where σ has been normalized as follows:

$$\overline{\sigma} = 2\pi(1-\gamma) \frac{\sigma}{G}, \quad (8)$$

x has been normalized with respect to b :

$$\overline{x} = \frac{x}{b} \quad (9)$$

and where $\Delta \theta$ is the lattice misorientation angle that is related to b and the spacing between the dislocations, h :

$$\Delta \theta = \frac{b}{h} \quad (10)$$

The activation energy barrier for the escape of a dislocation from the dislocation wall is equal to the maximum in ΔE with respect to x . The position of the peak, \overline{x}_c , for a given $\overline{\sigma}$ is obtained by differentiating Eq. (6) and equating to zero, which gives the following result:

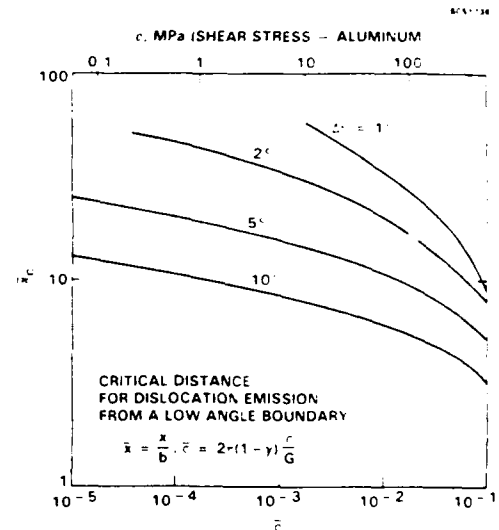


$$\bar{\sigma} = \frac{1}{\bar{x}_c} \left(\frac{\pi \bar{x}_c \Delta\theta}{\sinh \pi \bar{x}_c \Delta\theta} \right)^2 \quad (11)$$

A plot of \bar{x}_c vs $\bar{\sigma}$ is given in Fig. 9. As expected, it shows that the critical distance decreases at higher applied stress since the work done by the applied stress is equal to its product with the critical distance. The interesting result in Fig. 9 is that the stress required for dislocation escape at a given distance decreases as the angle of the boundary increases. The result is nonintuitive since the higher density of dislocations in boundaries with larger angles would have been expected to pin the dislocation more securely.

Fig. 9

The change in the critical distance for dislocation emission from a boundary of misorientation $\Delta\theta$, at different levels of applied stress. Note this distance varies from about 10 to 25 atom spacings.



The emission rate of dislocations can be described by kinetic theory. If ν_0 is vibrational frequency of dislocations, then the emission rate is the difference between the forward and backward jumps:

$$\dot{I} = \nu_0 \left[e^{-\frac{-(\Delta U_c - \sigma x_c)b}{kT}} - e^{-\frac{-(\Delta U_c + \sigma x_c)b}{kT}} \right] \quad (12)$$

The exponential factors are multiplied by a unit atomic length of the dislocation, assumed here to be equal to the Burger's vector. Normalizing temperature according to the equation:



$$\bar{\tau} = kT / \left(\frac{Gb^3}{2\pi(1-\gamma)} \right) \quad (13)$$

and rearranging Eq. (12) leads to:

$$\dot{\epsilon} = v_0 \exp \frac{-\bar{\Delta U}_c}{\bar{\tau}} \times 2 \sinh \frac{\bar{\sigma} \bar{x}_c}{\bar{\tau}} \quad (14)$$

Although in the strict sense $\bar{\Delta U}_c$ is stress dependent, numerical analysis in the stress range $10^{-3} < \bar{\sigma} < 10^{-1}$ shows that $\bar{\Delta U}_c$ is essentially constant and is approximately equal to $\bar{\Delta U}_c = \epsilon n (e/2\pi\Delta\theta)$. With this approximation we write Eq. (14) in the following form:

$$\dot{\epsilon} = 2v \sinh \frac{\bar{\sigma} \bar{x}_c}{\bar{\tau}} \quad (15)$$

where $v = v_0 \exp (-\bar{\Delta U}_c/\bar{\tau})$.

We now proceed with a calculation of the arrival rate of dislocations at the dislocation walls. The velocity of dislocations is assumed to be controlled by the rate of climb over the intermetallic dispersoids. In such a case a linear relationship between velocity and the force on the dislocation may be assumed:

$$v = \sigma b M \quad (16)$$

where M is the mobility, σb is the force per unit length and v is the velocity of the dislocation. The arrival rate of the dislocations, \dot{A} , is then given by:

$$\dot{A} = \frac{v}{d'} \quad (17)$$

where d' is the subgrain size. Setting $\dot{\epsilon} = \dot{A}$ gives the condition for steady state deformation and leads to the following result for the steady state subgrain size:

$$\frac{d'}{d'_0} = \frac{\bar{\sigma}/\bar{\tau}}{\sinh(\bar{\sigma} \bar{x}_c/\bar{\tau})} \quad (18)$$

where



$$d'_0 = \frac{kTM}{2vb^2} \quad (19)$$

It depends upon the microstructure since the mobility will be controlled by the distribution of the intermetallic dispersoids.

Plots of Eq. (18) in Fig. 10 show the change in the subgrain size with stress, temperature and misorientation. Three temperatures, 340°C, 520°C and 650°C, are considered. The last temperature, being close to the melting point, is experimentally unrealistic, and is included only to illustrate that the subgrain structure becomes increasingly unstable as the temperature increases. The other two temperatures span the superplastic forming range for the D19 aluminum alloy. The plots also show that the subgrains can be expected to be dynamically stable only in a certain regime of stress. The condition for stability is assumed to be that the subgrain size must decrease with increasing stress, which is a feature of dislocation creep.

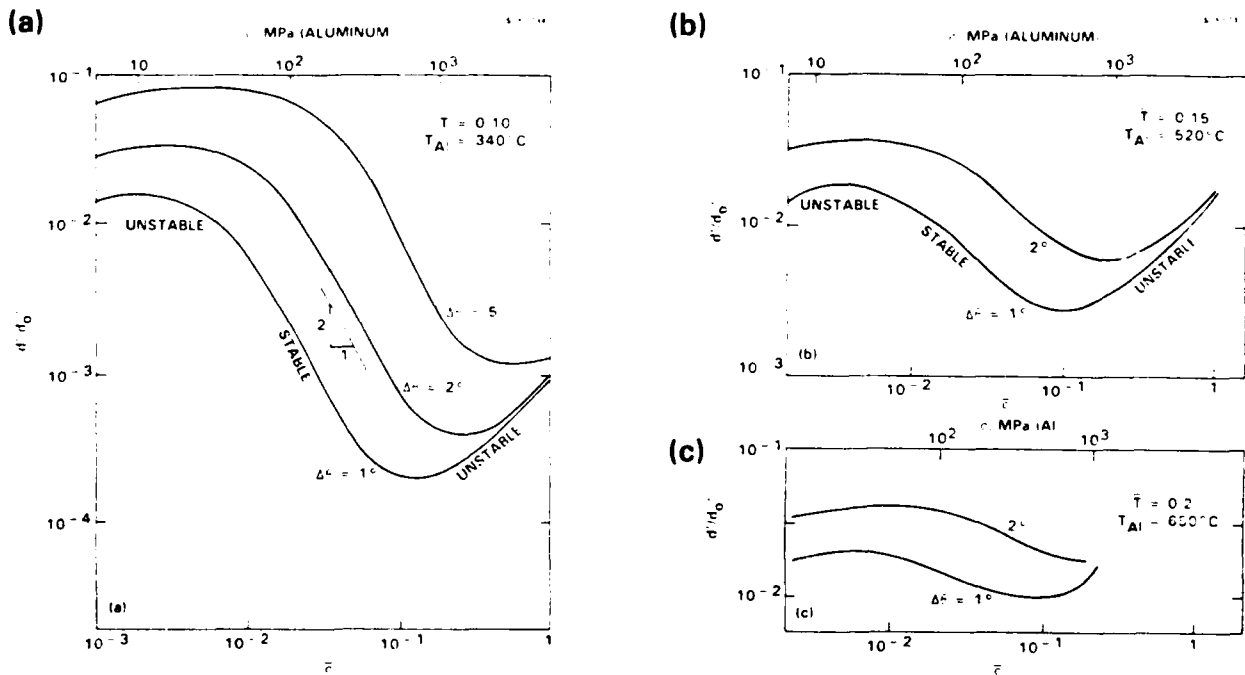


Fig. 10 Variation of subgrain size with stress at (1) 340°C, (b) 520°C, and (c) 650°C.



In Fig. 10 we note that $d' \propto \sigma^{-2}$ is valid only at intermediate temperatures ($\sim 340^\circ\text{C}$ in aluminum) and in a restricted range of stress. If the stress is much higher or much lower, then d' becomes less sensitive to σ . This result may be significant in the context of dynamic recrystallization where the subgrain size has been shown to follow σ^{-2} dependence³² and where the grain size has been found to be characteristic of deformation rate and temperature.³³

We now proceed to analyze the stress-strain rate behavior, keeping a special interest in studying the change in the strain rate sensitivity with strain-rate so a comparison can be made with the experimental results presented in Figs. 4 and 5.

The strain rate $\dot{\epsilon}$ may be assumed to be related to the dislocation density ρ , by the equation $\dot{\epsilon} = \rho b v$. Since the boundaries are assumed to consist of lattice dislocation arrays, it is readily shown that $\rho = (2\Delta\theta/bd')$ where the subgrains are assumed to be square shaped. With these two equations and substituting for v from Eq. (16) leads to the following expression for the strain-rate:

$$\dot{\epsilon} = 2Mb\Delta\theta \frac{\sigma}{d'} \quad (20)$$

Note that M and $\Delta\theta$ are microstructural parameters that depend on processing history. The subgrain size, d' , however, is stress dependent. Equation (20), therefore, does not predict a linear stress dependence. To obtain the stress dependence, we substitute for d' from Eq. (18) and combine that result with Eq. (19) to obtain:

$$\dot{\epsilon} = 4v\Delta\theta \sinh\left(\frac{\bar{\sigma} \bar{x}_c}{\bar{\tau}}\right) \quad (21)$$

where \bar{x}_c is related to $\bar{\sigma}$ by Eq. (11). The combination of Eqs. (11) and (21) were solved numerically, and the predicted stress-strain rate behavior is plotted in Fig. 11. Two temperatures and three boundary angles are considered. Nondimensional parameters are used for strain-rate and for stress, the advantage being that they lead to the prediction of the magnitude of the strain rate sensitivity, m , and its change with strain-rate, both of which can be compared with experiment, without having the values for material parameters.

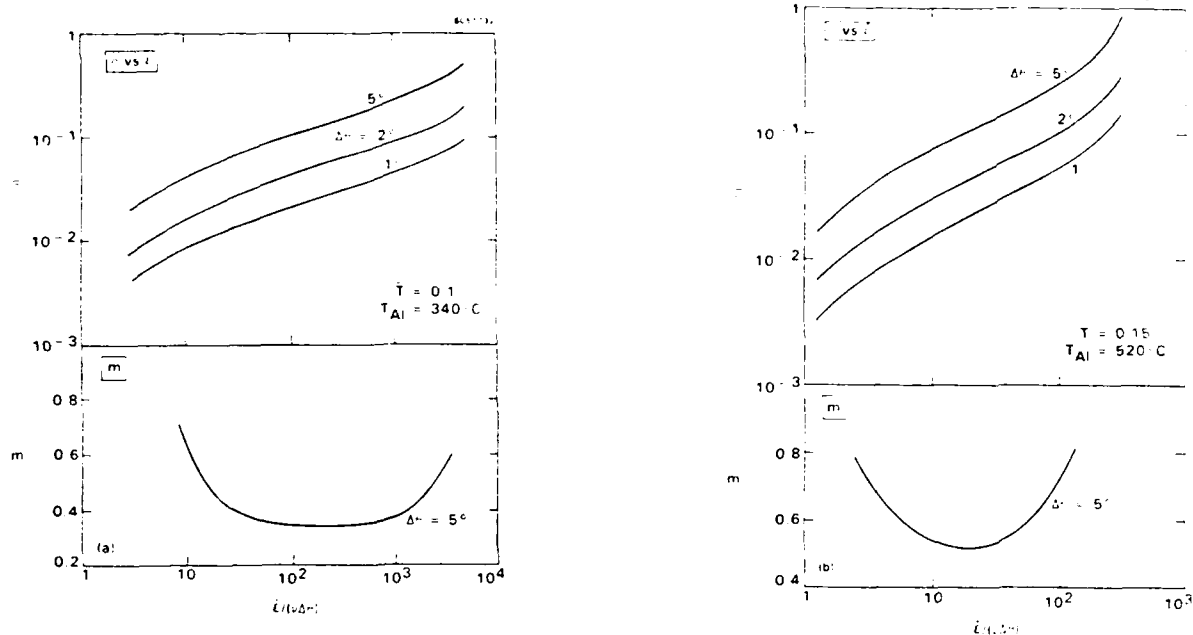


Fig. 11 The predicted shape of $\sigma(\dot{\epsilon})$ curves for different misorientations at (a) 340°C and (b) 520°C.

The most interesting result in Fig. 11 is that m shows a minimum at intermediate strain rate, a feature that distinguishes subgrain superplasticity from conventional superplasticity, as seen in Fig. 5. The theory also predicts m values that are less than 1, which is consistent with experiment.

The theory suggests that the subgrains will be stable only in a limited regime of strain-rate and temperature, as shown in Fig. 10. Furthermore, within the stable regime the value of m and the subgrain size can change with applied stress. It is interesting that Argon³⁴ has shown that in random dislocation arrangements, the interaction between dislocations leads to $m = 1/3$. We also calculate m to be close to this value in the middle of the stable regime and at intermediate temperatures. The importance of the microstructure in stabilizing the subgrain boundaries is discussed in the next section.

3.2.3.4 Discussion

The curves in Fig. 10 show that the subgrain structure is likely to be stable when the normalized subgrain size lies approximately in the following range:



$$10^{-2} > \frac{d'}{d'_0} > 3 \times 10^{-3} \quad (22)$$

The upper bound is limited by the arrival rate of dislocations at dislocation walls. Beyond the upper limit the emission rate of dislocations is faster than the arrival rate. Below the lower bound the arrival rate is faster. Physically, this means that if the strain rate is too slow then the subboundaries gather dislocations and change into large angle boundaries. On the other hand, if the deformation rate is too fast, then the low energy arrangement of dislocation arrays cannot be sustained and the subgrain boundaries melt into the single crystal grain.

The interesting question is how can the microstructure of the alloy be controlled in order to stabilize the subgrain boundaries. At least guidelines to the question can be obtained by substituting for d'_0 into Eq. (21) which gives that:

$$10^{-2} > \frac{2vb^2}{kT} \cdot \frac{d'}{M} > 3 \times 10^{-3} \quad (23)$$

The parameters in $2vb^2/kT$ include basic properties of the material that cannot be changed. However, M can be controlled by varying the size and spacing of intermetallic dispersoids. Also, the temperature dependence of M is expected to be related to boundary or lattice self diffusivity. Experience with aluminum alloys shows that very fine intermetallic dispersoids, on the scale of 10-100 nm, are effective in stabilizing the subgrains. Since those intermetallics form coherent interfaces, M is expected to be proportional to lattice diffusivity.

An expression for M can be obtained from the solution for grain boundary sliding in a boundary that contains particles, if we assume that all the work is expended in the climb of dislocations around the hard intermetallic particles and that climb is diffusion controlled. In that case, we have $v = \dot{u}b/\lambda$ where v is the dislocation climb velocity and λ is the spacing between the particles. The basis of this equation is that as one dislocation climbs over one particle, it effectively moves through a distance λ which results in relative displacement of b across the glide plane. Substituting this equation into the result in Ref. 35 gives the following expressions for dislocation mobility:

$$M_b = \frac{8b\delta D_b}{f\rho kT} \quad (24)$$

and



$$M_l = \frac{1.6 b D_l}{f k T} \quad (25)$$

where M_b and M_l are the interface diffusion controlled and lattice diffusion controlled mobilities. The particle size of the intermetallics is p and their volume fraction is f . While Eq. (25) does not show particle size dependence, it does remind us that larger particles may become incoherent leading to a switch from lattice diffusion control to boundary diffusion control. If that occurs, then mobilities may become too fast to sustain a subgrain structure.

Substitution of Eq. (25) into Eq. (1a) gives the following equation for the strain rate:

$$\dot{\epsilon} = 3.2 \frac{\sigma b^2}{k T} \cdot \frac{\Delta \theta D_l}{d' f} \quad (26)$$

The equation permits a comparison between the theoretical and the experimental magnitudes of the strain rate. Note that it does not predict a linear stress-strain rate dependence since d' is a function of σ as given by Eq. (18).

Substituting the values for aluminum into Eq. (26) as follows: $T = 460^\circ\text{C}$, $\sigma = 10 \text{ MPa}$, $\Delta \theta = 1^\circ$, $f = 0.01$, and $d' = 1 \text{ } \mu\text{m}$ gives $\dot{\epsilon} = 5.8$, which, from Fig. 5, is two orders of magnitude faster than experiment. A possible explanation for the discrepancy is that the diffusivity in the experimental alloy was slower than in pure aluminum because of impurities.

3.2.3.5 Summary

Phenomenological experiments on a variety of aluminum alloys have shown that a special type of superplastic flow occurs when the boundaries are predominantly low angle. The strain rate sensitivity, m , of the subgrain material is generally lower than that of conventional superplastic aluminum alloys, but is still high enough to produce large strains without strain localization. More interesting is the change in m with strain-rate: in the subgrain material it goes through a minimum at intermediate strain rates while the conventional materials show a maximum. As a result, high values of m , which yield the best elongations, obtain at high strain rates in the subgrain material.

The model developed to explain this behavior invokes a kinetic equilibrium between the arrival rate and the emission rate of dislocations at low angle boundaries. The emission rate depends on the angle of the subboundary and the elastic constants while the



arrival rate depends on the mobility of the dislocation which is controlled by the size and spacing of coherent intermetallic dispersoids in the lattice. The subgrain structure is stable only within a certain range of strain rate. If the strain rate is too slow then the arrival rate of dislocations exceeds the emission rate and the subboundaries gradually grow into large angle boundaries. If the strain rate is too high, then the emission rate is faster and the low angle boundaries melt into the crystal grains. Within the stable range, the m value changes and the model predicts a broad minimum in m , which agrees with experiment. The magnitude of m in the minimum is estimated to be 0.4 to 0.5 which is consistent with experiment.

The interesting application of this work could be to develop alloys that can be deformed superplastically at strain rates that exceed 1 s^{-1} by controlling the size and spacing of dispersoids and the structure of interfaces that the dispersoids form with the matrix.

The model presented here may also be relevant to dynamic recrystallization where a steady state subgrain structure can develop during deformation. So called transient superplasticity³⁶ where the initial subgrain structure leads to limited superplasticity before it changes to large angle boundaries may also be related to the present discussion.

3.2.3.6 Symbols, Definitions and Units

σ	:	shear stress (MPa)
ϵ	:	shear strain
$\dot{\epsilon}$:	shear strain rate (s^{-1})
G	:	shear modulus (MPa)
γ	:	Poisson's ratio
m	:	strain rate sensitivity $m = \frac{d \ln \sigma}{d \ln \dot{\epsilon}}$
ϵ_f	:	strain to failure
D_l	:	lattice diffusion coefficient ($\text{m}^2 \text{s}^{-1}$)
D_b	:	boundary diffusion coefficient ($\text{m}^2 \text{s}^{-1}$)
δ	:	boundary thickness (m)
b	:	Burger's vector (m)
T	:	temperature (K)
k	:	Boltzmann constant (J/K)
d	:	grain size (m)
d'	:	subgrain size (m)



ΔE	:	Interaction energy (J)
ΔU	:	Interaction energy in the absence of stress (J)
ΔW	:	work done by the applied stress (J)
ΔE_o	:	normalizing parameter ($Gb^2/2\pi(1-\gamma)$)
$\overline{\Delta E}, \overline{\Delta U}, \overline{\Delta W}$:	normalized energies
v	:	velocity of dislocation
x	:	distance of dislocation from cell wall (m)
x_c	:	critical distance of dislocation from cell wall (m)
\overline{x}	:	normalized distance of dislocation (x/b)
\overline{x}_c	:	normalized critical distance of dislocation
h	:	spacing between the dislocations (m)
\overline{h}	:	normalized spacing between the dislocations ($=h/b$)
$\Delta\theta$:	misorientation ($=b/h$)
$\overline{\sigma}$:	normalized stress ($\overline{\sigma} = 2\pi(1-\gamma) \frac{\sigma}{G}$)
I	:	emission rate of dislocations (s^{-1})
A	:	arrival rate of dislocations (s^{-1})
M	:	mobility of dislocation ($Pa^{-1}s^{-1}$)
ν_o	:	vibrational frequency of dislocation (s^{-1})
\overline{T}	:	normalized temperature ($kT/[Gb^3/2\pi(1-\gamma)]$)
p	:	particle size (m)
f	:	volume fraction of particles
λ	:	spacing between particles (m)

3.2.4 Results, Task 2: Effect of Processing on High Temperature Flow in Al Alloys

3.2.4.1 Introduction

In this part of the program, microstructural control and processability in advanced aluminum alloys were investigated, and the effect of microstructural conditions on widening the processing windows, within which material could be successfully processed, was determined.

One of the objectives of this research was to seek certain deformation path history which would either enhance the processability of the materials at a lower cost or clarify reasons for differences between various process paths. The available approaches in-



clude isothermal warm rolling, thermomechanical treatment, and forging along three orthogonal axes of the workpiece. It was to be expected that through these deformation processes, the microstructures would undergo changes which would eventually lead to an improved ductility and therefore processability of the materials.

The phenomenology of deformation at elevated temperatures for most metallic alloys has certain key features. For a fixed temperature and strain rate of deformation, there exists a steady state subgrain size. When microstructural size changes during deformation, subgrain size either increases with imposed strain (when existing subgrain size is smaller than the steady state value) or decreases with strain (when existing subgrain size is larger than the steady state substrate size). Obviously, the latter is the goal of our processing studies, and this calls for maintaining a low working temperature or a high strain rate, since both parameters cause a decrease in grain size.

Plastic flow behavior can also be influenced by grain or subgrain misorientation. This quantity also decreases with increasing strain, if deformation occurs at temperatures low enough for the statistical storage of dislocations. On the other hand, when dynamic recovery occurs, subgrain misorientation and subgrain size increase with strain. This process, which is marked by a reduction in dislocation density, represents a steady state grain size and misorientation which are larger than the starting values.

Earlier in the program, it was theorized that highly refined substrate structure could be achieved through an appropriate deformation processing cycle.² When strain rates are lower, steady state is achieved at a higher level of strain, and therefore continued increase in misorientation can occur with increasing strain if sufficient dynamic recovery occurs. This leads to a coarser grain size, unless a very high level of strain (> 6) is imparted to the workpiece. To achieve this in a bulk material, a method has been devised which involves alternate forging along three orthogonal directions of a billet in several passes so that the billet does not change its overall shape, but allows the accumulation of a large amount of shear strain.

Further understanding of microstructural changes in light of processing conditions is certainly needed to improve the processability of these advanced aluminum alloys. In this report, the effect of various thermomechanical processing techniques on microstructures and subsequently on processability of the above materials is discussed. The results of microstructural characterization and tensile and compression tests used to characterize the de-



formation behavior of these materials at elevated temperatures are also discussed, and the correlation between microstructural parameters and materials processability is interpreted.

3.2.4.2 Materials for Study

This study concentrated on materials having heterogeneous microstructures, such as a high-strength aluminum alloy reinforced with SiC particulate and Al-8-Fe-4Ce alloy which contained fine particles of $Al_{10}Fe_2Ce$ and $Al_{13}Fe_4$. An alloy that was previously determined to have a significant potential for high strength and toughness, rapidly solidified 7064 (PM-64) alloy, developed by Kaiser Aluminum Corporation, was selected as the matrix for this particulate composite. Composites were fabricated by blending 15 v/o of 1200 mesh SiC particulate with 7064 aluminum alloy powder, hot-outgassing and hot-pressing, followed by extrusion in a rectangular die (18:1 extrusion ratio). The high-temperature aluminum alloy, Al-8Fe-4Ce (CU78), developed by Alcoa under AFWAL contract, was selected. This alloy has shown promise for use at service temperatures as high as 500°F and might be a candidate materials for next generation aircraft. This material was produced in extruded plate and rolled sheet form. The chemical compositions of the materials studied in this report were given in Table I.

The as-received 7064 Al/SiC included a section of as-extruded bar of 25.4 mm (1 in.) thick and two pieces of three-axis forged disks (the imposed true strain of 6.4 during the forging process) with a thickness of 2 mm (0.08 in.). These latter items were forged at Rockwell Science Center. Compression specimens were made using the as-received material. Two forms of Al-8Fe-4Ce were received, the 2.54 mm (0.1 in.) thick rolled sheet which was subject to further rolling as described in the next section, and a piece of extruded bar from which the compression specimens were machined.

3.2.4.3 Experimental Methods: Processing and Testing

Various deformation processing techniques were utilized to process these aluminum alloys. They included warm rolling under isothermal conditions, thermomechanical treatment (TMT), and forging along three orthogonal directions of the workpiece. These processing methods provided an opportunity to control microstructures of the materials along different strain paths, so that the processability of the materials could be assessed. All three methods were applied to 7064 Al/SiC alloy and the warm rolling and the three-axis



forging were performed on Al-8Fe-4Ce alloy. Other methods employed included isothermal compression of the as-extruded materials at elevated temperature.

3.2.4.3.1 Warm Rolling Under Isothermal Conditions

Isothermal warm rolling of 7064 Al/SiC was performed in as-extruded condition and that of Al-8Fe-4Ce alloy in as-rolled condition, at the Department of Materials Science and Engineering, the University of Michigan. Facilities used included a two-high (140 mm in diameter) rolling mill and a heating furnace capable of use to 1200°C.

As-extruded 7064 Al/SiC was rolled to 94% thickness reduction, equivalent to a true strain of 2.8, at rolling temperatures of 250°C and 350°C, respectively. The samples were first preheated in the furnace to the rolling temperature. Thermocouples were attached directly to the sample to monitor temperature and assure isothermal conditions. Stainless steel packs were used to minimize heat loss of the billet during rolling. To avoid surface sticking between the sample and the pack, boron nitride powder in ethyl alcohol was coated on the sample surfaces. After each rolling pass, the sample thickness was measured and the rolling reduction calculated. The sample was cleaned for minor cracks and re-packed with the stainless sheet whenever necessary. Then it was reheated to the rolling temperature for the next rolling step. The process was repeated until the total reduction was reached.

A similar rolling procedure was followed for rolling of Al-8Fe-4Ce sheet. The samples were rolled to a total reduction of 66% (1.1 in true strain) at 380°C from a rolled sheet. To avoid cracking, the samples were subject to cross rolling and given no more than 20% reduction for each pass.

3.2.4.3.2 Thermomechanical Treatment (TMT)

This process consisted of four steps as previously developed at the Rockwell Science Center.³⁷ First, the as-extruded samples were solution treated at 480°C for one hour followed by a water quench. They were then overaged at 360°C for eight hours and water quenched. Next, the samples were preheated to 250°C and soaked for 30 mins, followed by cross rolling at 250°C. Approximately 20% reduction was given for each path, and a total of 91% rolling reduction (2.4 in true strain) was achieved to ensure grain refinement. As a final step samples were recrystallized at 480°C for 30 mins.



To study the effect of grain size on tensile properties, some of these thermo-mechanically processed samples were given an identical treatment except that the rolling reduction was only 46% (0.6 in true strain). Since the amount of deformation was not sufficient to provide adequate driving force for nucleation throughout the material, a coarser microstructure was obtained. This process is referred to as the coarse grain TMT in the text.

3.2.4.3.3 Three-Axis Forging

Three-axis forging operation was first proposed and performed at Rockwell.³⁸ In this experiment, a block of material was forged in a plane strain die in successive passes along three orthogonal directions. In each pass, two shear planes normal to the plane strain direction were active. By changing the forging axis between passes (each pass imparting a strain of 0.69), all possible shear planes were intersected, and equiaxed dislocation cells and eventually subgrains formed at high levels of strain (> 6). Each deformation stop introduces a truly constrained shear deformation since plane strain conditions are maintained. This method provides a unique way to achieve an extremely high level of plastic strain within the material not possible by other methods.

7064 Al/SiC and Al-8Fe-4Ce alloys were three-axis forged at Rockwell Science Center and eventually flattened in disks by forging for tensile test. For 7064 Al/SiC, the forging operation was carried out at 250°C, and a strain of 6.4 was imparted on the workpiece. The Al-8Fe-4Ce alloy was three-axis forged at 350°C to a true strain of 5.7, and the forged disks were further rolled at the same temperature for an additional 80% in reduction (total true strain of 7.3) to allow making the tensile specimens.

3.2.4.3.4 Tensile Tests

Elevated temperature tensile test conditions are summarized in Table 2. All tests were carried out to fracture in air. The load and displacement were recorded on a chart and values of true stress and true strain calculated from chart records were plotted as stress-strain curves.



Table 2
Summary of Tensile Test Conditions

7064 Al/SiC (as-extruded)

<u>Prior History</u>	<u>Temperature (°C)</u>	<u>Strain Rate (S⁻¹)</u>
Warm Rolled (250°C / ε=2.8)	250	10 ⁻⁴
	350	10 ⁻⁴
Warm Rolled (350°C / ε=2.8)	250	10 ⁻⁴
	350	10 ⁻⁴
	480	10 ⁻⁴
	350	10 ⁻²
Coarse Grain TMT (ε=0.6)	250	10 ⁻⁴
	480	10 ⁻⁴
Fine Grain TMT (ε=2.4)	250	10 ⁻⁴
	480	10 ⁻⁴
3-axis Forged (250°C/ε=6.4)	250	10 ⁻⁴
	350	10 ⁻⁴
	480	10 ⁻⁴

Al-8Fe-4Ce (CU78)

<u>Prior History</u>	<u>Temperature (°C)</u>	<u>Strain Rate (S⁻¹)</u>
Warm Rolled from rolled sheet (380°C/ε=1.1)	480	5x10 ⁻³
	480	5x10 ⁻²
	480	10 ⁻¹
	520	5x10 ⁻³
	520	5x10 ⁻²
	520	10 ⁻¹
3-axis Forged & Warm Rolled (From extrusion) (350°C/ε=7.2)	480	5x10 ⁻³
	480	10 ⁻¹
	520	5x10 ⁻³
	520	10 ⁻¹



3.2.4.3.5 Compression Tests

Constant true strain rate and step strain rate compression tests were performed on cylindrical compression specimens, 10 mm (0.4 in.) in height and 5 mm (0.2 in.) in diameter. All tests were performed on the as-extruded material with the compressive load applied parallel to the primary extrusion direction. Specimens were tested at elevated temperatures and various strain rates (Table 3), and were strained to approximately a true strain of one without fracture.

**Table 3
Summary of Compression Test Conditions**

<u>Materials</u>	<u>Temperature (°C)</u>	<u>Strain Rate (S⁻¹)</u>
7064 Al / 15 v/o SiC (As-extruded)	250	0.0001
	250	0.01
	350	0.0001
	350	0.01
	480	0.0001
	480	0.01
Al-8Fe-4Ce (CU78) (As-extruded)	350	10 ⁻⁵ to 10 ⁻² (step strain rate)
	480	10 ⁻⁵ to 10 ⁻² (step strain rate)
	520	10 ⁻⁵ to 10 ⁻² (step strain rate)
	480	0.005
	480	0.1
	520	0.005
	520	0.1



The purpose of this series of compression tests was to provide a base line for the as-extruded material for comparison with materials processed by other means. It has been found² that strain rate sensitivity, m , begins to increase at higher strain rates ($> 0.01 \text{ S}^{-1}$) for the three-axis forged Al-8Fe-4Ce alloy. To determine the effect of strain rate on m for the as-extruded material, three-step strain rate tests were performed at three different temperatures (250, 350 and 480°C) to cover a wide range of strain rates (10^{-5} S^{-1} to 10^{-2} S^{-1}). For each of the rate steps, the specimen was allowed only a limited amount of plastic deformation before it reached the steady state. Results from these experiments were used to determine the parameters (temperature and strain rate) of subsequent tests.

3.2.4.4 Experimental Methods: Microstructure Characterization

Microstructure characterization was carried out after the various processing steps and also after subsequent mechanical tests to assess the role of deformation on various microstructural features. This was performed by using the NIKON optical microscope and the HITACHI S-520 scanning electron microscope. Subgrain misorientation measurements were performed on the JEOL 2000FX scanning and transmission electron microscope (STEM) of Electron Microbeam Analysis Laboratory, the University of Michigan.

3.2.4.4.1 7064Al/15 v/o SiC

Microsamples Preparation for Microscopy - For each of the tested tensile specimens, microstructural examination was carried out from the gauge section and the grip area which represented a strain of zero. Due to difficulties in revealing grain boundaries of matrix grains through regular etching techniques, samples were briefly solution treated and aged, prior to mounting. This involved a treatment at 480°C for a maximum of 5 mins followed by a water quench. Subsequently, they were aged for 22-24 hours at 160-180°C, allowing reprecipitation along grain boundaries which would be revealed by etching later. While this step does alter the as-deformed microstructure somewhat, the change is believed to be small. To verify if this heat treatment would alter the grain size of the matrix significantly, an identical treatment was repeated on the same sample, and the result did not suggest any substantial change of grain structure. TEM foils were prepared through mechanical grinding and polishing, dimpling, and ion milling processes.

Grain Size Measurement - Grain (and subgrain) size measurement was made from SEM photomicrographs as well as TEM photographs using linear intercept method. For ten-



sile specimens, the grain size of both gauge and grip areas was measured, and for compression specimens, the grain size along the loading axis was measured. The measurements were made in different directions to ensure an average grain size of the sample.

Subgrain size of the 250°C and 350°C rolled materials were measured using TEM micrographs by taking an average of the major and minor diameters of matrix grains multiplied by a factor of 1.414. More than 50 grains were examined for each rolling condition.

Subgrain Misorientation Measurement - To study the microstructure change of the material during processing, misorientation of subgrains was determined by imaging and convergent beam electron diffraction (CBED) techniques. First, a CBED pattern was taken of a subgrain. By knowing the crystallographic orientation of the subgrain from the Kikuchi map for FCC crystals, a low-index crystal plane (e.g., {110} or {100}) was identified by tilting the foil in two directions, and two tilt angles were noted. Then, the same indexed plane was found from a neighboring subgrain and the tilt angles were noted. This process was repeated on 45-50 grains for each rolling condition to ensure the statistical validity of the results. Finally, values of these angles were plotted on a Wulff Net, so that the relative orientation (or misorientation) between neighboring subgrains could be determined.

Figures 12 and 13 illustrate the subgrain structures of the foils rolled 92% at 250°C and 88% at 350°C, respectively, and Fig. 14 is a CBED pattern taken from one of the subgrains indicated by the arrow in Fig. 13. While this method does not distinguish the degree of tilt vs twist at each grain boundary, it does provide an overall measure of misorientation across a grain boundary. For the purpose of examining the role of strain in altering misorientation distribution, this is an adequate measurement.

Distribution of SiC Particulate Clusters - It was observed that the SiC particulate cluster, (i.e., a group of SiC particulates that were agglomerated during the fabrication of the material), underwent a significant shape change as a result of deformation processing. To quantify this change in shape, the following parameters were defined: (1) aspect ratio, defined as a ratio of the length and width of a SiC cluster; (2) area fraction of SiC clusters (%), a ratio of the area occupied by SiC clusters in a given area of the micrograph; and (3) area fraction occupied by SiC particulates in nonclustered areas (%), a ratio of the areas occupied by SiC particulates per unit area where it does not contain obvious SiC clusters. These quantities were determined from optical or SEM microphotographs.

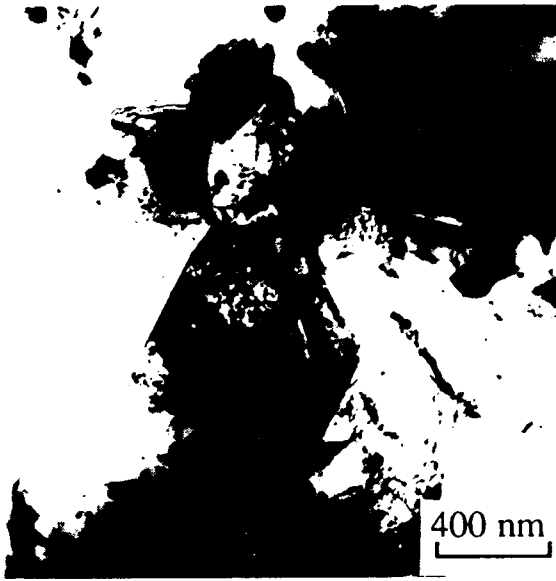


Fig. 12 TEM micrograph of 7064 AlSiC rolled 92% at 250°C.

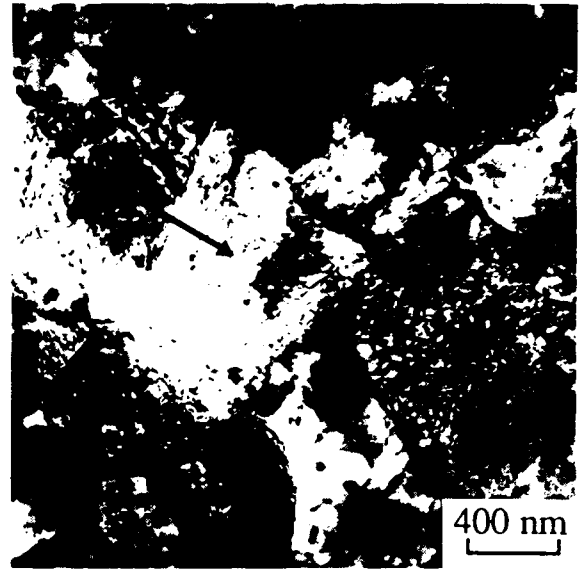


Fig. 13 TEM micrograph of 7064 AlSiC rolled 88% at 350°C.

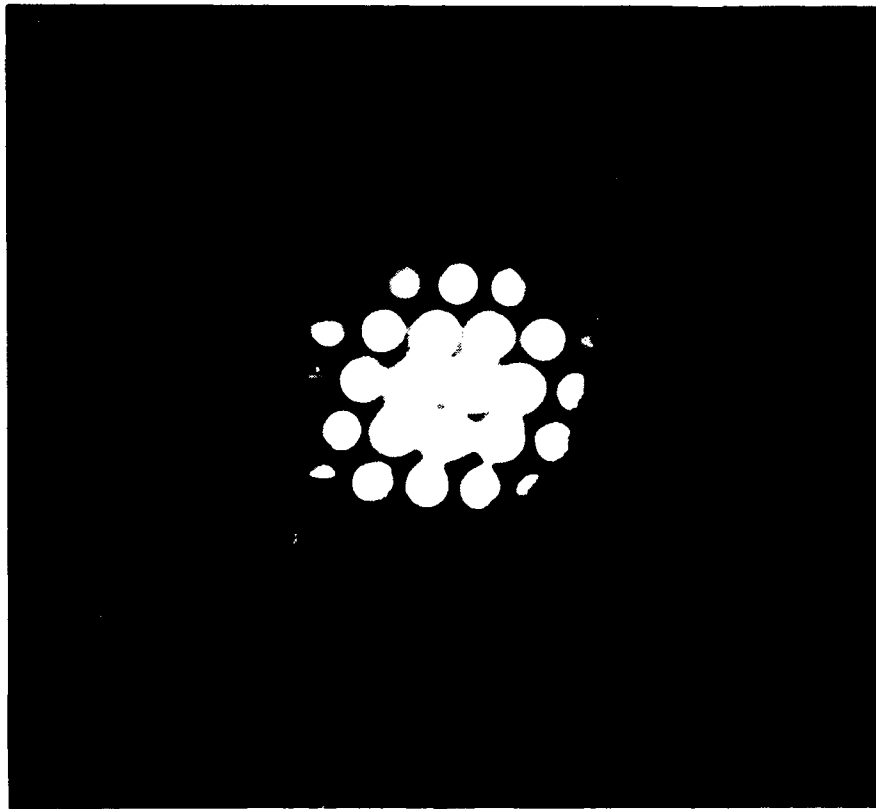


Fig. 14 {112} CBED pattern from grain indicated by arrow in Fig. 13.



3.2.4.4.2 Al-8Fe-4Ce (CU78)

The sample preparation of CU78 was similar to the procedure describe above, except that no heat treatment was given after tensile testing. Optical micrographs were used to determine the microstructure dimension (i.e., subgrain and grain size) using linear intercept method.

3.2.4.5 Results and Discussion

3.2.4.5.1 7064 Al/15 v/o SiC

3.2.4.5.1.1 Microstructure

Grain Size (As-Processed) - Microstructures of as-extruded, warmed rolled, thermomechanically processed, and three-axis forged materials are given in Fig. 15. The matrix microstructure has been significantly altered by these processing methods.

While the grain size of the three-axis forged and thermomechanically treated materials maintained about the same level as that of the as-extruded material, grain coarsening did occur in the warm rolled materials, especially when rolled at 350°C, and in those processed via a coarse grain TMT (Fig. 16). Nonuniform grain structure (or bimodal structure), was observed in the sample rolled at 350°C (Fig. 15(b)), where the coarse matrix grains existed between SiC clusters, and fine grains near the SiC clusters. The coarsening taking place during 350°C rolling is believed to have occurred partly due to the intermediate heating steps during rolling and when the sample was heated to 480°C due to somewhat slower heating rate. The lack of sufficient dislocation density within the material to maintain a finer structure results in areas of grain growth. In the areas where the SiC clusters existed, the particles served as barriers for grain boundaries to migrate, so that the growth was restrained.

The grain size measurements, Fig. 16, suggest that rolling or compressive deformation modes are less homogeneous than three-axis forging in imparting strain within the material. While three-axis forged structure can sustain a heat up to 480°C without showing excessive grain boundary migration and substantial growth, the deformation structure produced by rolling at 350°C or even at 250°C is not capable of this. The steady-state substructure developed at 350°C (warm rolled) is expected to be coarser than that for 250°C warm rolling, due to retention of a greater dislocation density at 250°C. Thus, dynamic

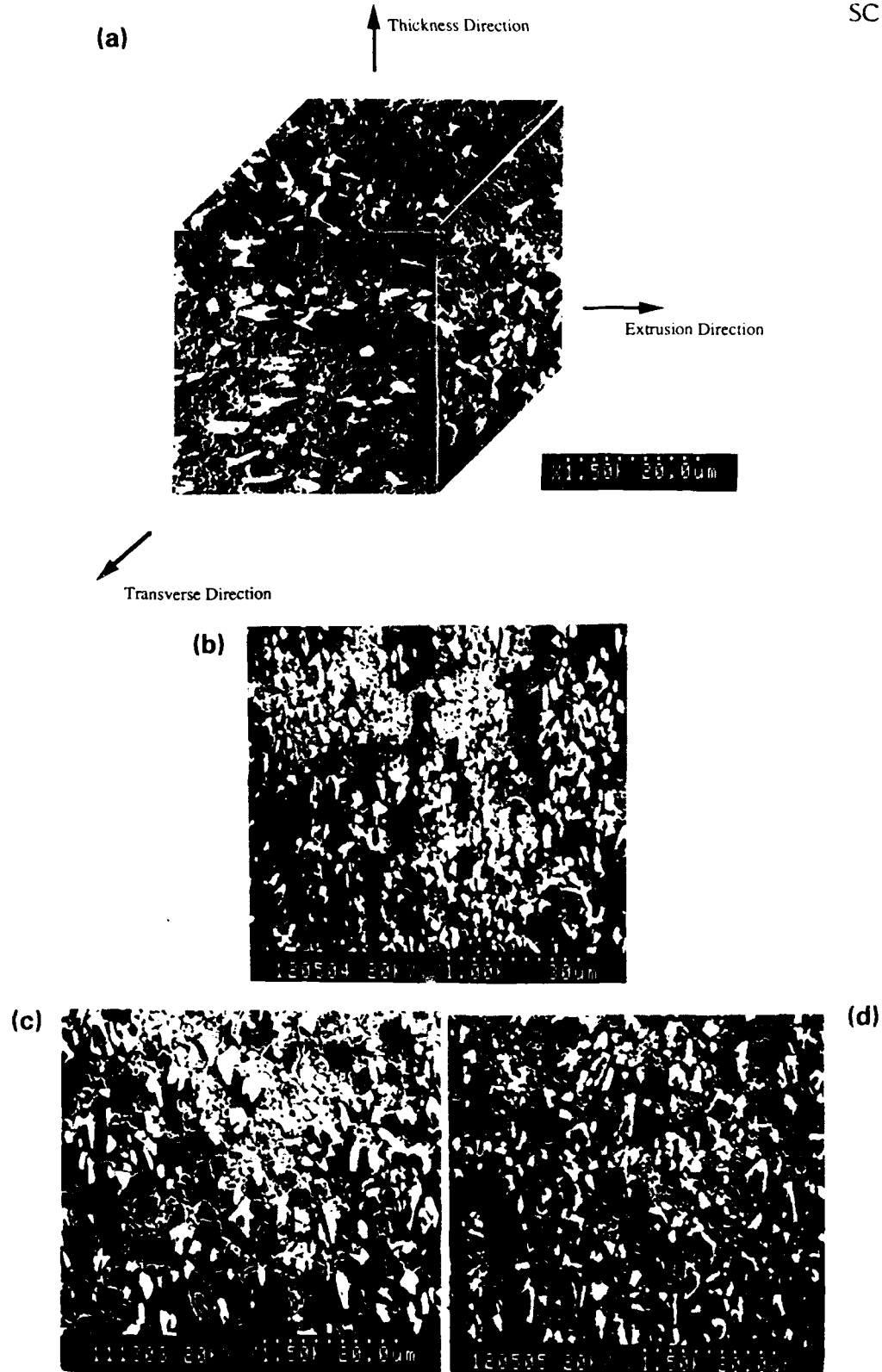


Fig. 15 SEM microstructures of 7064 Al/SiC: (a) as extruded; (b) 350°C warm rolled; (c) fine grain TMT; and (d) three-axis forged conditions. (Rolling direction is vertical.)



Fig. 16

Grain size (subgrain size) of 7064 Al/SiC for various processing methods.

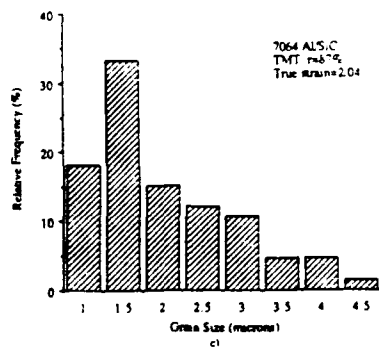
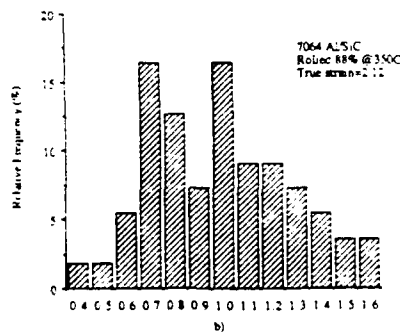
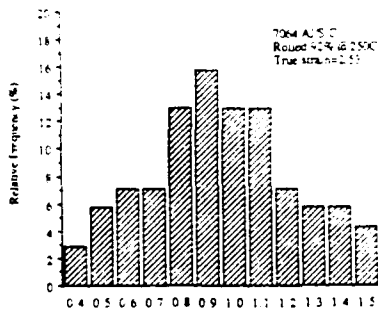
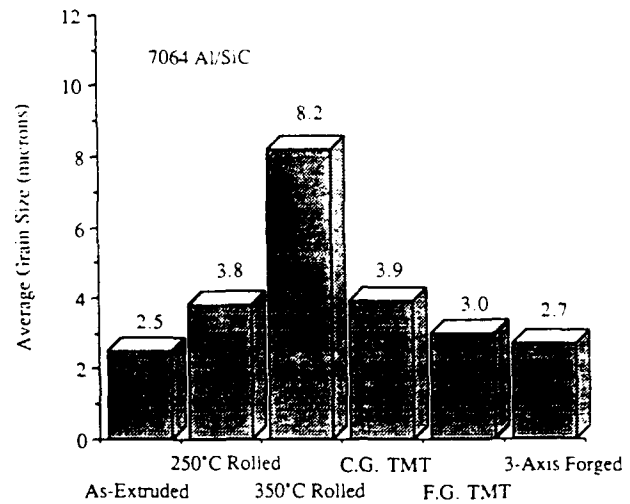


Fig. 17 Subgrain size distribution of 7064 Al/SiC: (a) 250°C rolled; (b) 350°C rolled; and (c) fine grain TMT.

recovery effects are substantial between 250°C and 350°C and SiC particles do not appear to influence this in any way.

A comparison of the microstructure from a coarse grain thermomechanically processed specimen and that from a fine grain TMT specimen indicates that the small reduction (46%) during the rolling step would result in grain coarsening (a grain size of 5.3 μm vs that of 2.6 μm) due to the insufficient rolling reduction compared to what would be required for recrystallization (91%).

Distributions of subgrain size for 250°C and 350°C rolled as well as thermomechanically processed 7064 Al/SiC shown in Fig. 17 are plotted as grain size against the relative frequency of each size interval. Results from the statistical analysis of the subgrain size data are summarized in Table 4.

Table 4
Statistical Analysis of Subgrain Size Data for Warm Rolled 7064 Al/SiC

Processing	Range of Subgrain Size (μm)	Mean (μm)	Sample Size	Sta. Dev.*
250°C rolled	0.33 - 1.49	0.90	70	0.273
350°C rolled	0.34 - 1.56	0.94	50	0.291
F.G. TMT	0.48 - 4.12	1.78	66	0.854

* Sta. Dev. stands for standard deviation of samples.

For both rolling conditions, the size distribution displays a similar pattern, with more than 50% of the grains having a mid-range size (0.7-1.1 μm). Results from the statistical analysis indicate that the average subgrain size and the standard deviation of the sample are very close for the sampled rolled at 250°C and 350°C, respectively (Table 5). It appears that there is little effect of the rolling temperatures on subgrain size of the material.

The subgrain size increased substantially for the TMT (Fig. 17(c)) with over 50% grains being 0.5-2.0 μm in size. This increase in size is believed to be associated with the formation of high angle grain boundaries, as discussed in the next section.

Grain Size (As-Tested) - Grain size of the specimens after tensile testing was determined both in the gauge area and in the grip area, Fig. 18 and Table 5. The average

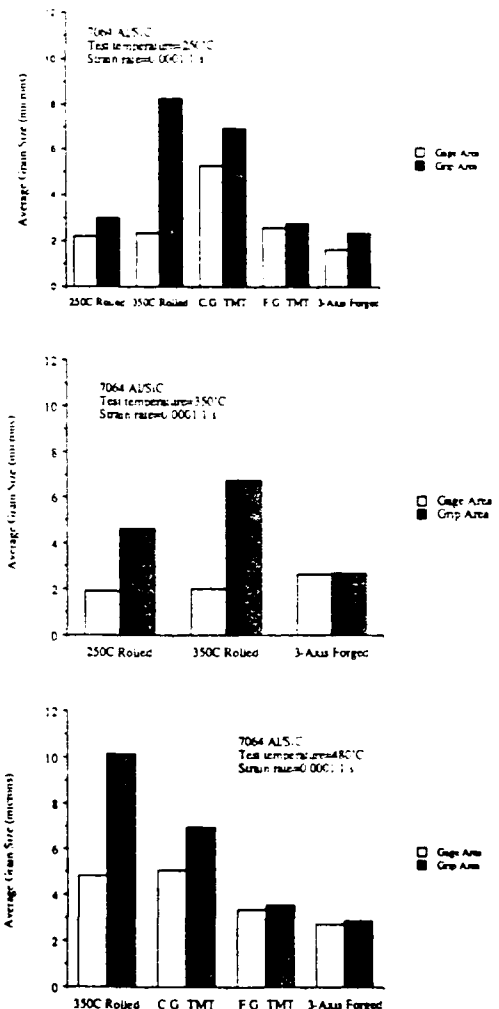


Fig. 18

Grain size of 7064 Al/SiC after tensile test at elevated temperatures.



Table 5
Grain size in 7064 Al/SiC after Tensile Test

<u>Processing Condition</u>	<u>Test Parameters</u>		<u>Average Grain Size (μm)</u>	
	<u>T ($^{\circ}\text{C}$)</u>	<u>$\dot{\epsilon}$ (S^{-1})</u>	<u>Grip Area</u>	<u>Near Fracture Region</u>
250 $^{\circ}\text{C}$ Rolled	250	10^{-4}	3.0 ± 0.5	2.2 ± 0.3
	350	10^{-4}	4.6 ± 1.2	2.1 ± 1.2
350 $^{\circ}\text{C}$ Rolled	250	10^{-4}	8.2 ± 2.9	2.4 ± 0.3
	350	10^{-4}	6.8 ± 1.5	2.0 ± 0.7
	480	10^{-4}	10.1 ± 2.3	4.8 ± 0.9
	350	10^{-2}	9.6 ± 1.3	2.0 ± 0.3
C.G. TMT	250	10^{-4}	6.9 ± 3.0	5.3 ± 0.6
	480	10^{-4}	6.9 ± 0.5	5.1 ± 0.4
F.G. TMT	250	10^{-4}	2.6 ± 0.3	2.8 ± 0.3
	480	10^{-4}	3.4 ± 0.4	3.7 ± 0.8
3-Axis Forged	250	10^{-4}	2.4 ± 0.4	1.6 ± 0.3
	350	10^{-4}	2.7 ± 0.5	2.6 ± 0.6
	480	10^{-4}	2.9 ± 0.1	2.7 ± 1.0

grain size represents the grain size in various directions along which the measurement was made. The standard deviation indicates the uniformity of the grain structure.

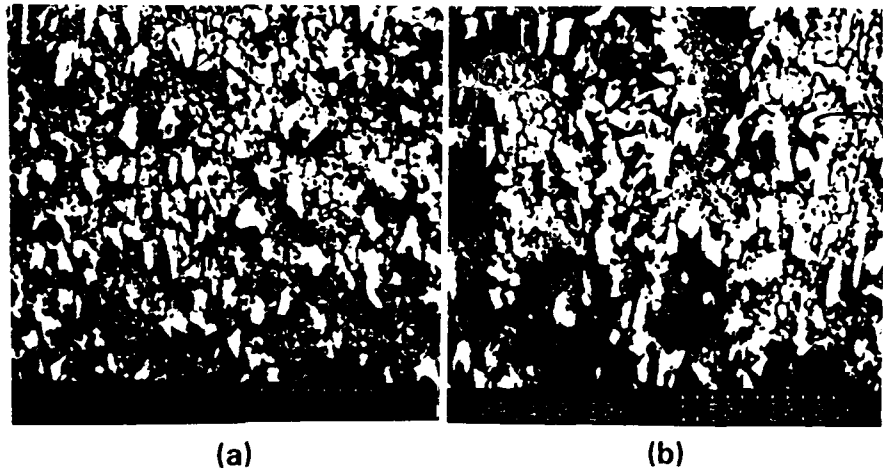
Compared with the grain size of the as-processed materials (Table 4), data in Table 5 indicate that grains were refined in all the rolled specimens during the tensile tests at all test temperatures, as a result of dynamic recrystallization, but those in the grip area remained largely unchanged. Figure 19 shows such an example of the 350 $^{\circ}\text{C}$ rolled specimen tested at 350 $^{\circ}\text{C}$ and 0.0001 1/s. The grains in the gauge area were refined during testing, while those in the grip area did not change their size significantly.

At 480 $^{\circ}\text{C}$ test temperature, the 350 $^{\circ}\text{C}$ rolled specimen showed the greatest microstructural instability, with grain growth to 10.1 μm in the grip region. However, with concurrent deformation, the same material showed significant refinement (4.8 μm) from a starting grain size of 8.2 μm . It appears that SiC particulates can strongly influence dynamic grain refinement process by nucleating new grains, but provide little barriers to boundary migration under static annealing conditions. Of course, this situation is also affected by the initial microstructural state of the material. For example, when a



Fig. 19

SEM microstructures of 350°C rolled 7064 Al/SiC after tested at 350°C and 0.0001 1/s: (a) gauge area, and (b) grip area. (Tensile axis is vertical.)

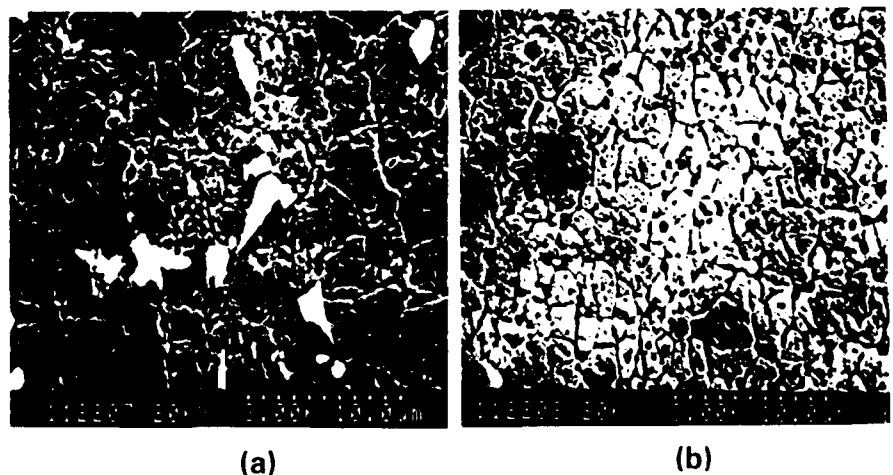


stabilizing treatment (480°C/5 mins) was given to the fine grain TMT and three-axis specimens prior to tensile testing, the grains underwent virtually no size change. The fine grain TMT specimen tested at 480°C had a slight grain growth after the test, suggesting that this was approaching a steady state structure for that test condition. The stability of these structures is related to the nature and misorientation of grain boundaries which are affected by the processing method.

Figure 20 presents the typical microstructure of the compression test specimens. The grain size was determined by averaging the grain size in the compressive loading direction and the transverse direction. Variation of the average grain size as a function of total strain is given in Fig. 21. The average grain size decreased for both strain rates for samples tested at 250°C and 350°C. Grain coarsening took place when tested at 480°C. This is consistent with the observation from the tensile tests discussed above.

Fig. 20

Typical grain structures of 7064 Al/SiC after compression test at 350°C and 0.0001 1/s: (a) plane parallel to compression (vertical) axis, and (b) plane normal to compression axis.



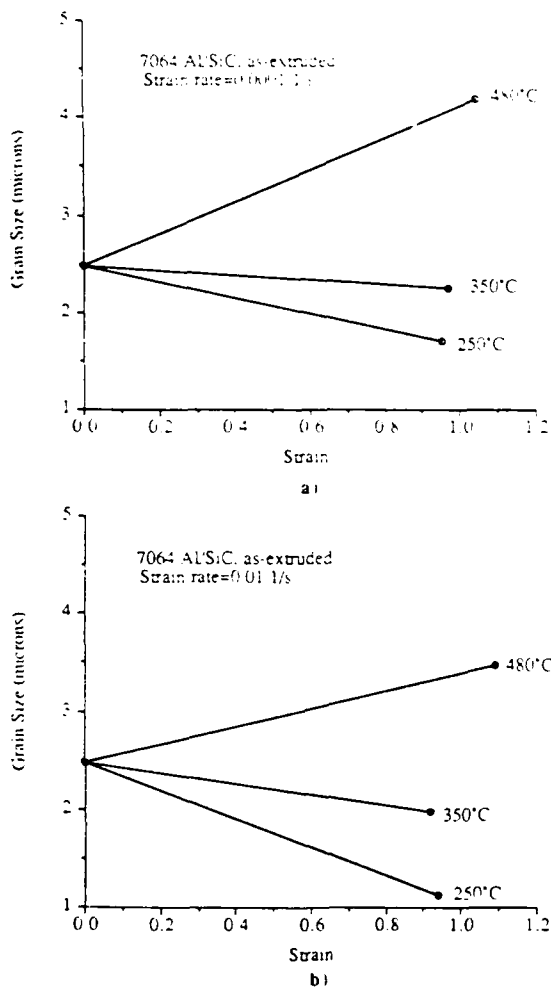


Fig. 21

Variation of average grain size of 7064 Al/SiC tested in compression at various temperatures and strain rates of (a) 0.0001 1/s and (b) 0.01 1/s as a function of strain.

Misorientation - Subgrain misorientation data of warm rolled and thermomechanically treated samples are presented in Fig. 22(a) to 22(c), and those obtained from the as-extruded and the three-axis forged samples, which were reported earlier,²⁴ are reproduced in Figs. 22(d) and 22(e) for the convenience of comparison.

The 18:1 extrusion ratio is capable of generating sufficiently large shear deformation to produce about as many (> 40%) grain boundaries with high misorientation (> 25°), as those with misorientations less than 15°. The 250°C rolling produced a predominantly large number of subgrains which were low-angle boundary (< 5°) grains, and the 350°C rolling resulted in > 55% of subgrains whose boundary angles were less than 5°. The number of low-angle (< 5°) boundaries formed as a result of rolling is about 3-3.5 times that for the as-extruded material. This observation may indicate that dynamic recovery has taken place during the rolling process at both temperatures. This dynamic change in microstructure is usually associated with the annihilation of pairs of dislocations during deformation due to the ease of cross slip, climb, and dislocation unpinning at nodes in this temperature region. Figure 23 shows the relationship between the average grain misorientation and its relative frequency. Notice the dramatic decrease in the number of grains as the misorientation angle increases for the samples rolled at 250°C and 350°C.

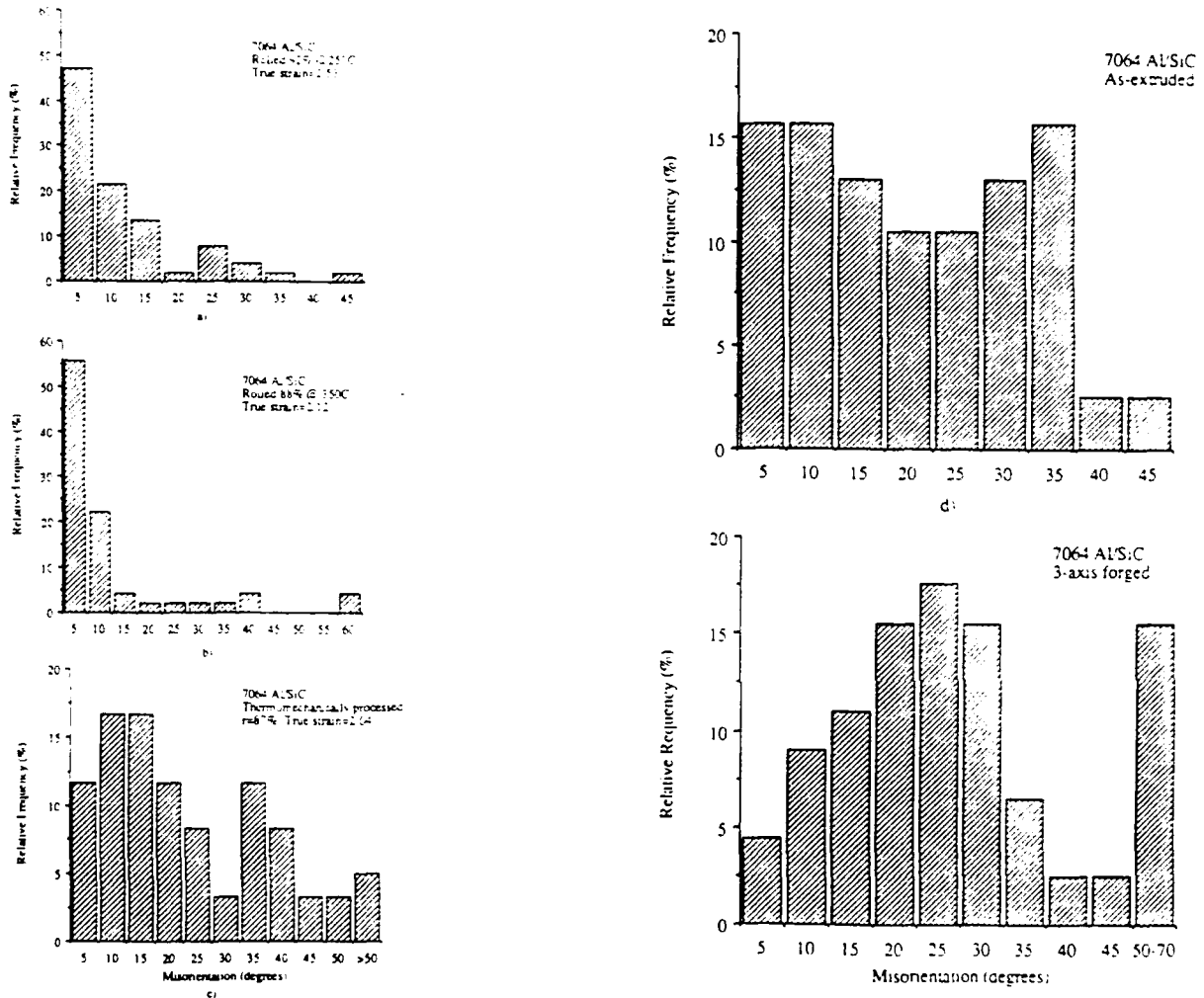


Fig. 22 7064 Al matrix subgrain misorientation distribution: (a) 250°C rolled; (b) 350°C rolled; (c) fine grain TMT; (d) as-extruded and (e) three-axis forged condition.

After the thermomechanical treatment, the number of high-angle grain boundaries increased significantly and that of low-angle boundary ($< 15^\circ$) grains fell to less than 45%. The formation of high-angle boundary grains is attributed to the recrystallization process following the 250°C cross rolling step during which the grains were heavily deformed. In the case of three-axis forging, the low-angle grain boundaries were reduced to less than one-quarter of the total grains examined and a much larger fraction of high-angle boundaries was generated. This is probably the primary reason for stability of this structure.

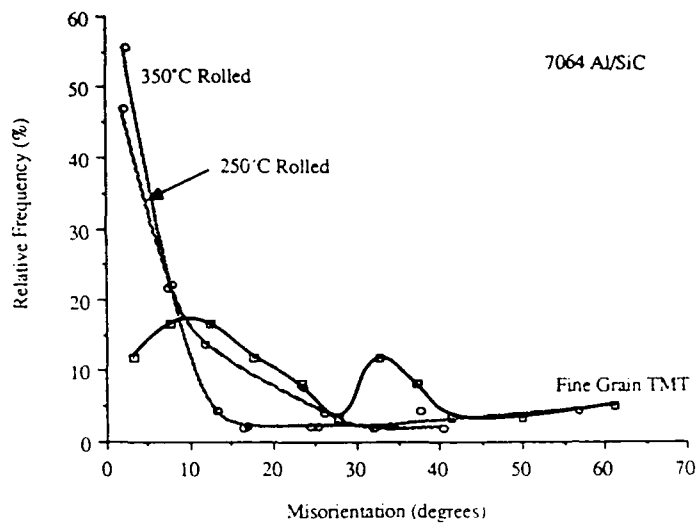
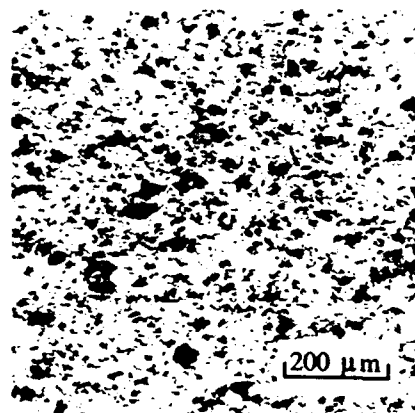
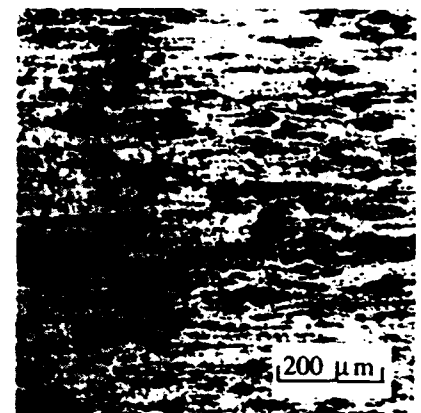


Fig. 23

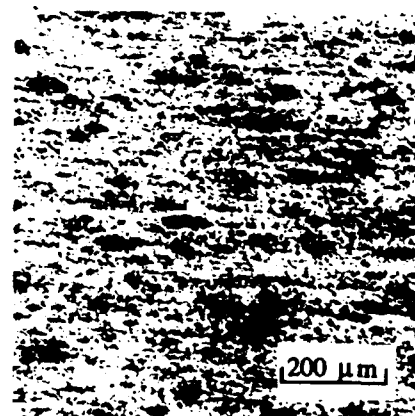
Relative frequency of average grain misorientation of 7064 Al/SiC.



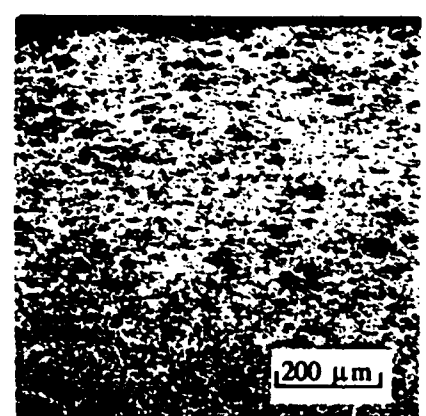
(a)



(b)



(c)



(d)

Fig. 24

Optical microstructure of 350°C rolled 7064 Al/SiC, (a) as-extruded, (b) rolled 23% at 350°C, (c) rolled 52% at 350°C, and (d) rolled 88% at 350°C.



Deformation of SiC Particulate Clusters - The distribution of SiC particulates in the as-extruded 7064 Al/SiC is not uniform throughout the microstructure, as seen in Fig. 24(a). After a 25% rolling reduction at 350°C, these SiC clusters were elongated in the rolling direction Fig. 24(b)). As the amount of deformation increased, the number of SiC clusters reduced, and many of them were broken up into smaller clusters or even individual particulates, Fig. 24(c). A similar trend was also observed in the samples rolled at 250°C, Fig. 25. Although at this lower rolling temperature, the process was delayed until the rolling reduction reached approximately 53%.

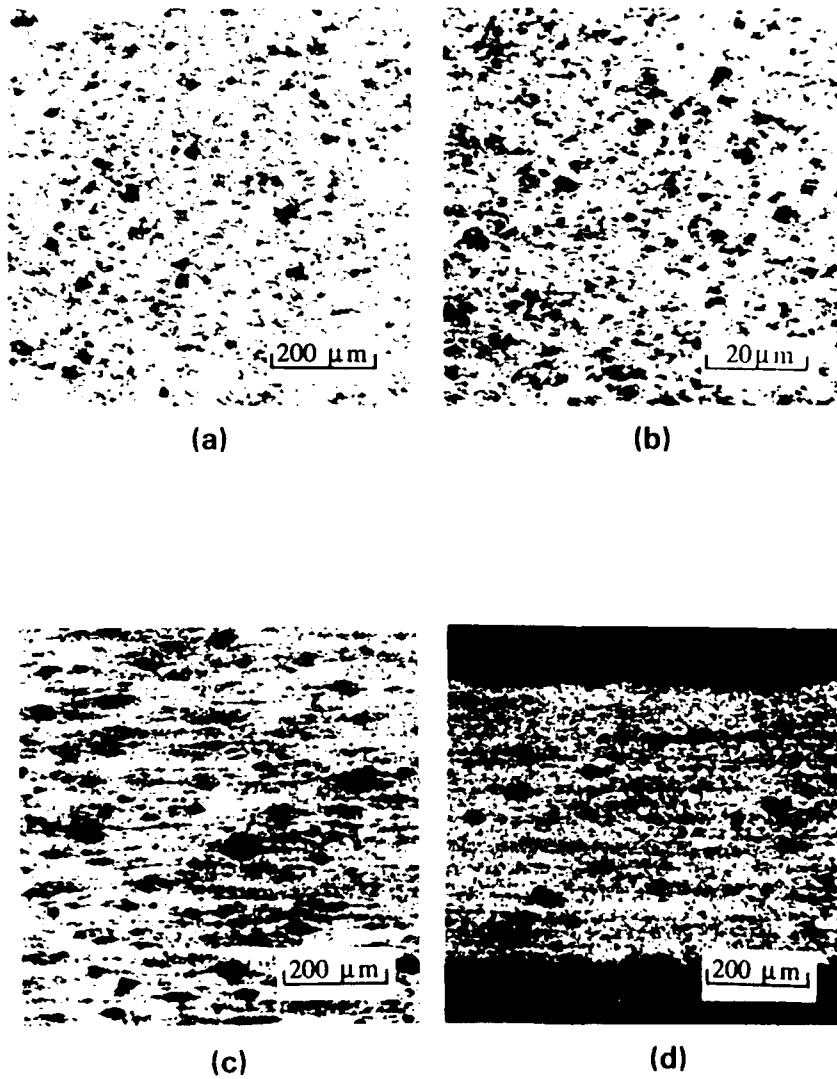


Fig. 25

Optical micro-structure of 250°C rolled 7064 Al/SiC, (a) as-extruded, (b) rolled 25% at 250°C, (c) rolled 53% at 250°C, and (d) rolled 92% at 250°C.



Changes in distributions of SiC particulate clusters were quantified by three parameters defined in Section 3.2.4.4.1. Figures 26 to 28 summarize the results. These parameters are presented with respect to the effective strain and rolling reduction of the samples. The area fraction of SiC particulate clusters decreases continuously as the effective strain increases for both rolling conditions (Fig. 26). On the other hand, the area

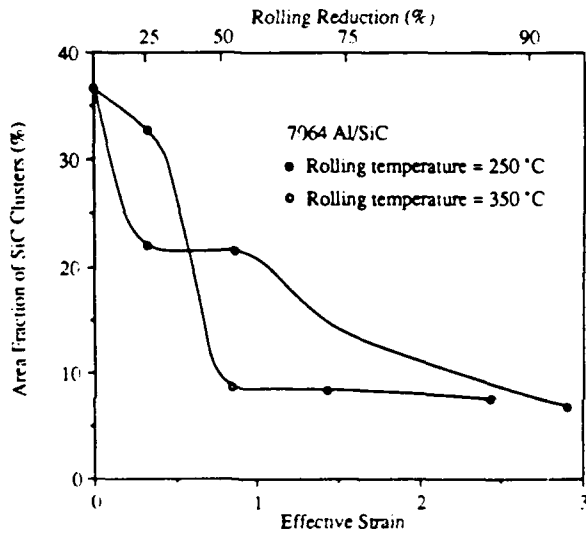


Fig. 26 Area fraction of SiC clusters as a function of effective strain.

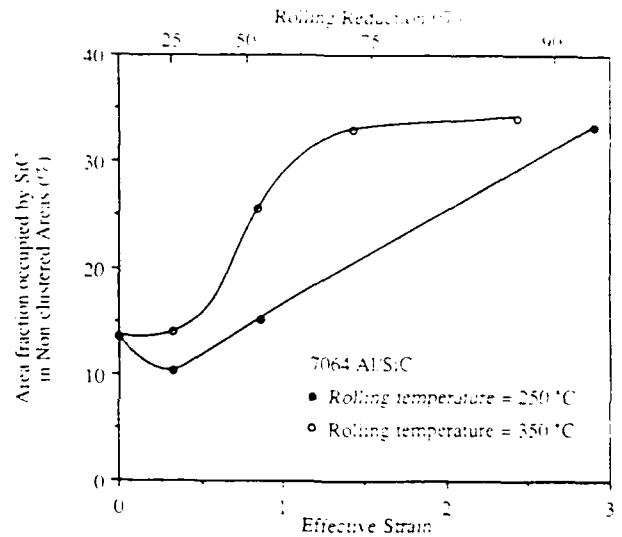
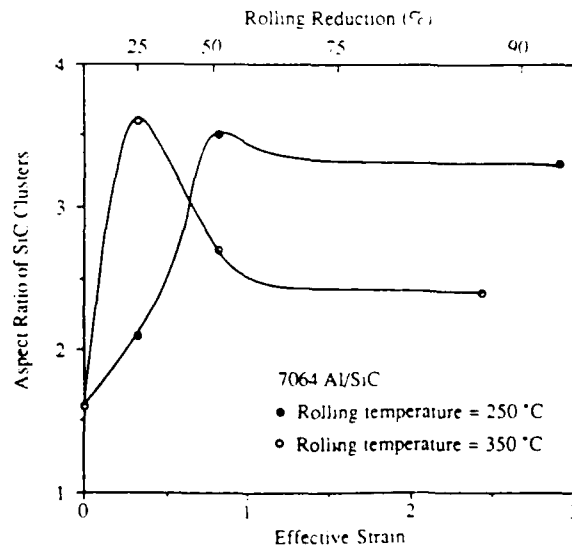


Fig. 27 Aspect ratio of SiC particulate clusters as a function of effective strain.

Fig. 28 Aspect ratio of SiC particulate clusters as a function of effective strain.





fraction occupied by SiC particulates in the nonclustered areas generally increases as the effective strain increases despite different rolling temperatures. At the rolling temperature of 350°C, the aspect ratio of SiC clusters increases sharply at the early stage of deformation and reaches its peak at about 25% reduction. Then there is a decline at the higher strain levels as a result of breaking up of SiC clusters. At 250°C, however, the peak shifts to higher strains, and the decline of the ratio after the peak becomes much less.

The movement of the SiC particulates depends upon the flow behavior of the matrix as well as deformation conditions. Under shear stresses, the particulates at the outer layers of clusters flow with the matrix much easier than those at the core. This appears to be the process of turbulent shear flow. As a result of this, these particulates were moved away from the clusters and become tails of clusters, as seen in Fig. 24(b) and 25(c). As the level of strains gets higher, more SiC particles are removed from the clusters to the areas originally SiC particulate-free. This process is clearly shear strain dominated. At lower rolling temperatures, plastic flow of the matrix and the SiC particulates becomes more difficult, requiring higher stresses to break them up. This explains why the peak of the aspect ratio shifts to higher strains, and this ratio maintains at a relatively high level afterwards. Also because of their low mobility, the area fraction occupied by the SiC particulates in nonclustered areas is lower at 250°C than that at 350°C.

3.2.4.5.1.2 Flow Behavior of 7064 Al/SiC

Warm Rolled Material - A summary of tensile results of 250°C and 350°C rolled specimens which were subsequently tested at various temperatures is presented in Table 6.

Table 6
Summary of Tensile Test Results of Warm Rolled 7064 Al/SiC

Material	Test Parameters		Stress at Max.		
	T (°C)	$\dot{\epsilon}$ (S ⁻¹)	Load (MPa)	% Elongation	ϵ_f
250°C rolled	250	10 ⁻⁴	86.4	58.1	0.50
	350	10 ⁻⁴	27.4	72.5	0.83
350°C rolled	250	10 ⁻⁴	88.4	50.1	0.54
	350	10 ⁻⁴	26.0	62.9	0.82
	480	10 ⁻⁴	20.4	21.6	0.20
	350	10 ⁻²	55.1	98.2	1.00



From Table 6, it can be seen that flow stress and ductility of the two materials were affected significantly by test temperature and strain rate. As expected, at the lower test temperatures, the materials showed increased flow stress but lower ductility. The flow stress and the rate of strain hardening are considerably greater for test temperature of 250°C in comparison to 350°C. The strain to maximum load is higher at 250°C, however, the total elongation is greater at 350°C. This is due to greater dynamic recovery at 350°C.

The 350°C rolled material is most ductile when tested at 350°C compared to testing at 250°C and 480°C. A higher flow stress was observed at 480°C than at 350°C resulting from the coarser microstructure produced by the heating to 480°C (see Table 5). Dynamic recovery seemed to be nonexistent with this material and intergranular fracture occurred with low strain to fracture. Thus, the best processing window for sheets rolled at 250°C and 350°C is deformation carried out at 350°C.

Effect of strain rate on flow stress of the 350°C rolled specimen was also measured. At the high strain rate, the material showed a rapid increase in stresses before reaching the steady state. A 100-fold increase in strain rate doubled the flow stress and increased the total elongation by over 55%, Table 7. A calculation of strain rate sensitivity indicated an m value of 0.25 at the strain level of 0.075. This suggests that deformation is by dislocation creep although the level of flow stress and possibly m value can be affected significantly by the process of matrix sliding past SiC particles. The increased elongation at the high strain rate is believed to be related to dynamic recrystallization.

Thermomechanical Treatment - Tensile data in Table 7 show that, after the starting grain size was reduced from 3.9 μm to 3.0 μm (see Table 4), the total elongation of the fine grain TMT material tested at 250°C and 480°C was improved 4-5 times in comparison to the coarse grain TMT material. Fracture strain was also improved by 234% and 154%, respectively. While the elongation showed a similar response to test temperatures for both materials, the fracture strain seemed to be relatively insensitive to the temperature change.

Strain hardening of the fine grain TMT material was gradual and essentially linear with strain at 480°C. This indicates a grain growth induced hardening, especially at the test temperature of 480°C, where the grains were found to be coarsened in the gauge area after the test. Strain hardening for the coarse grain TMT material was rapid and led to an early fracture. It is clear that the steady state stress in these materials is strongly influenced by the starting microstructure of the material, unlike that in materials undergoing dynamic recovery.



Table 7
Summary of Tensile Test Results of TMT 7064 Al/SiC

<u>Material</u>	<u>Test Parameters</u>		<u>Stress at Max.</u>		
	<u>T (°C)</u>	<u>$\dot{\epsilon}$ (S⁻¹)</u>	<u>Load (MPa)</u>	<u>% Elongation</u>	<u>ϵ_f</u>
C.G. TMT	250	10 ⁻⁴	179.6	12.2	0.21
	480	10 ⁻⁴	11.8	29.5	0.28
F.G. TMT	250	10 ⁻⁴	120.9	73.5	0.68
	480	10 ⁻⁴	3.9	144.0	0.71

Table 8
Summary of Tensile Results of Three-Axis Forged 7064 Al/SiC

<u>Material</u>	<u>Test Parameters</u>		<u>Stress at Max.</u>		
	<u>T (°C)</u>	<u>$\dot{\epsilon}$ (S⁻¹)</u>	<u>Load (MPa)</u>	<u>% Elongation</u>	<u>ϵ_f</u>
3-axis forged	250	10 ⁻⁴	99.1	43.3	0.88
	350	10 ⁻⁴	30.1	52.3	1.04
	480	10 ⁻⁴	3.7	172.4	2.03

Three-Axis Forging - The three-axis forged specimens were tested at 250, 350 and 480°C, with a strain rate of 0.0001 S⁻¹. The test data are summarized in Table 8. The total elongation increased about 400% and the fracture strain more than 230% as the temperature increased from 250°C to 480°C.

The improved ductility was concurrent with lower flow stresses. Similar to the fine grain TMT material, the three-axis forged material also exhibited linear work hardening behavior with the strain.

Compression Tests - Constant strain rate compression tests were performed on the as-extruded 7064 Al/SiC at 250, 350 and 480°C. Two strain rates were used, 0.0001 S⁻¹ and 0.01 S⁻¹.

The steady state flow stress is affected by test temperatures and strain rate. At the slower strain rate, the maximum stress decreased from 120 MPa to 10 MPa as the temperature decreased from 250°C to 480°C. On the other hand, at the higher strain rate



but within the same temperature range, the maximum stress decreased from 200 MPa to 22.5 MPa. The increase in flow stress as a result of the change of strain rate depends on temperature. For example, at 250°C, the maximum stress increased by 67% as the strain rate increased from 0.0001 S^{-1} to 0.01^{-1} . However, at 480°C, the same change in strain rate resulted in a 125% increase in stress.

Strain rate sensitivity of the as-extruded material was calculated at the strain level of 0.1 and 0.2 for three test temperatures. The result is presented in Table 9. The m value varied from 0.117 to 0.134, increasing with the test temperature.

Table 9
Strain Rate Sensitivity of As-Extruded 7064 Al/SiC

<u>Test Temperature (°C)</u>	<u>Strain Rate Sensitivity</u>
250	0.117
350	0.121
480	0.134

Effect of Mechanical Processing on Flow Behavior of 7064 Al/SiC - Flow behaviors of 7064 Al/SiC processed via rolling, three-axis forging, and TMT, tested at 250, 350 and 480°C, have been compared with that of the as-extruded material obtained from the compression tests. At 250°C, coarse grain TMT material has a low initial flow with a strain hardening rate that becomes increasingly higher resulting in the highest yield strength. The fine grain TMT shows a behavior similar to the coarse grain TMT material, but dynamic recovery effects lead to much lower stresses for $\epsilon = 0.01$ or greater. The three-axis forged material shows an initial yield behavior which is similar to the two cases mentioned above, however, with considerably less strain hardening. Contrary to expectations, the 350°C rolled material shows a higher initial flow stress than the sample rolled at 250°C. The most probable reason for this is the internal residual stresses which may develop around SiC particles during deformation and which experience more recovery during 350°C rolling.

The warm rolled materials behave in an entirely different manner from the three-axis forged and thermomechanically processes materials, and lead to steady state stresses which are quite dependent on initial structure of the material.



At all temperatures, the flow stresses relative to the extruded material were reduced significantly by any of the processing methods. The higher flow stress of the as-extruded material despite its fine microstructural size may lie in the predominance of low angle grain boundaries and harder unworked prior particle boundaries in that material. It is also possible that the extruded material possesses some amount of "cold work" which is not fully recovered. The flow curves for 250 and 350°C rolled samples tested at 350°C are considerably closer than those tested at 250°C, which suggests that recovery effects at 350°C remove any internal residual stresses which might remain in the sample rolled at 250°C.

Virtually no difference in flow behavior is observed between the three-axis forged and fine grain TMT materials at 480°C but the former is considerably softer at 250°C. The 480°C behavior is marked by grain growth hardening which is identical for the two processing conditions, although the maximum ductility is greater for the three-axis forged material.

Dynamic Strain Aging - Dynamic strain aging was observed in all warm rolled and coarse grain TMT specimens, but was not observed in the fine grain TMT and the three-axis forged materials. The dynamic strain aging was associated with irregular and sudden drops in load during testing, and was marked by the occurrence of serrations in the load-displacement curves. Dynamic strain aging is usually associated with the interreaction between dislocations and solute atoms, and sometimes related to the rate of work hardening. However, in our case, the serrations occurred primarily in the coarse grain structures which show the higher initial work hardening rate. It is possible that these serrations are triggered by a higher rate of work hardening for these processing conditions which also maintained a high solute concentration level.

Effect of Grain Size on Fracture Strain - It appears that the fracture strain of these materials is closely related to the matrix grain size, particularly at the higher test temperatures. Figure 29 is a plot of fracture strain vs grain size measured near the fracture surface and in the grip area for a variety of test temperatures. In general, as the grain size near the fracture surface increased, the fracture strain decreased, regardless of the processing conditions and test temperatures.

Effect of Test Temperature - Grain size measurements and tensile test data (Tables 5-8) clearly indicate that higher test temperatures result in flow stress and strain hardening decreases in all materials. Since the ability to retain grain size at these temperatures diminished for warm rolled and coarse grain TMT specimens, elongation



Fig. 29

Fracture strain vs grain size of 7064 Al/SiC (a) near the fracture surface (top), and (b) in the grip area (bottom).

decreased accordingly. However, with the fine grain TMT and the three-axis forged microstructures, the grain size increased only slightly, so that the materials maintained a relatively higher elongation. Below 480°C, grain size is stable in all the processed materials except for the coarse grain TMT material.

Cavity Distribution - Cavities were observed in specimens tested at all three temperatures. Figure 30 shows the typical form of cavities near the fracture surface. Cavitation was found both at the tip of a SiC cluster, where the stress concentration was high because of the inhomogeneous deformation (Fig. 31), and at grain boundaries, where the particles debonded with the matrix (Fig. 32). Figure 33 illustrates the distribution of cavities as a function of strain in the three-axis forged material tested at 480°C. The amount of cavities increased rapidly as the level of strain increased. It is believed that the cavity formation is closely associated with the triaxial stress state developed in the matrix between particles. Cavities that form along grain boundaries are enlarged in the direction of tensile stress.

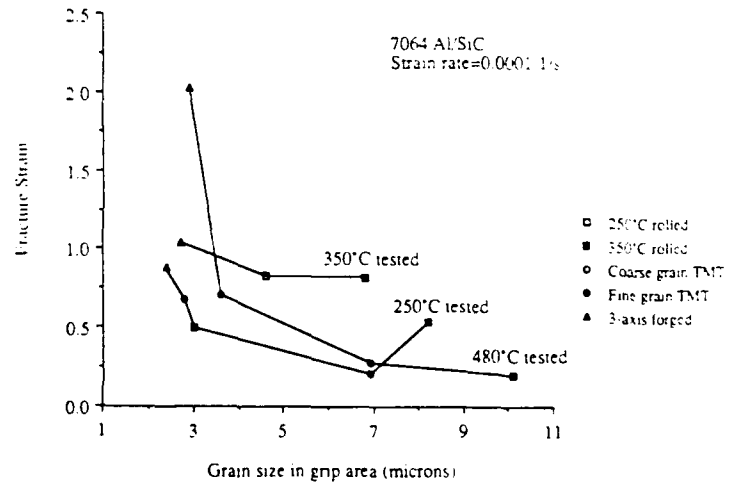
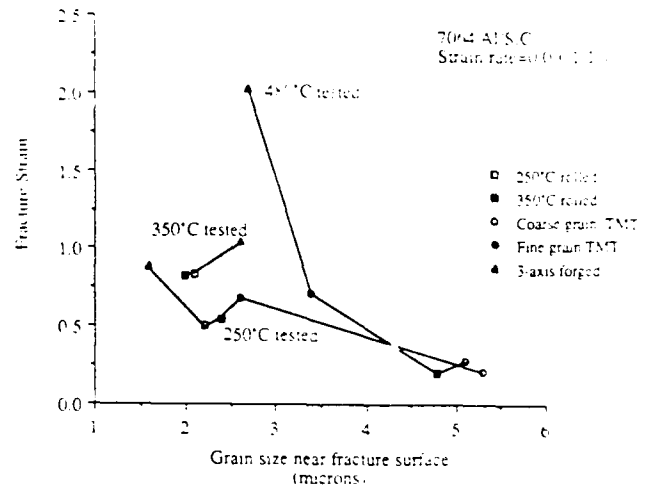




Fig. 30 Cavitation below the fracture surface of the 350°C rolled 7064 Al/SiC tested at 350°C and 0.01 1/s.

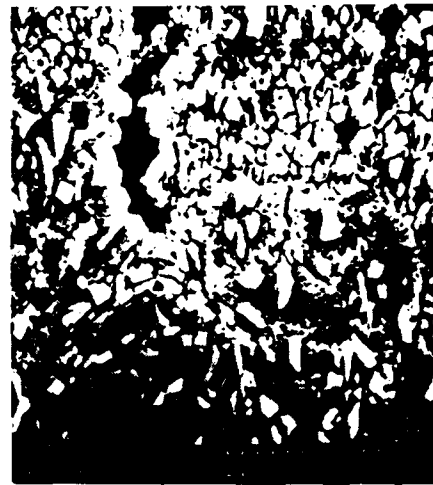


Fig. 31 Cavitation initiated at the tip of SiC cluster.



Fig. 32 Cavity formation along grain boundaries.

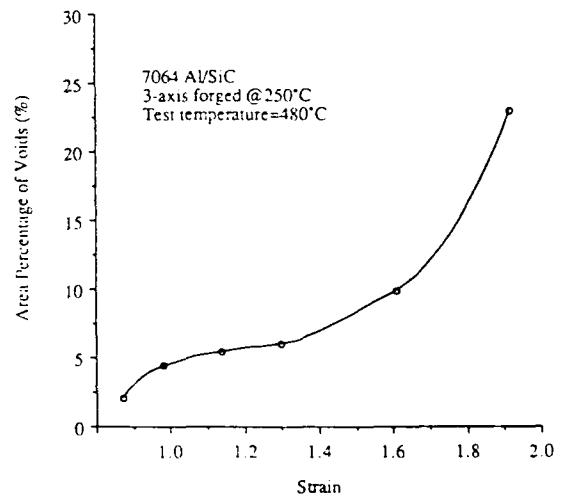


Fig. 33 Cavitation as a function of strain, determined by metallographic method.



3.2.4.5.2 Al-8Fe-4Ce (C478)

3.2.4.5.2.1 Microstructure

Microstructures of the warm rolled, and the three-axis forged and subsequently rolled Al-8Fe-4Ce alloy show very fine precipitates located at grain and subgrain boundaries (Fig. 34). Detailed structure of the fine dispersoids, $\leq 1 \mu\text{m}$, is illustrated in Fig. 35. It was reported^{1,39,40} that these dispersoids are $\text{Al}_{13}\text{Fe}_4$ and $\text{Al}_{10}\text{Fe}_2\text{Ce}$.

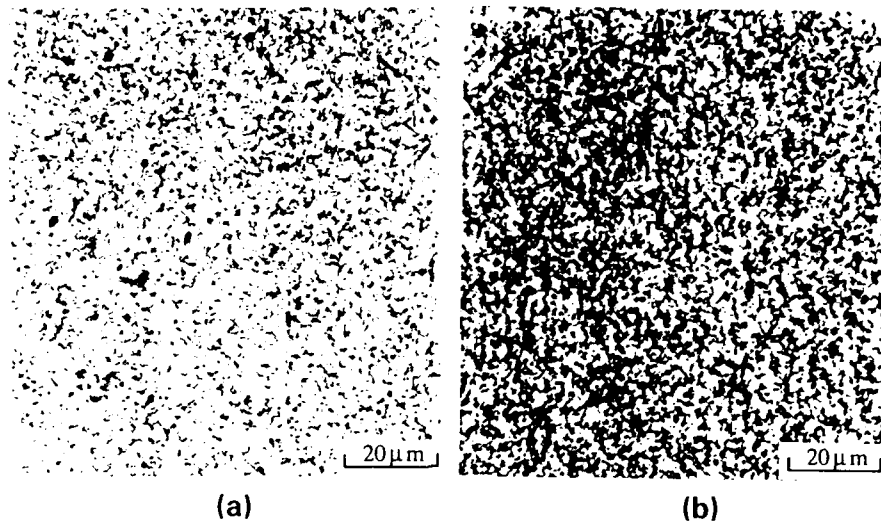


Fig. 34 Optical microstructure of (a) 380°C rolled and (b) three-axis forged Al-8-Fe-4Ce.

Fig. 35

SEM microstructure of 380°C rolled sheet tested at 480°C and 0.005 1/s.





The microstructural dimension reported here is an average grain and subgrain size as measured by the linear intercept method. The measured microstructure sizes for both the rolled and three-axis forged and rolled material are reported in Fig. 36. Though somewhat scattered, the structural dimension of both materials exhibited an increasing trend with strain. It appears that the 380°C rolled microstructure is somewhat coarser than that of the three-axis forged and rolled specimen.

The morphology of the microstructure was affected by strain rates for a given temperature as shown in Fig. 37. At the high strain rate (0.1 S^{-1}), the microstructure has a banded appearance the width of which is about $20 \mu\text{m}$. This kind of structure was not observed in the same material tested at the slow strain rate of 0.005 S^{-1} .

Fig. 36

Variation of microstructural size of Al-8Fe-4Ce as a function of strain.

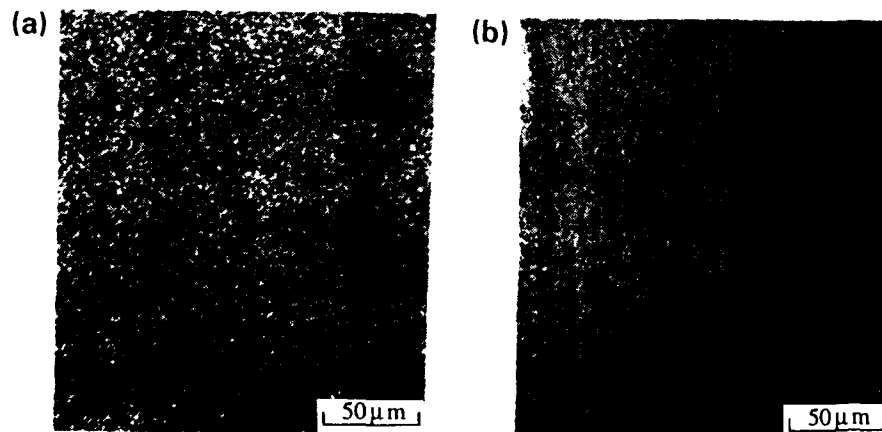
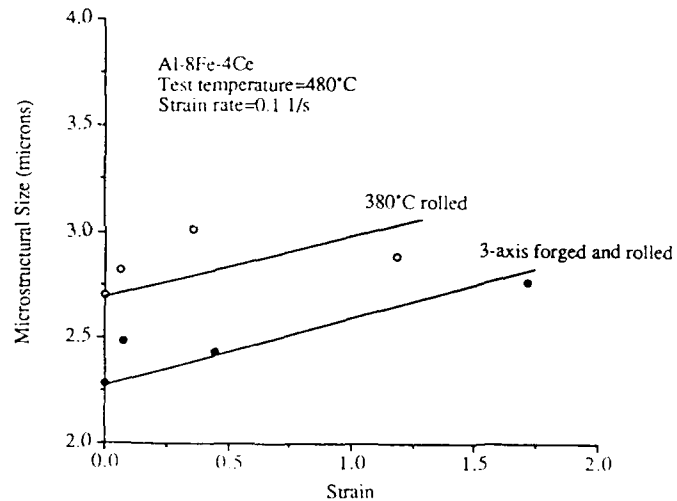


Fig. 37 Optical microstructure of rolled Al-8Fe-4Ce tested at (a) 0.005 1/s and (b) 0.1 1/s , 400X. Notice the non-uniform microstructure as a result of high strain in (b).



3.2.4.5.2.2 Mechanical Tests

To assess flow behavior of this material under various processing conditions, elevated temperature compression and tension tests were performed on the as-extruded material as well as on the rolled sheet and the three-axis forged and subsequently rolled materials.

Step-Strain Rate Tests in Compression - The results of three-step strain rate tests performed on as-extruded Al-8Fe-4Ce at 350, 480 and 520°C are shown in Fig. 38. Yield stresses obtained from tensile tests of the rolled sheet specimens for a given strain rate and test temperature are also plotted in the figure (shown as solid data points). Slopes of these curves ($\partial \log \sigma / \partial \log \dot{\epsilon}$), which represent the strain rate sensitivities of the material, are shown in Fig. 38(b) as a function of strain rate for these test temperatures. The strain rate sensitivity, m , remains nearly constant at 350°C for the entire range of strain rate under consideration, but increases as the test temperature increases. At 520°C, m increases from 0.06 to 0.2 as the strain rate increases from 5×10^{-4} to 5×10^{-2} .

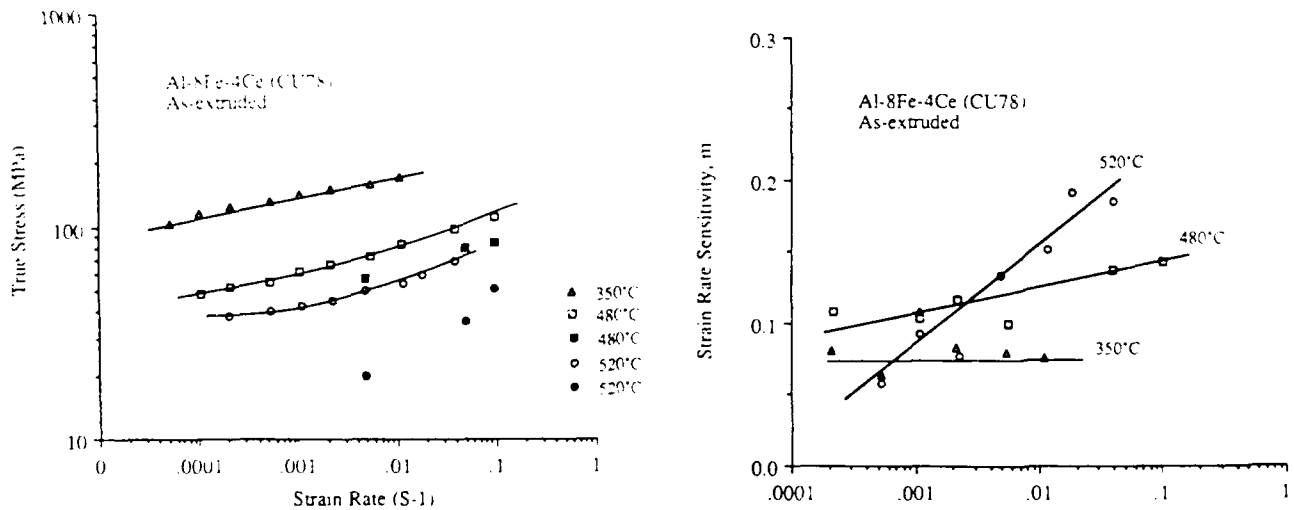


Fig. 38 (a) Flow stress vs strain rate of as-extruded Al-8Fe-4Ce. Open data points: compression data; solid data points: tensile data. (b) Strain rate sensitivity vs strain rate of as-extruded Al-8Fe-4Ce.

Figure 39 is an Arrhenius plot where the logarithm of the steady state strain rate is plotted against the reciprocal of temperature (K), for stresses ranging from 85 MPa to 115 MPa. The apparent activation energy for deformation of the as-extruded material, as calculated from the slope, was approximately 214 kJ/mol. This is higher than the activation



energy for bulk self-diffusion in aluminum (142 kJ/mol),²⁸ which is not surprising in view of the presence of higher melting constituents in solid solution and as precipitates. Similar results were reported by Legzdina and Parthasarthy⁴¹ who showed that the creep behavior of as-extruded Al-8.8Fe-3.7Ce alloy could be described by power law creep in the similar ranges of stress and temperature.

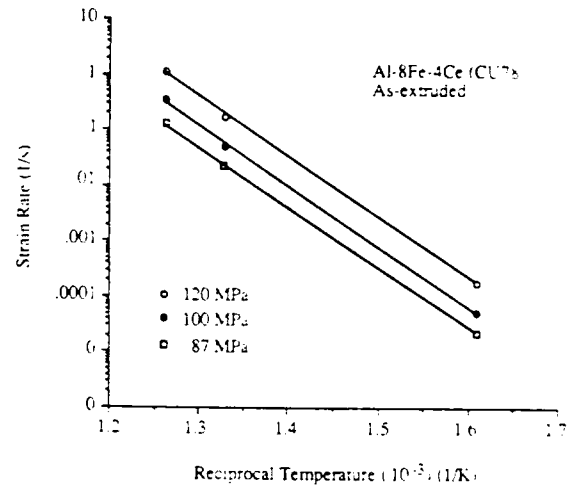


Fig. 39

Arrhenius plots showing the variation of strain rate with the reciprocal temperature of as-extruded Al-8Fe-4Ce.

Tensile Tests - High temperature tensile test data from warm rolled specimens and three-axis forged and sequentially warm rolled specimens are given in Table 10.

Table 10
Summary of Tensile Test Results of Al-8Fe-4Ce

Material	Test Parameters		Stress at Max.		
	T (°C)	$\dot{\epsilon}$ (S ⁻¹)	Load (MPa)	% Elongation	ϵ_f
380°C rolled	480	5x10 ⁻³	48.3	91.6	1.52
	480	5x10 ⁻²	70.5	83.0	1.36
	480	10 ⁻¹	76.8	75.2	1.38
	520	5x10 ⁻³	21.6	128.8	1.99
	520	5x10 ⁻²	38.6	115.3	1.73
	520	10 ⁻¹	46.4	88.9	1.79
350°C 3-axis forged and subsequently rolled	480	5x10 ⁻³	40.4	109.3	1.58
	480	10 ⁻¹	73.1	94.2	1.49
	520	5x10 ⁻³	25.3	135.6	2.01
	520	10 ⁻¹	46.6	115.2	1.97



Both of the processed materials exhibited more than 75% tensile elongation, compared with the tensile elongation of 55% of as-extruded material, as reported in Ref. 1. It is clear that the improvement in ductility comes from the additional mechanical processing which increases the average misorientation between subgrains, thereby enhancing diffusional creep, based on the model developed in this program.² For three-axis forged and subsequently rolled specimens, the total elongation was 20-30% higher than the rolled specimens. It is expected that the alloy would exhibit even higher ductility at temperatures greater than 520°C. Thus, superplastic behavior might be expected in this alloy. If tests are conducted with superimposed hydrostatic pressure to suppress cavitation, considerable large ductilities (300-400% elongation) may result.

Compression Tests - Flow curves of as-extruded Al-8Fe-4Ce alloy tested in compression at 480 and 520°C show a decreasing strain for the onset of significant plastic flow with increasing temperature. This is clearly a result of softening at the higher temperature, at which maximum flow stress was found to be 87 MPa as opposed to 120 MPa for a strain rate of 0.04 S^{-1} . This softening is expected from greater diffusional flow within the solid solution matrix and not related to the intermetallic particles. Flow softening is observed with increasing strain, possibly due to dynamic grain refinement and slight particle coarsening.

3.2.4.6 Conclusions

In this project, we have developed an understanding of the interrelationship among the various deformation (and thermomechanical) processing approaches, the resulting microstructures and their subsequent elevated temperature flow characteristics for two advanced aluminum-based materials. The materials are 7064 Al containing 15 v/o SiC particulate dispersions and Al-8Fe-4Ce alloy containing an extremely fine dispersion of complex intermetallic particles. Following extrusion, these materials were subjected to a variety of processing procedures involving a wide range of strain levels, and the subsequent flow behavior and microstructural characteristics were determined. The following major conclusions are made:

1. Three-axis forged and fine grain TMT processes produce the greatest microstructural refinement and larger grain misorientation distributions, in comparison to isothermally rolled materials. Extruded alloy showed an extremely fine microstructure but grain orientations are generally low.



These processing steps cause negligible microstructural coarsening in the Al-8Fe-4Ce alloy.

2. Processability improvements are greatest for the three-axis deformation, which shows largest ductilities and lowest flow stresses, believed to arise from extensive shear occurring on intersecting shear planes. Processability improvement is tied not only to microstructural fineness, but to the higher misorientation levels. Thus deformation path and the magnitude of overall strain influence subsequent flow characteristics more strongly than grain size or subgrain size.
3. Fracture strain increases with decreasing grain size at higher test temperatures (480°C) for 7064 Al/SiC, but the behavior becomes more complicated at lower temperatures (350°C or below). Overall ductility, however, increases and flow stress decreases with decreasing grain size even at the lower temperatures. This grain size dependence at temperatures well below that where diffusional creep is important suggests an important role of high angle grain boundaries on intermediate temperature creep.
4. In 7064 Al/SiC, SiC particle distribution becomes increasingly homogeneous during rolling. A mechanism of particle cluster break-up by shear flow at their extremities was deduced.
5. Dynamic grain refinement occurs during testing of the as-processed materials, even though the as-processed microstructure may be thermally unstable. Shear flow around particles is believed to be primarily responsible for this effect.
6. Al-8Fe-4Ce alloy exhibited extended ductility in three-axis forged condition, indicating it might be possible to achieve superplasticity in that alloy at higher test temperatures under superimposed hydrostatic pressure. Microstructural coarsening is negligible in this alloy at temperatures up to 520°C.



3.3 Part II. Creep of High-Temperature Intermetallics

This section describes results from Part II of the program to study creep behavior in Ti_3Al base alloys. The program goals are described, followed by a brief background outlining the basis of the program. Results reported earlier^(1,2) are summarized, followed by details of the latest results.

3.3.1 Program Goals

The overall objectives of Part II were to:

1. Measure the effect of C, O, Si, Fe, Nb, V, Zr, and Y on the 675°C creep resistance of Ti-23Al-8Nb (at. pct.).
2. Evaluate the influence of the most effective additives listed above on the creep behavior of Ti-24Al-11Nb (at. pct.).
3. Determine the mechanisms by which the minor alloying additions improve creep resistance in Ti_3Al base alloys.
4. Evaluate the contribution of primary creep strain to total creep strain.
5. Provide a phenomenological description of creep in Ti_3Al base alloys and the influence of additives thereon.

3.3.2 Background

Creep strength in Ti alloys is generally defined, for design considerations, as the ability to withstand deformation up to some specific level, such as 0.1 or 0.2%, for a given time, temperature and stress level. Testing that is performed to qualify alloys within these types of guidelines will therefore include both primary and secondary creep deformation. The large scatter in data from qualification tests has been attributed to the variations in primary creep strain.⁴² For instance, when Raut and Clough⁴³ could not get a good correlation of Ti creep-rupture data, they suggested it was due to "abundant scatter in the test results". Similarly, Bania⁴² has shown that primary creep strain in Ti-6Al-2Sn-4Zr-6Mo varies in a manner that does not correlate with heat treatment. Rhodes' work on alpha +



alpha two (alpha two = Ti_3Al) alloys has shown that alloys with identical secondary creep rates can have vastly different primary creep rates.⁴⁴ All of these results indicate that primary creep behavior in Ti alloys is not well understood.

The influence on creep behavior of minor additives to near-alpha and super-alpha Ti alloys has been documented over the last several years.⁴⁵⁻⁴⁷ However, their effects on Ti aluminide alloys have not been investigated. Because of the differences in deformation characteristics between the disordered alpha phase of the near-alpha alloys and the ordered alpha-two phase of the Ti aluminides, it is not clear if the effects of these minor additives will be similar in the the two types of alloy systems. This program examines those effects.

The overall goal of this research was to improve the creep resistance of high-temperature Ti alloys. The specific objectives were to: 1) investigate the influence of C, O, Si, Fe, V, Nb, Zr and Y on creep resistance of Ti-22Al-8Nb (at%); 2) evaluate the contribution of primary creep to total creep strain; and 3) determine the mechanism by which the additives improve creep resistance. The effort in Part II is divided into two phases which were performed sequentially. Phase I consisted of a screening approach to evaluate the effects of eight different additives that have been shown to have a significant effect on properties of leaner Ti alloys. Tensile and creep tests at 675°C provided sufficient information to determine which of the additives have the most significant effect on the creep resistance of the Ti aluminide base composition.

Phase 2 consisted of a study of the effects of minor alloying additives on creep resistance in Ti-24Al-11Nb. In addition, the contribution of primary creep strain to total creep strain was assessed.

3.3.3 Summary of Phase I Results

It was reported in Annual Report No. 1 that creep tests at 675°C and 30 ksi revealed small variations in steady-state creep rates with small composition variations.¹ It was shown that creep rates could be reduced by reducing the concentration of Fe, O, or Nb, or by increasing the level of C, Si, or Si + Zr. Vanadium was found not to influence creep behavior under these test conditions.

It was reported in Annual Report No. 2² that Si and Si + Zr are effective for improving creep resistance by pinning mobile dislocations during creep exposure. Close control of Fe to its lowest possible level is also an effective approach to increased creep resistance.



Carbon additions enhance creep resistance as well, although to a lesser extent than Si. Primary creep behavior as a function of alloying addition follows the same general trend as the minimum creep rate.

3.3.4 Phase II Results

3.3.4.1 Material Selection

For Phase II studies, the base alloy composition was changed to Ti-24Al-11Nb (at pct.). Iron, silicon, and carbon were included for study based on results obtained in Phase I. After casting, ingots were sectioned and rolled to 1/2 in. diameter rod. This processing resulted in improved homogenization of the alloys as well as providing a convenient size for machining tensile and creep samples. Chemical analyses of the ingots are given in Table II. Alloy No. 1 is the 'baseline' composition and will be considered the third composition in each group of alloys. Carbon varies by about a factor of two, iron by a factor of five, and silicon by a factor of at least thirty.

Table II
Compositions of Ti Aluminide Alloys, at% (wt%)

Alloy	Ti	Al	Nb	O	C	Fe	Si
1	Bal.	25.4 (14.5)	10.7 (21.0)	0.207 (0.070)	0.165 (0.042)	0.050 (0.059)	0.0 (0.0)
2	Bal.	25.3 (14.4)	10.8 (21.1)	0.16 (0.054)	<u>0.077</u> (0.020)	0.065 (0.077)	0.0 (0.0)
3	Bal.	24.8 (14.1)	10.8 (21.1)	0.187 (0.063)	<u>0.101</u> (0.026)	0.071 (0.084)	0.0 (0.0)
4	Bal.	23.8 (13.5)	10.8 (21.0)	0.244 (0.082)	0.186 (0.047)	<u>0.009</u> (0.011)	0.0 (0.0)
5	Bal.	24.5 (13.9)	10.8 (21.1)	0.249 (0.084)	0.174 (.044)	<u>0.020</u> (0.024)	0.0 (0.0)
6	Bal.	25.1 (14.3)	10.7 (21.0)	0.213 (0.072)	0.158 (0.040)	0.053 (0.062)	<u>0.123</u> (0.073)
7	Bal.	25.4 (14.5)	10.7 (21.0)	0.274 (0.093)	0.169 (0.043)	0.053 (0.063)	<u>0.302</u> (0.180)

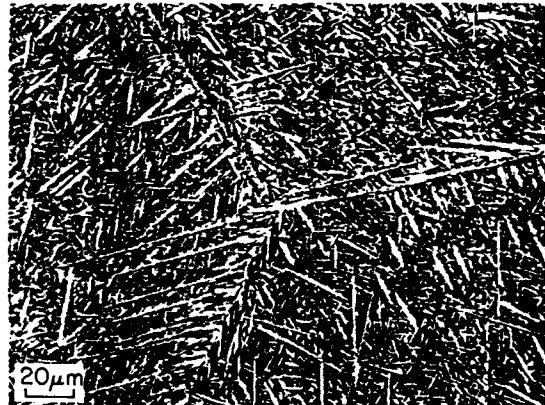


3.3.4.2 Heat Treatments

The microstructures selected for all testing were based on beta annealing, followed by air cooling. Each alloy was heated to a temperature low in the beta phase field, 1200°C, and held for a short time, 0.5 hour, to minimize beta grain growth. Typical microstructures are shown in Fig. 40. It is well-known that a transformed beta microstructure is optimum for creep resistance.⁴⁸

Fig. 40

Typical microstructure of Ti-24Al-11Nb alloys creep tested in this program.



3.3.4.3 Tensile Properties

Prior to creep testing, all alloys were tensile tested at room temperature and at creep temperatures. These were round bar specimens (0.16 in. diameter) tested at a strain rate of 0.005 in./in./min. Room temperature results are presented in Table 12. The two alloys with the lower Fe levels, #4 and #5, tend to exhibit higher strengths and lower ductilities than the other alloys at room temperature and 600°C, Tables 13-15. The Fe effect seems to diminish at the higher temperatures.

The tensile strengths are typical for Ti-24Al-11Nb that has been beta annealed. This microstructure, which is most effective for creep resistance,⁴⁸ results in a decrease in room temperature ductility. Elongation and reduction of area values suggest that the ductile/brittle transition has been exceeded at 600°C.



Table 12
Room Temperature Tensile Properties of Titanium Aluminide Alloys

Alloy No.	0.2% Offset Yield Strength, MPa	Ultimate Tensile Strength, MPa	Pct. Elong.	Pct. RA
1	638	648	1.2	2.8
2	653	814	3.8	7.0
3	812	924	2.0	3.8
4	688	788	0.7	3.8
5	787	848	0.6	7.0
6	630	737	1.8	4.3
7	616	647	1.5	2.7

Table 13
600°C Tensile Properties of Titanium Aluminide Alloys

Alloy No.	0.2% Offset Yield Strength, MPa	Ultimate Tensile Strength, MPa	Pct. Elong.	Pct. RA
1	421	674	15.6	22.5
2	485	734	16.9	24.1
3	540	736	15.3	22.5
4	467	658	4.8	26.3
5	459	619	4.0	17.8
6	453	681	14.6	18.4
7	450	715	20.7	27.2



Table 14
675°C Tensile Properties of Titanium Aluminide Alloys

Alloy No.	0.2% Offset Yield Strength, MPa	Ultimate Tensile Strength, MPa	Pct. Elong.	Pct. RA
1	404	619	15.0	20.1
2	426	635	16.6	27.3
3	437	634	17.2	22.5
4	412	546	11.5	28.9
5	417	572	10.0	19.4
6	395	597	13.8	20.6
7	434	592	11.8	17.3

Table 15
750°C Tensile Properties of Titanium Aluminide Alloys

Alloy No.	0.2% Offset Yield Strength, MPa	Ultimate Tensile Strength, MPa	Pct. Elong.	Pct. RA
1	348	510	17.3	21.9
2	363	522	30.7	59.8
3	372	520	15.2	20.8
4	338	449	11.5	22.4
5	383	486	17.0	37.9
6	337	508	28.9	31.5
7	321	497	15.3	20.8

3.3.4.4 Creep Properties

Creep tests were conducted at 600, 675, and 750°C with three stress levels (constant load tests) at each temperature. The (initial) stress levels for each temperature corresponded to approximately 25, 40 and 60 percent of the yield strength. All creep tests exhibited well defined primary and secondary regimes, except for the highest stress level (207 MPa) at the highest temperature (750°C). Tests were terminated after the establishment of steady-state creep, except for one sample which was run to fracture.



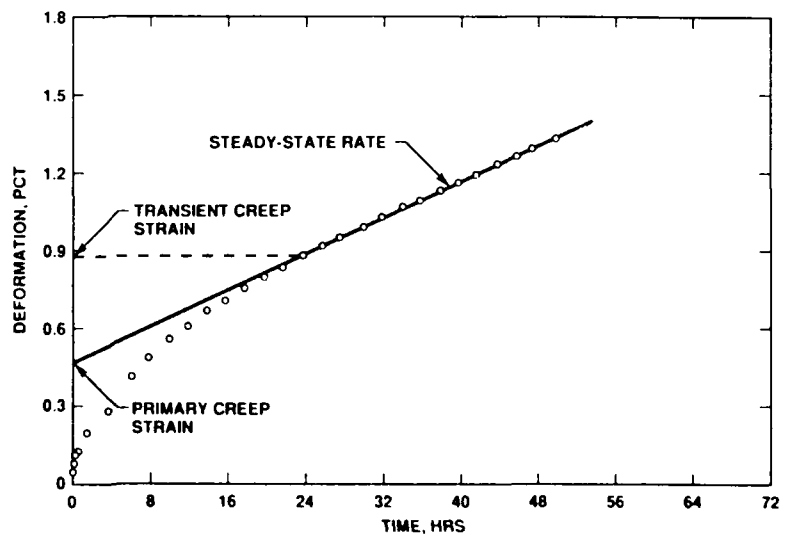
Surface cracking of the type observed in creep samples tested to failure in Phase I was not detected in these Phase II studies, with two exceptions. The only sample tested to fracture - Alloy 25, 750°C/20 ksi - contained numerous circumferential surface cracks. One of these cracks initiated failure. The sample of Alloy 26 tested at 675°C/25 ksi contained a large volume fraction of equiaxed primary alpha-two due to improper heat treatment. As a result, a large creep strain developed and surface cracks were observed. It would appear that surface cracking is a function of strain and time at temperature.

3.3.4.4.1 Primary Creep

Primary creep strain was measured from creep curves in the manner shown in Fig. 41. Primary creep strain is plotted as a function of applied stress for each of the three temperatures in Fig. 42. The slopes of the three temperature regimes are approximately the same, indicating that the relative influence of applied stress on primary creep is independent of temperature. As expected, primary creep strain increases with increasing temperature. There is no strong systematic effect of C, Fe, or Si on primary creep strain or on the time required to reach steady-state creep.

Fig. 41

Illustrating method for determining primary creep strain from experimental creep curve.



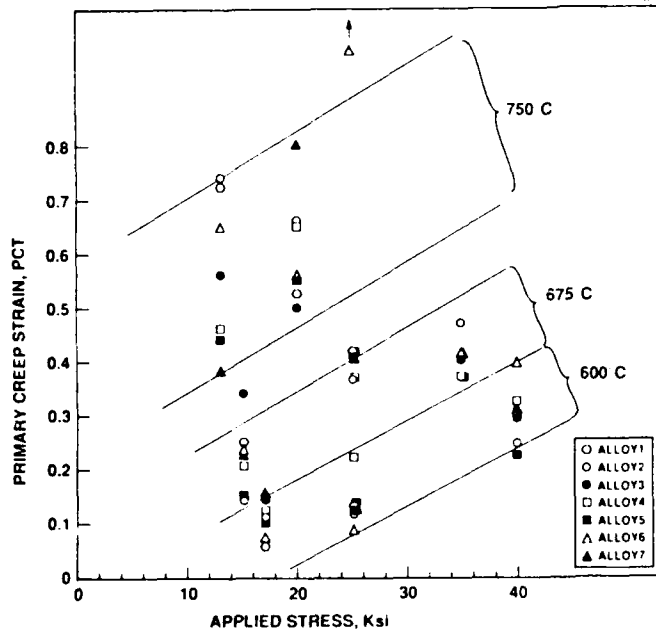


Fig. 42

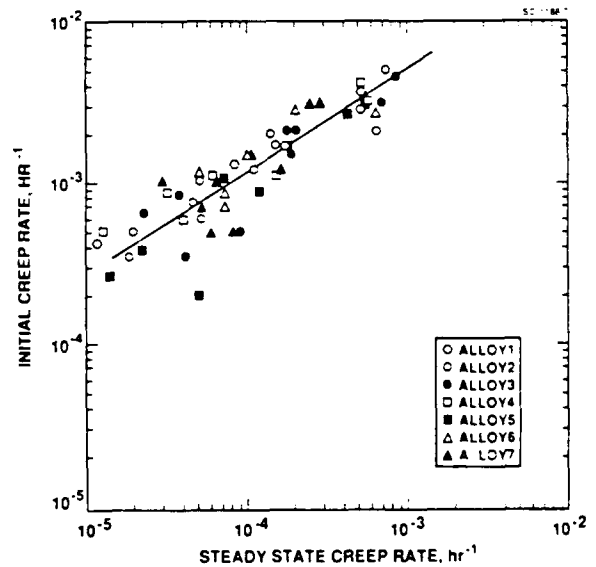
Primary creep strain for Ti-24Al-11Nb alloys as a function of applied stress for three temperatures.

The initial creep rate, i.e., the rate recorded immediately following initial loading and system response (compliance), was measured from creep curves and plotted vs steady-state creep rate, Fig. 43.

There is a positive correspondence of initial creep rate with steady-state rate indicating that primary creep is influenced by those factors that influence steady-state creep.

Fig. 43

Initial creep rate for Ti-24Al-11Nb alloys as a function of steady-state creep rate.



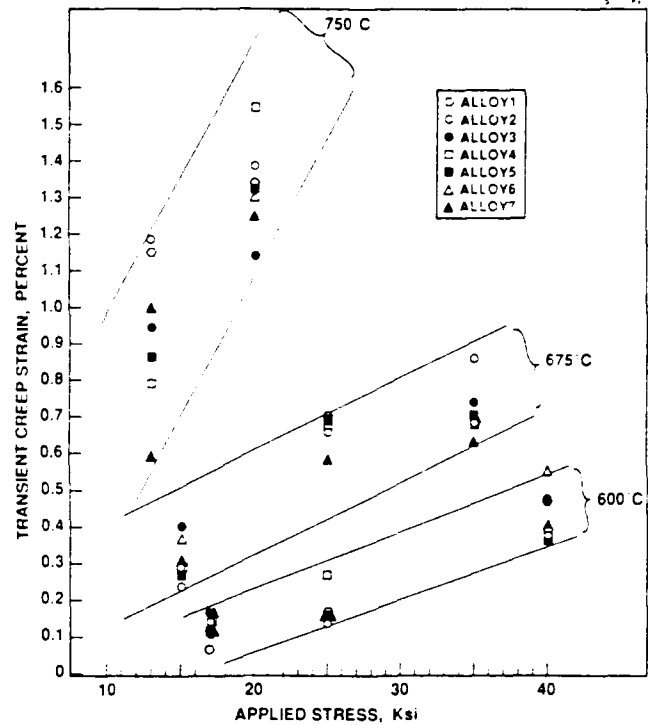
Transient creep strain, which is the total measured strain at the onset of steady-state creep, can be important in structural applications. This is especially true when transient creep strain is a significant fraction of the design allowable creep strain. Transient creep strains are plotted as a function of applied stress in Fig. 44. Unlike primary creep strain (Fig. 42), the slopes of the three temperature regimes are not the same. That is, the rate at which transient creep strain increases with



applied stress increases with temperature. It is clear from Fig. 44 that significant levels of strain can accumulate during the transient creep stage.

Fig. 44

Transient creep strain as a function of applied stress.



3.3.4.4.2 Secondary Creep

Steady-state creep rates for the seven compositions, three temperatures and three stress levels are given in Tables A1 through A9 in the Appendix. The variations in creep rates are small, corresponding to small variations in compositions. Nevertheless, there are definite effects of alloying additions on secondary creep rate. For instance, the effect of carbon is shown in Figs. 45-47. Although the differences are not large, it is apparent from the plots that increasing carbon lowers steady-state creep rate. In general, the effect is most pronounced at the highest stress levels.

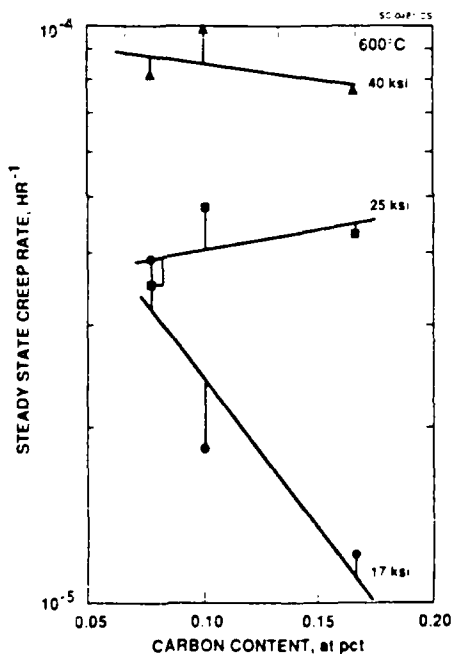


Fig. 45

Steady-state creep rate at 600°C as a function of carbon content for three stress levels.

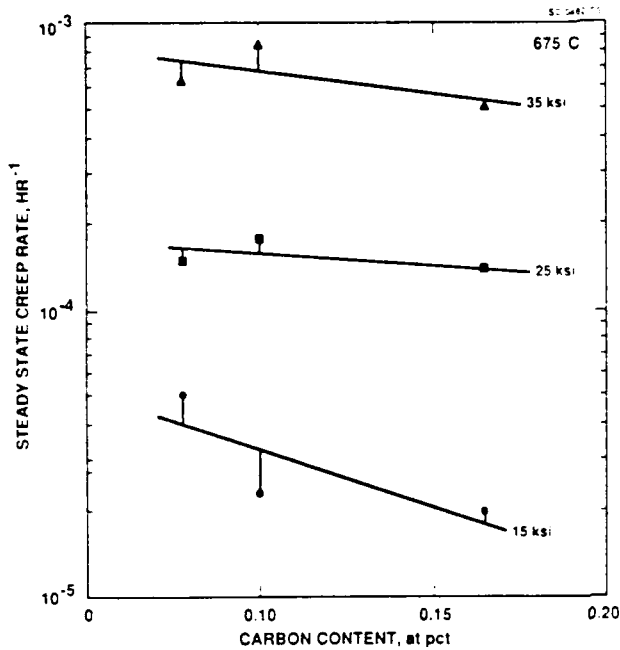


Fig. 46 Steady-state creep rate at 675°C as a function of carbon content for three stress levels.

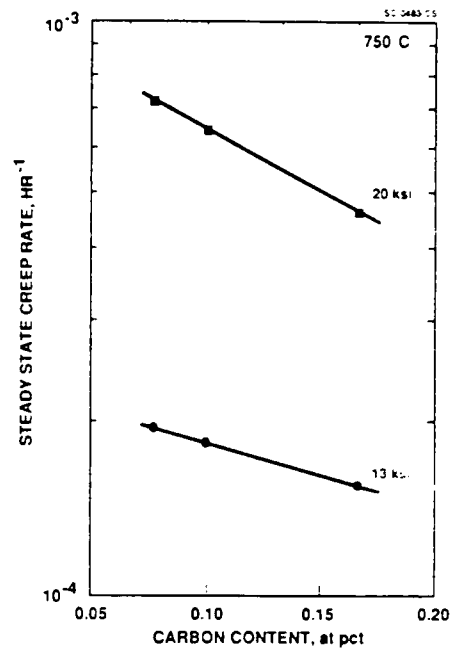


Fig. 47 Steady-state creep rate at 750°C as a function of carbon content for two stress levels.

The effect of Fe on steady-state creep rate is demonstrated in Figs. 48-50. The 600°C data, Fig. 48, show that a decrease in Fe content results in lower creep rates at the higher stress levels. As the temperature increases, the effect of Fe is diminished, and even appears reversed at 750°C.

Silicon tends to lower creep rates, as shown in Figs. 51-53. At 600°C, the silicon-bearing alloys actually have higher creep rates than the baseline (0 Si) alloy. However, as the temperature is increased, the Si-containing alloys are seen to lower the creep rates.

Plots of steady-state creep rate vs $1/T$ for the seven alloys are presented in Figs. 54-60. Although there are data points for only 3 test temperatures, the curves have been drawn to indicate a change in slope at the lower temperatures. Such behavior is consistent with the observations of others,^{49,50} although Mendiratta and Lipsitt⁴⁹ found the change in creep mechanism to occur around 700°C.

Results of calculations of apparent activation energies, ΔH_c , from the curves in Figs. 54-60 are given in Tables 16-17. For the high temperature regime, these values vary from ~ 200 - 300 kJ/m, in good agreement with previously reported results.^{49,50} Because of the limited data through which the curves have been drawn and from which the calculations

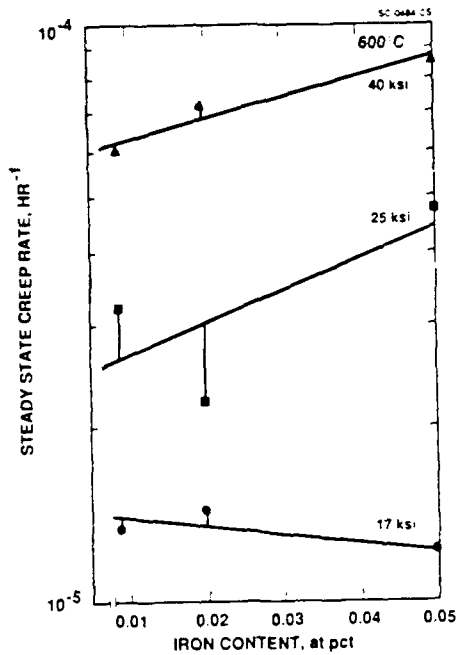


Fig. 48 Steady-state creep rate at 600°C as a function of iron content for three stress levels.

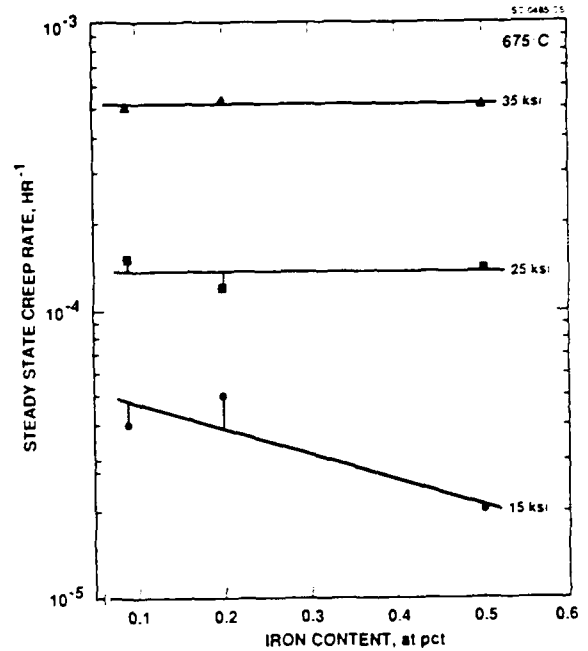


Fig. 49 Steady-state creep rate at 675°C as a function of iron content for three stress levels.

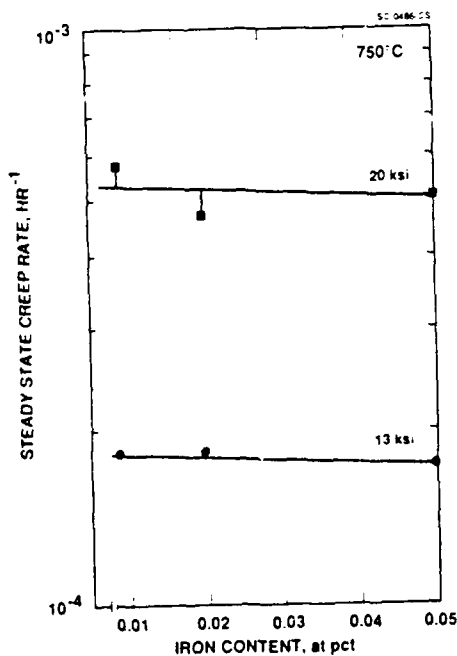


Fig. 50 Steady-state creep rate at 750°C as a function of iron content for two stress levels.

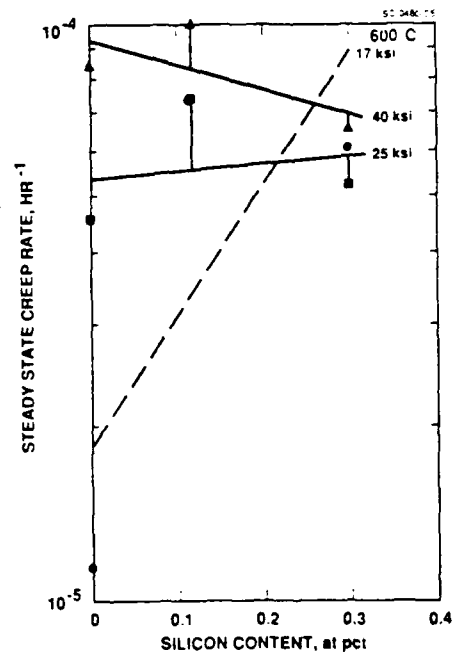


Fig. 51 Steady-state creep rate at 600°C as a function of silicon content for three stress levels.

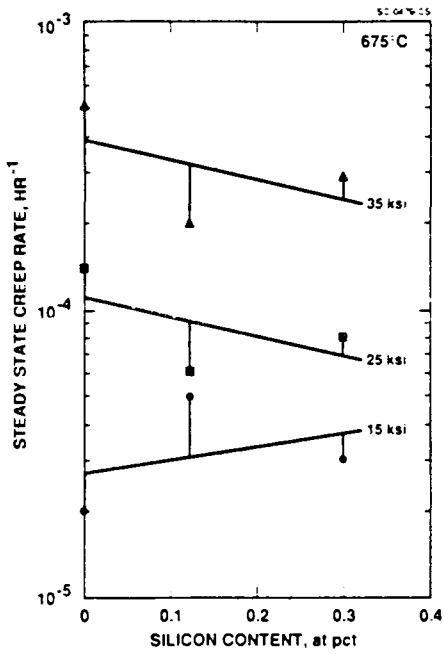


Fig. 52 Steady-state creep rate at 675°C as a function of silicon content for three stress levels.

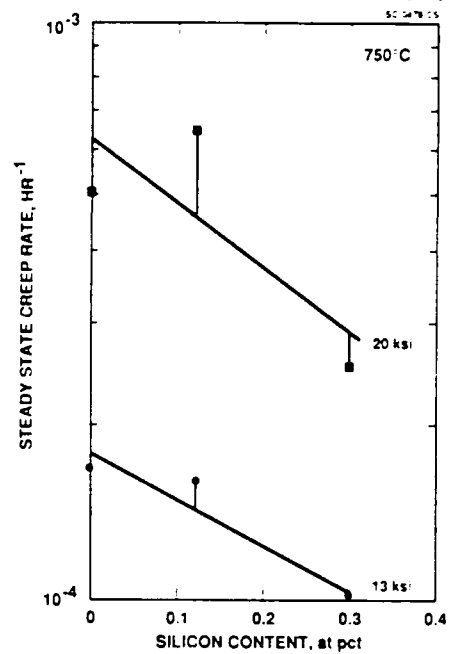


Fig. 53 Steady-state creep rate at 675°C as a function of silicon content for two stress levels.

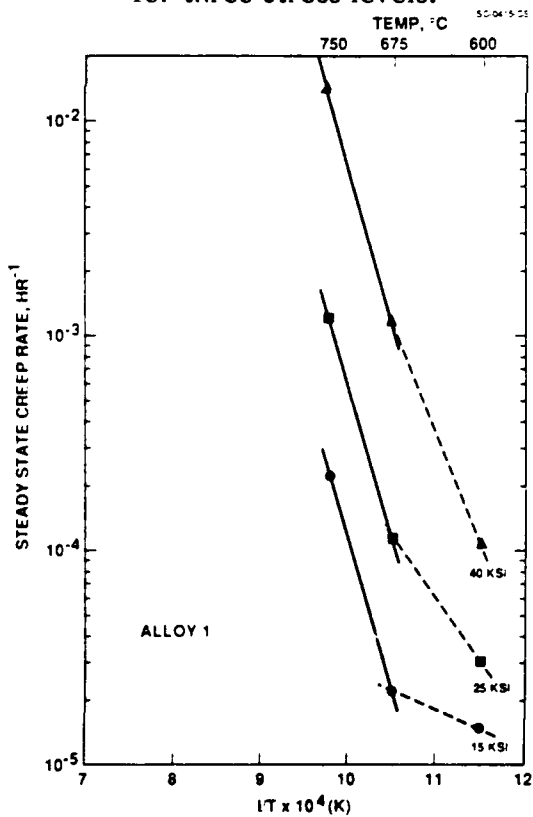


Fig. 54 Steady-state creep rate as a function of reciprocal temperature for baseline alloy at three stress levels.

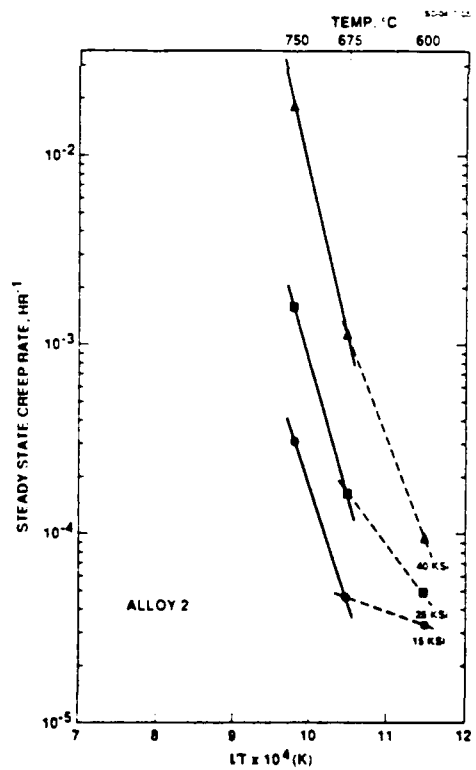


Fig. 55 Steady-state creep rate as a function of reciprocal temperature for low carbon containing alloy at three stress levels.

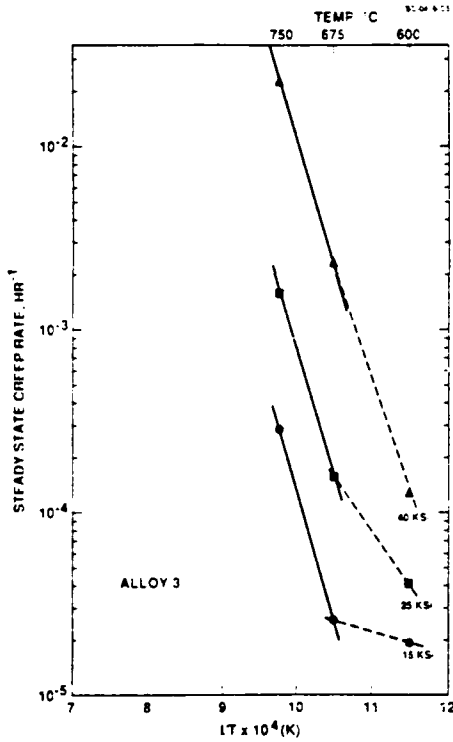


Fig. 56 Steady-state creep rate as a function of reciprocal temperature for intermediate carbon containing alloy at three stress levels.

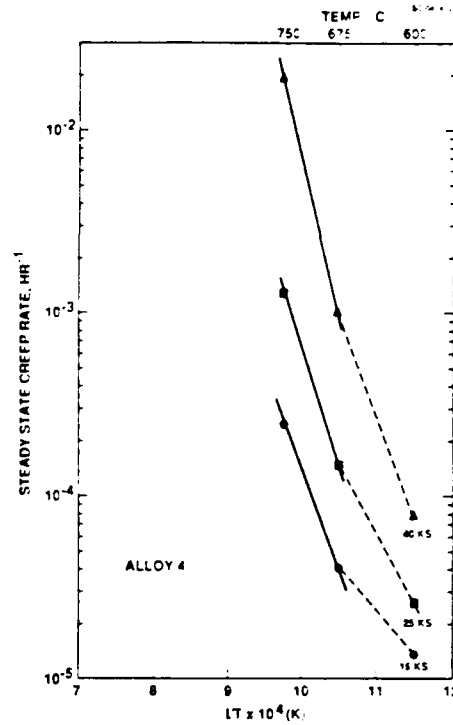


Fig. 57 Steady-state creep rate as a function of reciprocal temperature for low iron containing alloy at three stress levels.

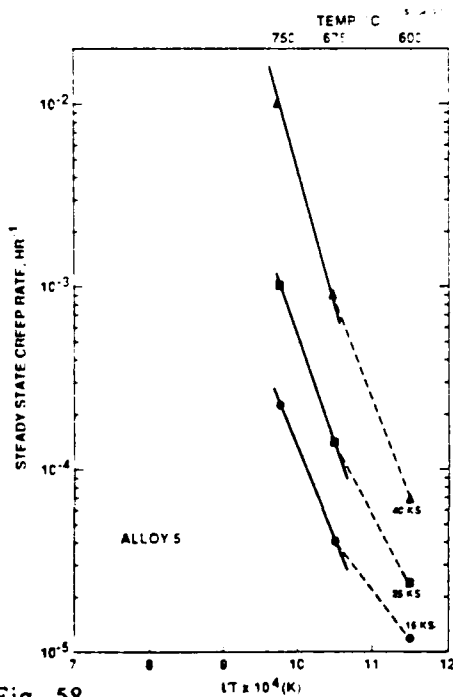


Fig. 58 Steady-state creep rate as a function of reciprocal temperature for intermediate iron containing alloy at three stress levels.

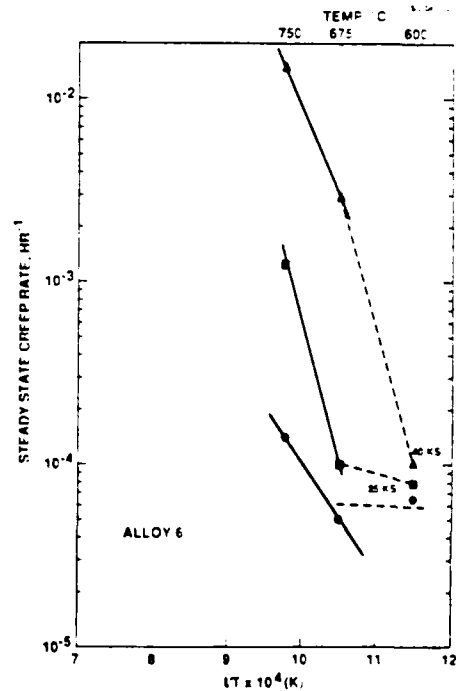


Fig. 59 Steady-state creep rate as a function of reciprocal temperature for intermediate silicon containing alloy at three stress levels.



Fig. 60

Steady-state creep rate as a function of reciprocal temperature for high silicon containing alloy at three stress levels.

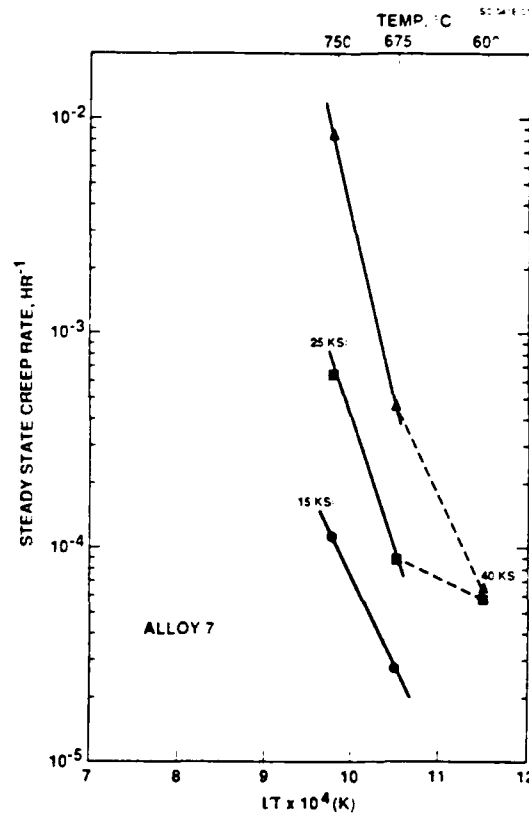


Table 16

Apparent Activation Energy for Steady State Creep in Titanium Aluminide Alloys at 103 MPa (15 ksi)

Alloy No.	Composition Variable	Apparent Activation Energy	
		Low Temperature Regime (kJ/m)	High Temperature Regime (kJ/m)
1	baseline	32	239
2	0.077 C	29	197
3	0.101 C	26	251
4	0.009 Fe	93	186
5	0.020 Fe	100	177
6	0.123 Si	5	107
7	0.302 Si	-	151



Table 17

Apparent Activation Energy for Steady State Creep in Titanium
Aluminide Alloys at 172 MPa (15 ksi)

Alloy No.	Composition Variable	Apparent Activation Energy	
		Low Temperature Regime (kJ/m)	High Temperature Regime (kJ/m)
1	baseline	115	239
2	0.077 C	100	236
3	0.101 C	115	239
4	0.009 Fe	149	224
5	0.020 Fe	156	197
6	0.123 Si	21	267
7	0.302 Si	32	209

Table 18

Apparent Activation Energy for Steady State Creep in Titanium
Aluminide Alloys at 276 MPa (15 ksi)

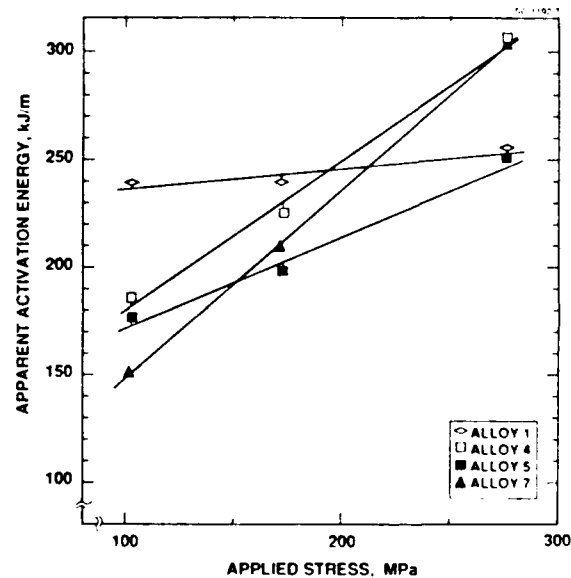
Alloy No.	Composition Variable	Apparent Activation Energy	
		Low Temperature Regime (kJ/m)	High Temperature Regime (kJ/m)
1	baseline	199	255
2	0.077 C	204	285
3	0.101 C	239	239
4	0.009 Fe	214	306
5	0.020 Fe	215	250
6	0.123 Si	280	171
7	0.302 Si	162	302



have been made, detailed analysis of activation energies is not practical. The low temperature, low stress data are especially variable. Nevertheless, trends can be determined. For instance, in the high temperature regime, ΔH_C in the baseline alloy is independent of stress, in agreement with the data of others.^{49,50} On the other hand, there is a slight increase in ΔH_C with applied stress for the Si and Fe containing alloys, Fig. 61. Classically, ΔH_C should decrease with stress,⁵¹ as the increasing stress lowers the material's barrier to creep deformation. Because of the limited data, it is not clear if the stress dependence of ΔH_C is a statistical variation in plotting the data or a physical phenomenon related to the variation with temperature of activation volume and activation stress.⁵¹

Fig. 61

Apparent activation energy vs applied stress for baseline (Alloy 1), low iron (Alloy 4), intermediate iron (Alloy 5), and high silicon (Alloy 7) alloys.



To assist in determining if minor alloying additions have influenced the basic creep mechanism, i.e., altered ΔH_C , the stress exponent in a power law creep equation has been evaluated. Plots of $\ln \dot{\epsilon}$ vs $\ln \sigma$ for all creep tests are presented in Figs. 62-70. Measurements of the slopes of the curves give values for n in the creep equation:

$$\dot{\epsilon}_s = A\sigma^n \quad (27)$$

The results range from around 2.0 at low temperature to around 3.0-4.0 at the higher temperatures, Table 19. The values at the higher temperature are in good agreement with the findings of others.^{49,50} Mendiratta and Lipsitt⁴⁹ also found a stress exponent value of about 2 at temperatures below 650°C.



Fig. 62

$\ln \dot{\epsilon}$ vs $\ln \sigma$ for 600°C test
of variable carbon alloys.

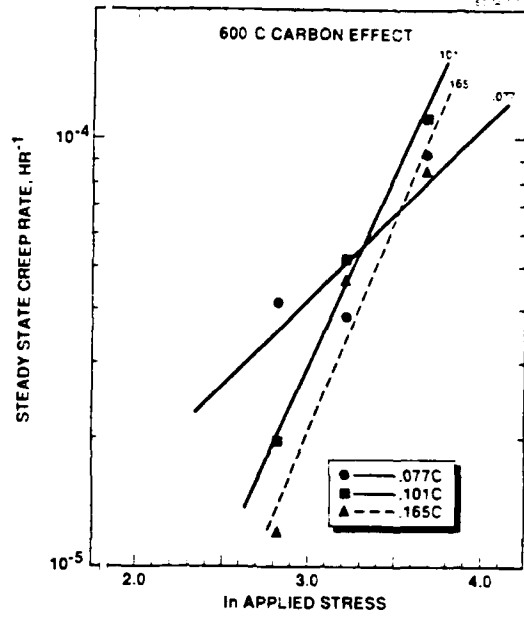


Fig. 63

$\ln \dot{\epsilon}$ vs $\ln \sigma$ for 675°C test of variable
carbon alloys.

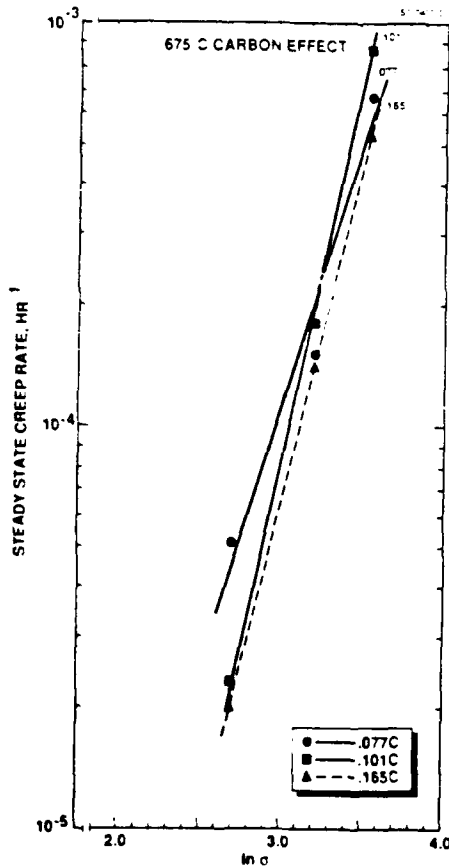


Fig. 64

$\ln \dot{\epsilon}$ vs $\ln \sigma$ for 750°C test of
variable carbon alloys.

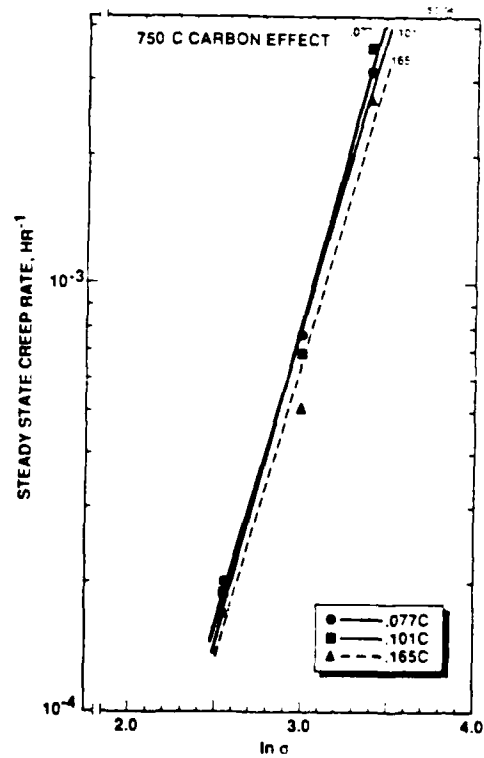




Fig. 65

$\ln \dot{\epsilon}$ vs $\ln \sigma$ for 600°C test of variable iron alloys.

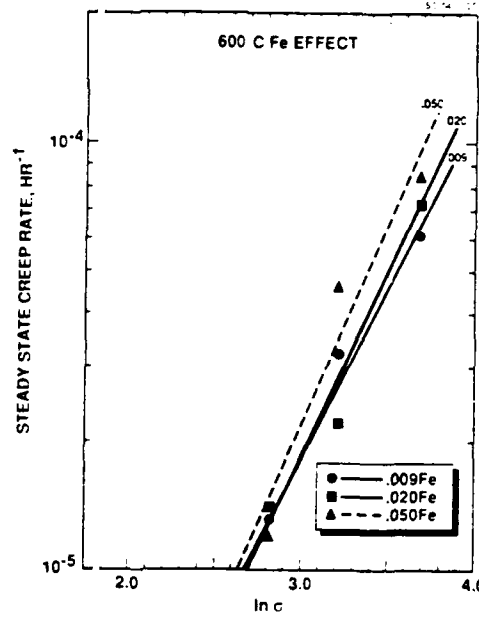


Fig. 66

$\ln \dot{\epsilon}$ vs $\ln \sigma$ for 675°C test of variable iron alloys.

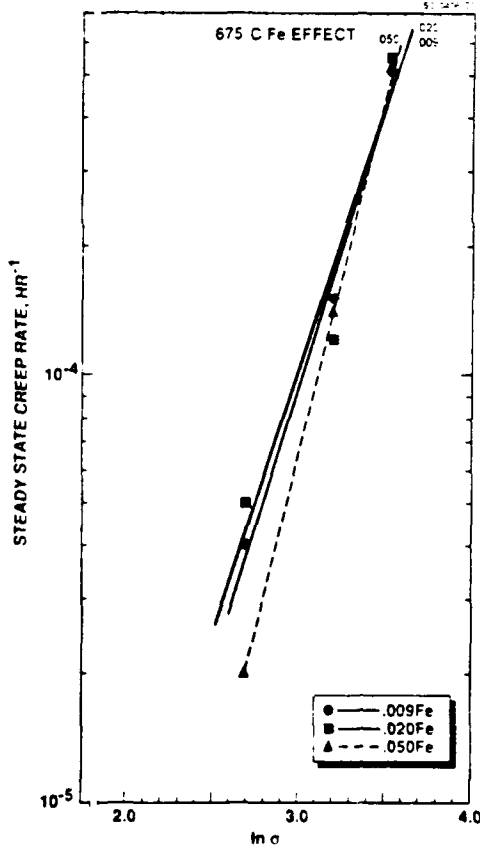


Fig. 67

$\ln \dot{\epsilon}$ vs $\ln \sigma$ for 750°C test of variable iron alloys.

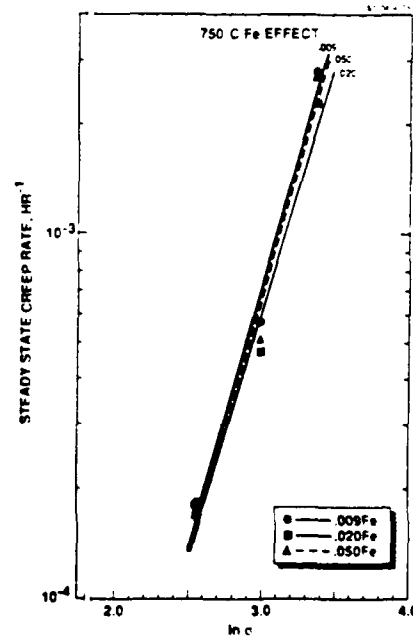




Fig. 68

$\ln \dot{\epsilon}$ vs $\ln \sigma$ for 600°C test of variable silicon alloys.

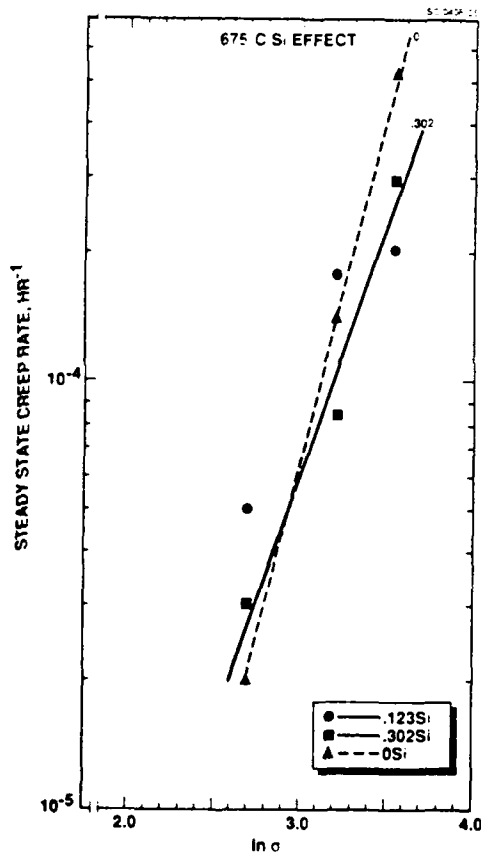
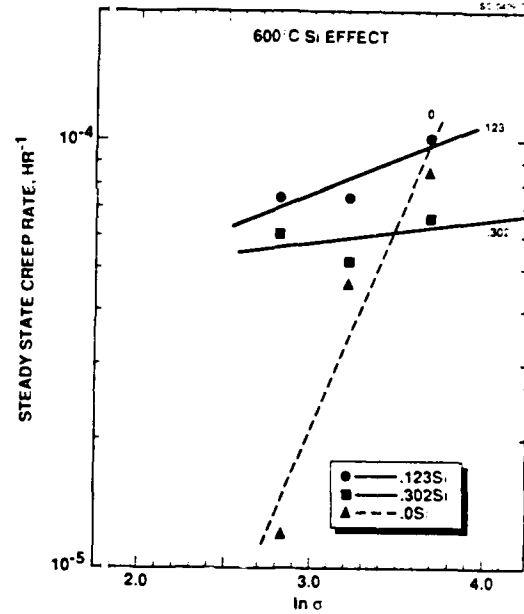


Fig. 69

$\ln \dot{\epsilon}$ vs $\ln \sigma$ for 675°C test of variable silicon alloys.

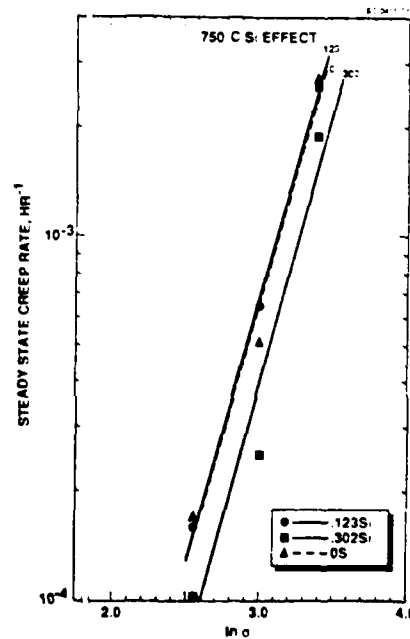


Fig. 70

$\ln \dot{\epsilon}$ vs $\ln \sigma$ for 750°C test of variable silicon alloys.



Table 19
Stress Exponent for Power Law Creep in Titanium Aluminides

Temperature	Composition Variable	Stress Exponent, n
600°C	baseline	2.2
	0.077 C	1.2
	0.101 C	1.9
	0.009 Fe	2.2
	0.020 Fe	2.2
	0.123 Si	0.4
	0.302 Si	0.2
675°C	baseline	4.3
	0.077 C	3.2
	0.101 C	4.1
	0.009 Fe	3.2
	0.020 Fe	3.1
	0.123 Si	1.6
	0.302 Si	2.6
750°C	baseline	3.5
	0.077 C	3.2
	0.101 C	3.4
	0.009 Fe	3.5
	0.020 Fe	3.3
	0.123 Si	3.5
	0.302 Si	4.1

The stress exponent values and the ΔH_c calculations indicate a single creep mechanism over the temperature range 675-750°C, and a second mechanism below 675°C. The data further suggest that there is no significant change in mechanism associated with the variation in minor alloying additions.

3.3.5 Discussion of Results

All the data developed in this program indicate a single creep mechanism in the temperature regime of 675°C-750°C. The stress exponent values of ~ 3-4, in conjunction with ΔH_c values of 200-300 kJ/m, suggest dislocation climb as the most likely rate controlling mechanism. Below 675°C, stress exponent values fall to 1-2, with ΔH_c ~ 100 kJ/m, clearly indicating a change in the rate controlling mechanism. Mendiratta and Lipsitt⁴⁴ also observed a lower activation energy creep mechanism at the lower temperatures. At this point, there is no correspondence of the lower activation energy to a creep mechanism.



Indeed, Wilshire⁵² has recently suggested that the traditional interpretation of $n \sim 1$ being representative of diffusional creep is not necessarily correct. He has demonstrated that the Theta Projection Concept⁵³ predicts creep behavior as a single dislocation mechanism across regimes that produce varying values of stress exponent, n .

Effects of the minor alloying additions on creep behavior are not large, essentially because the changes in compositions are also not large. Primary creep was least affected by composition. However, the amount of strain experienced prior to the onset of steady-state creep can be significant. For instance, transient creep strains can exceed 0.5 pct at 600°C/276 MPa, approach 1 pct at 675°C/241 MPa, and exceed 1 pct at 750°C/90 MPa. The combination of these strains and the time spent in transient creep - up to 30 hours - results in transient creep being a significant portion of total allowable creep in many applications. There was no correlation of composition with transient creep behavior.

Steady-state creep correlated somewhat with composition. The most significant effect was due to silicon at the higher temperatures, where increasing Si reduced the creep rate at all stress levels. It required a Si concentration of 0.302 at. pct. (0.18 wt. pct.) to impact the creep behavior. At a level of 0.123 at. pct. (0.07 wt.pct.), there was no particular improvement in creep resistance over the baseline alloy, which had no measurable Si. In the Second Annual Report,² transmission electron microscopy results demonstrated that Si improved creep resistance in alpha-two type alloys by pinning dislocations. The Si, which is in solution prior to creep exposure, precipitates on mobile dislocations during creep and thereby pins the dislocations. It is likely that the same mechanism is operable in these Phase 2 alloys.

For the composition range studied, the effects of carbon on steady-state creep rates are small, but definite. That is, increasing carbon levels reduces secondary creep rate. Extrapolation of the experimental curves given in Figs. 45-47 indicates that creep rate could be reduced an order of magnitude by increasing the carbon level to about 0.55 at% (0.15 wt%). This carbon concentration is below the solubility limit (for unalloyed Ti), indicating that solid solution strengthening is the mechanism for improved creep resistance.

Iron effects on steady-state creep are most significant at the lowest test temperature (600°C). In this case, lowering Fe concentration results in reduced creep rates. An iron level of 0.009 at% (0.01 wt%) is about as low as is currently reasonable for mill product. Modest improvements in creep resistance in the lower temperature regime could be expected, however, at higher temperatures (675 and 750°C), the iron effect is lost. It



was suggested earlier² that increasing the Fe level may lower the stress required to activate c + a type dislocations. Such a mechanism would be consistent with the observed loss of the Fe effect at higher temperatures, if thermal activation of c + a slip is sufficient to overcome the increased stress accompanying the low iron concentration.

3.3.6 Summary and Conclusions

Creep tests were conducted at 600, 675 and 750°C in air. All tests exhibited well defined primary and secondary regimes. Surface cracking of the type observed in creep samples tested to failure in Phase I, and reported by others,^{50,54,55} was not detected in samples tested only into steady-state regime. Surface cracking is a function of strain and time at temperature. Surface cracking is not a 'creep mechanism' as has been suggested,⁵⁴ but rather occurs when the material has strained well into steady-state or, more likely, into tertiary creep.

Primary creep strain increases with increasing temperature. There is no systematic effect of C, Fe, or Si on primary creep strain. There is a positive correspondence of initial creep rate with steady-state creep rate indicating that primary creep is influenced by those factors that influence steady-state creep. Significant levels of strain can accumulate during transient creep.

There are definite effects of alloying additions on secondary creep rate. The most significant effect was due to silicon at the higher temperatures, where increasing Si reduced the creep rate at all stress levels. The effect of carbon was found to be small, but definite: increasing C reduces secondary creep rates. Iron was effective only at the lowest temperature, where reducing Fe to 0.009 at% (0.01 wt%) decreased creep rates. At the higher temperatures, Fe had essentially no effect on creep.

All the data indicate a single creep mechanism in the temperature regime of 675-750°C. The stress exponent values of 3-4, in conjunction with ΔH_C values of 200-300 kJ/m, suggest dislocation climb as the most likely rate controlling mechanism. Below 675°C, stress exponent values fall to 1-2, with $\Delta H_C \sim 100$ kJ/m, indicating a change in the (unidentified) rate controlling mechanism.



4.0 REFERENCES

1. A.K. Ghosh and C.G. Rhodes, "Processability and High-Temperature Behavior of Emerging Aerospace Alloys," Annual Report No. 1, Contract No. F49620-86-C-0058, SC5459.AR, August 1987.
2. A.K. Ghosh and C.G. Rhodes, "Processability and High Temperature Behavior of Emerging Aerospace Alloys," Annual Report No. 2, Contract No. F49620-86-C-0058, SC5459.AR, August 1988.
3. M.E. Fine and E.A. Starke, "Rapidly Solidified Powder Aluminum Alloys," ASTM STP 890 (1986).
4. V. Anand, A.J. Kaufman and N.J. Grant, "Rapid Solidification of a Modified 7075 Aluminum Alloy by Ultrasonic Gas Atomization," Rapid Solidification Processing - Principles and Technologies II, Ed., R. Mehrabian, B.H. Kear and M. Cohen, Claitors Pub. Div., Baton Rouge, LA (1980), pp. 273-286.
5. C.M. Adam, R.G. Bourdeau and J.W. Broch, AFWAL Report, AFWAL-TR-81-4188, Feb. 1982, Contract No. F33615-76-C-5136.
6. R.E. Lewis, "Advanced Aluminum Alloy from Rapidly Solidified Powders," DARPA Order No. 3147, Report on AFWAL Contract No. F33615-78-C-5203.
7. Y.V.R.K. Prasad, H.L. Gegel, S.M. Doraivelu, J.C. Malus, J.T. Morgan, K.A. Lark and D.R. Barker, *Met. Trans. A* 15, 1883 (1984).
8. J.S. Gunasekara, H.L. Gegal, J.C. Malas, S.M. Doraivelu and J.T. Morgan, Computer-Aided Process Modeling of Hot Forging and Extrusion of Aluminum Alloys (1984).
9. H.L. Gegel, J.S. Gunasekara, S.M. Doraivelu, J.C. Malas, J.T. Morgan and L.E. Matson, Consolidation and Forming of P/M Porous Billets (1985).
10. O. Richmond and M.L. Devenpeck, Proc. 4th U.S. Nat. Cong. of Applied Mechanics, 1503 (1962).
11. W.A. Backofen, Deformation Processing, Addison-Wesley Pub. Co. (1972).
12. J.P. Hirth and J. Lothe, Theory of Dislocations, McGraw Hill (1968).
13. C. Gandhi, C. Bampton, A. Ghosh and C. Anton, Proc. of 5th International Conf. on Aluminum-Lithium Alloys, Eds. T. Sanders and E. Starke, Vol. 1, p. 141 (1989).
14. A.K. Ghosh and R.A. Ayres, *Metall. Tran. A* 7A, 1589 (1976).
15. C. Herring, *J. Appl. Phys.* 21, 437 (1950).
16. R.L. Coble, *J. Appl. Phys.* 34, 1679 (1963).
17. W.A. Backofen, J.R. Turner and D.H. Avery, *Trans. Quart. ASM* 57, 980 (1964).



18. M.F. Ashby and R.A. Verrall, *Acta Metall.* 21, 149 (1973).
19. R. Raj and A.K. Ghosh, *Acta Metall.* 29, 283 (1981).
20. C.C. Bampton and R. Raj, *Acta Metall.* 30, 2043 (1982).
21. C.C. Bampton, M.W. Mahoney, C.H. Hamilton, A.K. Ghosh and R. Raj, *Metall. Trans. A* 14A, 1583 (1983).
22. J.A. Wert, N.E. Paton, G.H. Hamilton and M.W. Mahoney, *Metall. Trans. A* 12A, 1265 (1981).
23. C.H. Hamilton, C.C. Bampton and N.E. Paton, Superplastic Forming of Structural Alloys, Eds. N.E. Paton and C.H. Hamilton, The Metallurgical Society of AIME, Warrendale, PA, 1982, p. 173.
24. M.H. Mahoney and A.K. Ghosh, *Metall. Tran. A* 18A, 653 (1987).
25. A. Ghosh and C. Gandhi, *Proc. of 7th International Conf. on Strength of Metals and Alloys*, Eds. H. McQueen et al, Pergamon Press, p. 2065 (1986).
26. C. Gandhi and A.K. Ghosh, "Grain Refinement and Superplastic Forming of an Aluminum Base Alloy," U.S. Patent No. 4770848, Sept. 1988.
27. C. Gandhi and A.K. Ghosh, in Light-Weight Alloys for Aerospace Applications, Eds. E.W. Lee, E.H. Chia and N.J. Kim, The Minerals, Metals and Materials Society, Warrendale, PA, 1989, p. 385.
28. H.J. Frost and M.F. Ashby, Deformation-Mechanism Maps, Pergamon Press, NY, 1982, p. 21.
29. T.S. Lundy and J.F. Murdock, *J. Appl. Phys.* 33, 1671 (1962).
30. A. Ghosh, C. Gandhi, R. Crooks and J. Wert, *Ultrafine Grain Aluminum Research and Data*, Final Report: WRDC-TR-89-4021, p. 19-77 (1989).
31. W.T. Read and W. Shockley, *Phys. Rev.* 78, 275 (1950).
32. G. Glover and C.M. Sellars, *Metall. Trans.* 4A, 765 (1973).
33. T. Sakai and J.J. Jonas, *Acta Met.* 32, 189 (1984).
34. A.S. Argon, *Scripta Metall.* 4, 1001 (1970).
35. R. Raj and M.F. Ashby, *Metall. Trans. A.* 2A, 1113 (1971).
36. B. Baudelet and M. Surey, *Proc. of International Conf. on Superplasticity*, Eds. B. Baudelet and M. Surey, Grenoble, France, p. 17 (1985).
37. N.E. Paton and C.H. Hamilton, Method for Imparting Fine Grain Size to Aluminum Alloys Containing Precipitates Constituents, U.S. Patent No. 4,292,181 (1978).



38. A.K. Ghosh, Method for Producing a Fine Grain Aluminum Alloy Using Three Axes Deformation, U.S. Patent No. 4,721,537, June 1988.
39. D.L. Yaney and W.D. Nix, Metall. Trans. A 18, 893-902 (1987).
40. R. Ayer, L.M. Angers, et al, Metall. Trans. A 19, 1645-1656 (1988).
41. D. Legzdina and T.A. Parthasarthy, Metall. Trans. A 18, 1713-1719 (1987).
42. P.J. Bania and J.A. Hall, "Titanium Science and Technology," Proc. 5th Int. Conf. on Titanium, G. Lutjering, U. Zwicker and W. Bunk, eds., Deutsche Gesellschaft fur Metallkunde E.V., Oberursel, 1985, pp. 2371-2378.
43. P.K. Raut and W.R. Clough, "Titanium Science and Technology," Proc. 2nd Int. Conf. on Titanium, R.I. Jaffee and H.M. Burte, eds., Plenum Press, NY, 1973, pp. 2243-2254.
44. C.G. Rhodes, Rockwell International Science Center, Thousand Oaks, CA, unpublished research.
45. M.W. Mahoney and N.E. Paton, "The Effect of Minor Alloying Element Additions on Mechanical Properties of Titanium Alloys," Technical Report AFML-TR-77-56, May 1977.
46. G.S. Hall, S.R. Seagle and H.B. Bomberger, "Titanium Science and Technology," Proc. 2nd Int. Conf. on Titanium, R.I. Jaffee and H.M. Burte, eds., Plenum Press, NY, 1973, pp. 2141-2150.
47. M. Kehoe and R.W. Broomfield, *ibid.*, pp. 2167-2178.
48. E. Bohanek and H. D. Kessler, Reactive Metals, W.R. Clough, ed., Interscience Publishers, N.Y., 1959, pp. 23-41.
49. M.G. Mendiratta and H.A. Lipsitt, J. Mater. Sci. 15, pp. 2985-2990 (1980).
50. R.W. Hayes, Scr. Met. 23, pp. 1931-1936 (1989)
51. F. Garafalo, "Fundamentals of Creep and Creep-Rupture in Metals," MacMillan Co., N.Y., pp. 91-92 (1966).
52. B. Wilshire, in Creep and Fracture of Engineering Materials and Structures, B. Wilshire and R.W. Evans, eds., The Institute of Metals, London, 1990, pp. 1-9.
53. R.W. Evans, J.D. Parker and B. Wilshire, in Recent Advances in Creep and Fracture of Engineering Materials and Structures, B. Wilshire and D.R.J. Owen, eds., Pineridge Press, Swansea, 1982, p. 135.
54. J.A. Hall, Garrett Turbine Engine Div., Allied-Signal, Phoenix, AZ, private communication.
55. B.J. Marquardt, General Electric Co., Evendale, OH, private communication.



5.0 APPENDIX

Table A1
Steady State Creep Rates for Titanium Aluminides Tested
at 600°C and 117 MPa (17 ksi)

Alloy No.	Steady State Creep Rate (hr ⁻¹)	Time to Reach Steady State (hr)	Composition Variant (at. pct.)
1	1.2×10^{-5}	10.6	baseline
2	4.2×10^{-5}	6.7	0.077 C
3	1.9×10^{-5}	10.5	0.101 C
4	1.3×10^{-5}	8.3	0.009 Fe
5	1.4×10^{-5}	12.4	0.020 Fe
6	7.3×10^{-5}	4.5	0.123 Si
7	6.0×10^{-5}	6.6	0.302 Si

Table A2
Steady State Creep Rates for Titanium Aluminides Tested
at 600°C and 172 MPa (17 ksi)

Alloy No.	Steady State Creep Rate (hr ⁻¹)	Time to Reach Steady State (hr)	Composition Variant (at. pct.)
1	4.6×10^{-5}	8.7	baseline
2	3.8×10^{-5}	6.7	0.077 C
3	5.2×10^{-5}	8.7	0.101 C
4	3.2×10^{-5}	14.8	0.009 Fe
5	2.2×10^{-5}	15.0	0.020 Fe
6	7.3×10^{-5}	8.6	0.123 Si
7	5.2×10^{-5}	6.7	0.302 Si



Table A3

Steady State Creep Rates for Titanium Aluminides Tested
at 600°C and 276 MPa (17 ksi)

Alloy No.	Steady State Creep Rate (hr ⁻¹)	Time to Reach Steady State (hr)	Composition Variant (at. pct.)
1	8.4×10^{-5}	20.9	baseline
2	9.1×10^{-5}	16.5	0.077 C
3	11.1×10^{-5}	18.8	0.101 C
4	6.1×10^{-5}	13.6	0.009 Fe
5	7.2×10^{-5}	18.8	0.020 Fe
6	10.0×10^{-5}	15.7	0.123 Si
7	6.5×10^{-5}	15.0	0.302 Si

Table A4

Steady State Creep Rates for Titanium Aluminides Tested
at 675°C and 103 MPa (17ksi)

Alloy No.	Steady State Creep Rate (hr ⁻¹)	Time to Reach Steady State (hr)	Composition Variant (at. pct.)
1	2.0×10^{-5}	24.9	baseline
2	5.1×10^{-5}	16.8	0.077 C
3	2.3×10^{-5}	32.8	0.101 C
4	4.0×10^{-5}	25.2	0.009 Fe
5	5.0×10^{-5}	23.4	0.020 Fe
6	5.0×10^{-5}	25.7	0.123 Si
7	3.0×10^{-5}	29.3	0.302 Si



Table A5
Steady State Creep Rates for Titanium Aluminides Tested
at 675°C and 117 MPa (17 ksi)

Alloy No.	Steady State Creep Rate (hr ⁻¹)	Time to Reach Steady State (hr)	Composition Variant (at. pct.)
1	1.4 x 10 ⁻⁴	19.2	baseline
2	1.5 x 10 ⁻⁴	20.8	0.077 C
3	1.8 x 10 ⁻⁴	15.4	0.101 C
4	1.5 x 10 ⁻⁴	21.1	0.009 Fe
5	1.2 x 10 ⁻⁴	25.0	0.020 Fe
6	0.6 x 10 ⁻⁴	--	0.123 Si
7	0.8 x 10 ⁻⁴	23.0	0.302 Si

Table A6
Steady State Creep Rates for Titanium Aluminides Tested
at 675°C and 241 MPa (17 ksi)

Alloy No.	Steady State Creep Rate (hr ⁻¹)	Time to Reach Steady State (hr)	Composition Variant (at. pct.)
1	5.2 x 10 ⁻⁴	5.4	baseline
2	6.5 x 10 ⁻⁴	6.0	0.077 C
3	8.5 x 10 ⁻⁴	3.9	0.101 C
4	5.1 x 10 ⁻⁴	6.0	0.009 Fe
5	5.4 x 10 ⁻⁴	6.2	0.020 Fe
6	2.0 x 10 ⁻⁴	13.4	0.123 Si
7	2.9 x 10 ⁻⁴	7.8	0.302 Si



Table A7

Steady State Creep Rates for Titanium Aluminides Tested
at 750°C and 90 MPa (17ksi)

Alloy No.	Steady State Creep Rate (hr ⁻¹)	Time to Reach Steady State (hr)	Composition Variant (at. pct.)
1	1.7×10^{-4}	25.9	baseline
2	2.0×10^{-4}	23.1	0.077 C
3	1.9×10^{-4}	21.7	0.101 C
4	1.8×10^{-4}	19.9	0.009 Fe
5	1.8×10^{-4}	23.8	0.020 Fe
6	1.6×10^{-4}	21.9	0.123 Si
7	1.0×10^{-4}	22.1	0.302 Si

Table A8

Steady State Creep Rates for Titanium Aluminides Tested
at 750°C and 138 MPa (17 ksi)

Alloy No.	Steady State Creep Rate (hr ⁻¹)	Time to Reach Steady State (hr)	Composition Variant (at. pct.)
1	5.1×10^{-4}	15.8	baseline
2	7.6×10^{-4}	10.1	0.077 C
3	6.8×10^{-4}	9.8	0.101 C
4	5.7×10^{-4}	15.8	0.009 Fe
5	4.7×10^{-4}	13.6	0.020 Fe
6	6.4×10^{-4}	11.5	0.123 Si
7	2.5×10^{-4}	27.6	0.203 Si



Table A9
Steady State Creep Rates for Titanium Aluminides Tested
at 750°C and 207 MPa (17ksi)

Alloy No.	Steady State Creep Rate (hr ⁻¹)	Time to Reach Steady State (hr)	Composition Variant (at. pct.)
1	2.7×10^{-3}	---	baseline
2	3.2×10^{-3}	---	0.077 C
3	3.6×10^{-3}	---	0.101 C
4	2.8×10^{-3}	---	0.009 Fe
5	2.3×10^{-3}	---	0.020 Fe
6	2.6×10^{-3}	---	0.123 Si
7	1.9×10^{-3}	---	0.302 Si